SCANNING TUNNELING SPECTROSCOPIC STUDIES ON HIGH-TEMPERATURE SUPERCONDUCTORS AND DIRAC MATERIALS

Thesis by

Marcus Lawrence Teague

In Partial Fulfillment of the Requirements for the

degree of

Doctor of Philosophy

CALIFORNIA INSTITUTE OF TECHNOLOGY

Pasadena, California

2013

(Defended June 8, 2012)

ACKNOWLEDGEMENTS

I would like to thank Andrew for his help in getting started with STM, his friendship, and many great conversations. I also thank Cameron for the many fun times and general agreement on the pitfalls of life. Chen Tzu and Ted, thank you for making me feel welcome in the group when I first started and for the very wise advice you gave. Thanks to Slobodan for friendship and the massively fun debates that we had. A big thanks to all the great undergrads I have had the privilege of working with: Renee Wu, Andrew Lai, Garret Dryna, and Michael Grinolds. Yall were all a massive help. Thank you Hao for your help in the last year.

A major thank you to Loly, without whom I could not have survived these last eight years, for navigating me through the bureaucracy of Caltech. I would also like to thanks Nil Asplund for his *massive* help on so many projects. I could not have gotten as far as I did without your help. And thank you Nai-Chang, for your patience when I did not deserve it, your aid when I needed it, and for teaching me the important aspects of being a research scientist.

Thanks to my parents and family for your support and love and for being there when I needed you. Thank you Cindy, Karen, Sherry, Becky, Aarin, Leslie, Eric, Lety, Mike, Dad, and Mom.

Thank you to my best friends Jayson, Mike, and Justin. Yall have kept me sane all these years and have given useful, if not very blunt, advice which yall routinely provided free of charge with extra sass on top. Thank you Katie for your friendship and the many lunchtime drives to Pasadena. Most importantly I must thank the good Lord for his aid in all things, his grace, and his forgiveness. Finally, thank you, Boodle.

ABSTRACT

This thesis details the investigations of the unconventional low-energy quasiparticle excitations in electron-type cuprate superconductors and electron-type ferrous superconductors as well as the electronic properties of Dirac fermions in graphene and three-dimensional strong topological insulators through experimental studies using spatially resolved scanning tunneling spectroscopy (STS) experiments.

Magnetic-field- and temperature-dependent evolution of the spatially resolved quasiparticle spectra in the electron-type cuprate $La_{0.1}Sr_{0.9}CuO_2$ (La-112) T_C = 43 K, are investigated experimentally. For temperature (T) less than the superconducting transition temperature (T_C), and in zero field, the quasiparticle spectra of La-112 exhibits gapped behavior with two coherence peaks and no satellite features. For magnetic field measurements at $T < T_C$, first ever observation of vortices in La-112 are reported. Moreover, pseudogap-like spectra are revealed inside the core of vortices, where superconductivity is suppressed. The intra-vortex pseudogap-like spectra are characterized by an energy gap of $V_{PG} = 8.5 \pm 0.6$ meV, while the inter-vortex quasiparticle spectra shows larger peak-to-peak gap values characterized by $\Delta_{pk\text{-}pk}(H) > V_{PG}$, and $\Delta_{pk\text{-}pk}(0) = 12.2 \pm 0.8$ meV $> \Delta_{pk\text{-}pk}(H > 0)$. The quasiparticle spectra are found to be gapped at all locations up to the highest magnetic field examined (H = 6T) and reveal an apparent low-energy cutoff at the V_{PG} energy scale.

Magnetic-field- and temperature-dependent evolution of the spatially resolved quasiparticle spectra in the electron-type “122” iron-based $Ba(Fe_{1-x}Co_x)_2As_2$ are investigated for

multiple doping levels (x = 0.06, 0.08, 0.12 with T_C= 14 K, 24 K, and 20 K). For all doping levels and the T < T_C, two-gap superconductivity is observed. Both superconducting gaps decrease monotonically in size with increasing temperature and disappear for temperatures above the superconducting transition temperature, T_C. Magnetic resonant modes that follow the temperature dependence of the superconducting gaps have been identified in the tunneling quasiparticle spectra. Together with quasiparticle interference (QPI) analysis and magnetic field studies, this provides strong evidence for two-gap sign-changing s-wave superconductivity.

Additionally spatial scanning tunneling spectroscopic studies are performed on mechanically exfoliated graphene and chemical vapor deposition grown graphene. In all cases lattice strain exerts a strong influence on the electronic properties of the sample. In particular topological defects give rise to pseudomagnetic fields (B ~ 50 Tesla) and charging effects resulting in quantized conductance peaks associated with the integer and fractional Quantum Hall States.

Finally, spectroscopic studies on the 3D-STI, Bi_2Se_3 found evidence of impurity resonance in the surface state. The impurities are in the unitary limit and the spectral resonances are localized spatially to within ~ 0.2 nm of the impurity. The spectral weight of the impurity resonance diverges as the Fermi energy approaches the Dirac point and the rapid recovery of the surface state suggests robust topological protection against perturbations that preserve time reversal symmetry.

TABLE OF CONTENTS

LIST OF ILLUSTRATIONS AND/OR TABLES

Number *Page*

Chapter 1

Introduction

One of the frontiers in modern condensed matter physics is the physics of strong correlated electronic systems. Among the most celebrated examples of strongly correlated electrons include spin liquids, fractional Quantum Hall (FQH) liquids in two-dimensional electron gases, and high-temperature superconductivity. In these systems, we cannot treat the electrons as independent but we must take into account their correlated behavior. Understanding the electron-electron interactions in these systems is vital to our attempts to explain the complex phenomena associated with these novel states of matter. Another frontier of modern condensed matter physics is the topological materials, where the physical states are no longer categorized by conventional notions of symmetry breaking. The best known examples of such systems are graphene and the surface state of topological insulators.

Given the importance of microscopic interactions to the physical properties of correlated electrons, we employed scanning tunneling microscopy (STM) to study the spatially resolved electronic properties of high-temperature superconducting cuprates and iron-based compounds, with special emphasis on the electron-type $La_xSr_{1-x}CuO_2$, the ferrous superconductor $Ba_1(Fe_{1-x}Co_x)_2As_2$. Additionally, novel physical properties of known topological materials are primarily associated with their surface states. Therefore, this thesis also included applications of STM techniques to the studies of single graphene on multiple substrates, and the three-dimensional strong topological insulator Bi_2Se_3.

As elaborated before, scanning tunneling microscopy provides a unique approach to investigating the electronic and structural properties of strongly correlated electrons and topological materials because of its atomic-scale spatial resolution and its sensitivity to the surface states of matter. STM uses an atomically sharp tip brought within angstroms of a sample, with an applied bias voltage between the two, inducing either electrons or holes to tunnel across the vacuum barrier. It is capable of topographic and spectroscopic measurements with 0.1 angstrom lateral resolution, making it ideally suited to studying nanoscale variations in the conduction (and therefore the density of states), like those observed in superconductors, graphene, and topological insulators.

1.1 Unconventional Properties of High-Temperature Superconductors

The high-temperature cuprate superconductors display the highest known values of superconducting transition temperature, T_C (maximum T_C = 165 K), to date. However, the mechanism of superconductivity remains a mystery, despite much research progress since their discovery by Bednorz and Mueller 26 years ago [1]. Cuprate superconductors, which are extreme type II superconductors, are doped antiferromagnetic (AFM) Mott insulators with strong electronic correlation [2–6]. Mott insulators are influenced by the strong on-site Coulomb repulsion such that double occupancy of electrons per unit cell is energetically unfavorable. The overall consequence of the strong on-site Coulomb repulsion in this scenario is that the materials behave as insulators, [8], whereas electronic band-structure calculations would have predicted them to be metallic. Doped Mott insulators are known to exhibit strong electronic correlations among carriers due to poor screening and have ground

states that are sensitive to doping level. That is, upon doping of carriers, long-range AFM vanishes, spin fluctuations become important, and various competing orders (COs) emerge in the ground state, followed by the occurrence of superconductivity (SC). This is schematically illustrated in Figure 1.1(c) in the doping vs. temperature phase diagrams of both electron- and hole-type cuprates.

A common feature of the cuprates is the presence of CuO_2 planes as shown in Figure 1.1(a–b), with holes or electrons doped into these planes. The pairing symmetry of the superconducting order parameter in the cuprates is found to be unconventional, with many samples exhibiting $d_{x^2-y^2}$-wave (d-wave) superconductivity [9]. However, all cuprates do not exhibit pure d-wave superconductivity. For example, the Ca-doped exhibit doping-dependent pairing symmetry leading to (d+s)-wave symmetry with increasing s-component upon increasing hole doping [10].

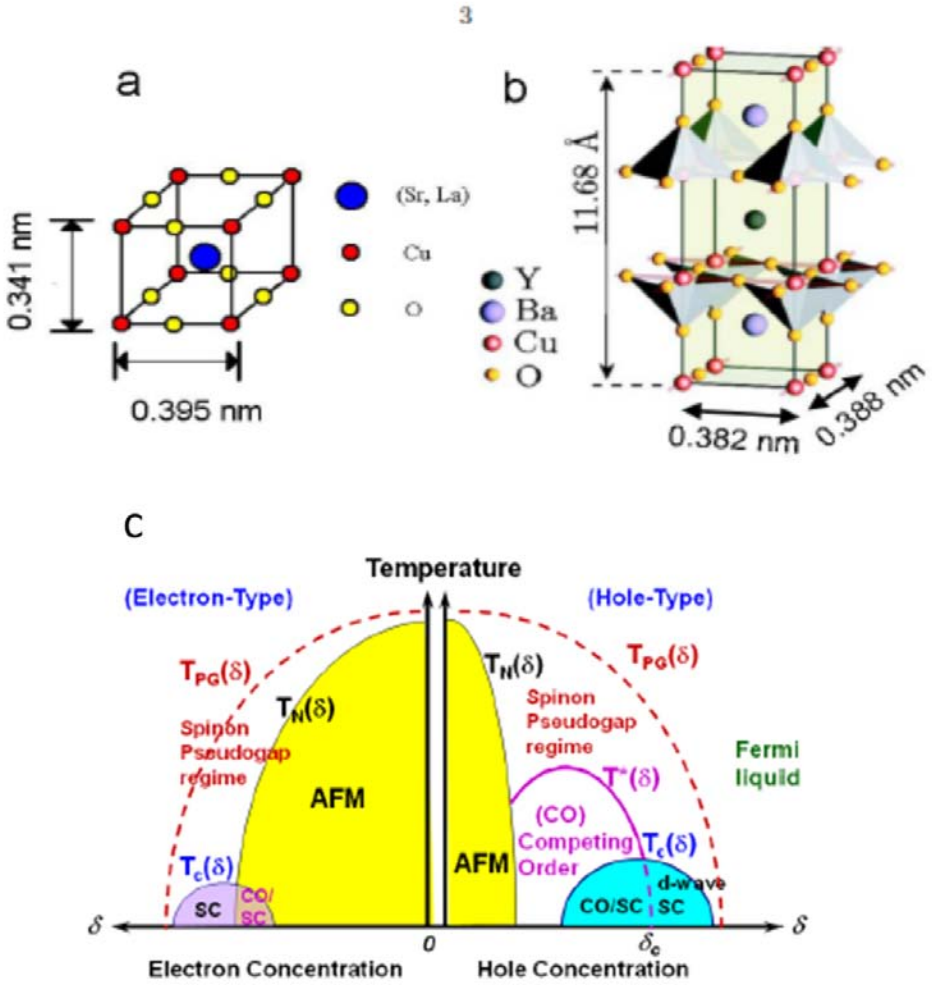

Figure 1.1 (a) Crystalline structure of the infinite layer electron type cuprate $La_xSr_{1-x}CuO_2$. (b) The crystalline structure of hole-type cuprate $YBa_2Cu_3O_{7-\delta}$. (c) The temperature vs. doping phase diagram for the cuprate superconductors. CO: competing order, SC: superconductivity, δ: doping level, T_N: Néel temperature, T_C superconducting transition temperature, T*: low-energy pseudogap (PG) temperature, T_{PG}: high-energy pseudogap temperature. Images modified from [7].

The phase diagram of the cuprates is not symmetric among hole- and electron-type cuprates. The presence of the low-energy pseudogap phenomena on the hole-type side of

the phase diagram is not reproduced on the electron-type side of the phase diagram. The pseudogap is the observation of a soft gap in the quasiparticle density of states spectra that

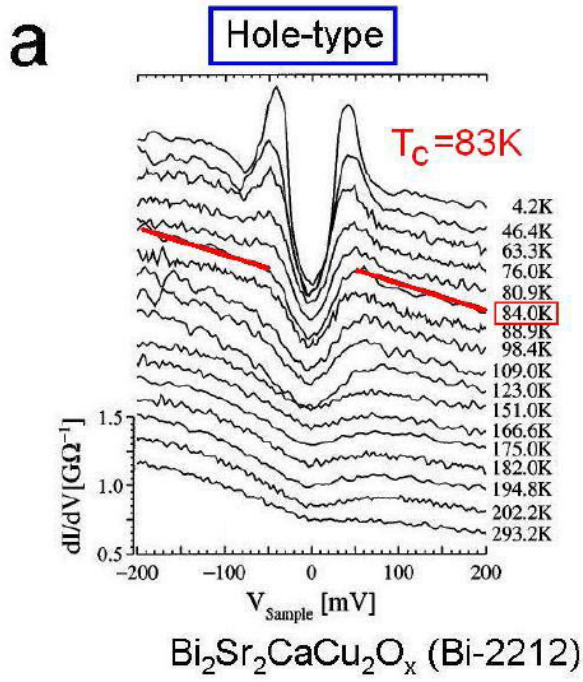

Figure 1.2 : Example of the pseudogap phenomena in hole-type $Bi_2Sr_2CaCu_2O_x$ (Bi-2212) from scanning tunneling microscopy experiments [11].(Figure reproduced from [11]).

persists above T_C in underdoped to slightly overdoped hole-type cuprates [6,7,13–21]. It exhibits no coherence peaks and is referred to as a soft gap because the quasiparticle density of states are suppressed, but nonzero, below the pseudogap energy. Further the pseudogap of the hole–type cuprates persists in a temperature range $T_C, < T < T^*$. In contrast, the AFM region of the phase diagram extends out to meet the superconducting "dome" in electron-type cuprates, while clear separation is observed between the superconducting region and AFM on the hole-type side of the phase diagram, with a pseudogap phase intervening in between.

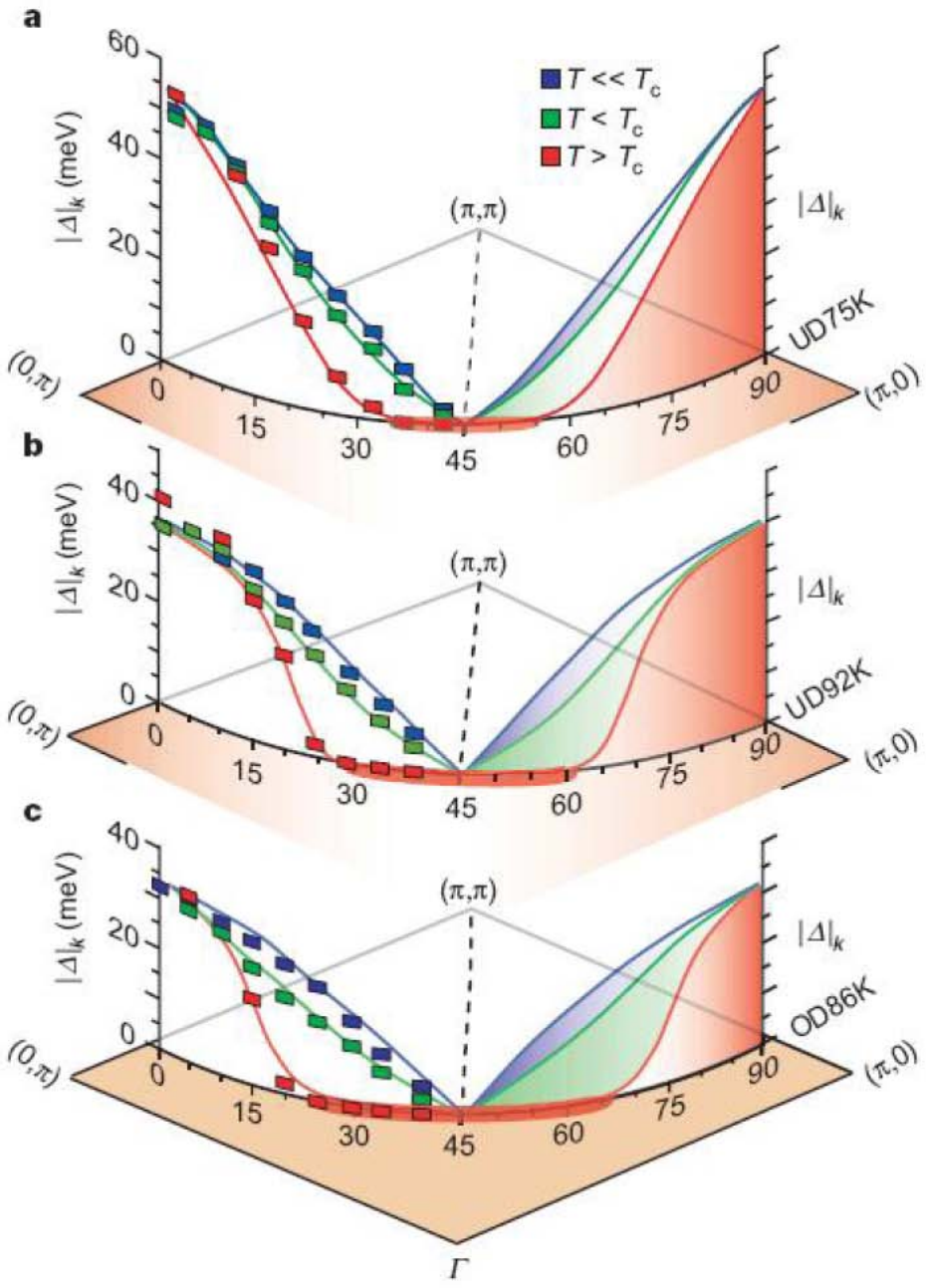

Figure 1.3 : Fermi arc in Bi-2212 with doping dependence: The measured gap-Δ(**k**) values in Bi-2212 along the Fermi surface for different doping levels are shown. (a) Underdoped, T_C = 75 K, (b) Slightly underdoped, T_C = 92 K, (c) Overdoped, T_C= 86 K. Gapped behavior persists near the (π, 0) and (0,π) regions of the Brillouin zone. Image modified from [24].

Although the pseudogap is not observed in the electron doped cuprates, a “hidden pseudogap"-like quasiparticle excitation spectra have been observed under the superconducting dome in doping-dependent grain-boundary tunneling experiments on $Pr_{2-x}Ce_xCuO_{4-y}$ and $La_{2-x}Ce_xCuO_{4-y}$ when a magnetic field $H>H_{C2}$ is applied to suppress superconductivity [22]. It is possible that the pseudogap is present in both hole- and electron-type cuprates and has a nonuniversal energy scale among hole- and electron-type cuprates, such that the pseudogap is effectively hidden under the superconducting dome for electron-type cuprates.

Also absent in the electron type cuprates above T_C is the Fermi arc phenomenon which refers to an incomplete recovery of the full Fermi surface for temperatures in the range $T_C < T < T^*$[23, 24, 25]. This feature manifests as the persistence of gapped quasiparticle spectral density functions near the $(\pi, 0)$ and $(0,\pi)$ portions of the Brillouin zone above T_C in hole-type cuprates.

Many of the asymmetric properties between the hole- and electron-type cuprates can be explained by the differences in the ratio of the SC energy gap (Δ_{SC}) relative to a competing order (CO) energy gap (V_{CO}) and by attributing the origin of the low-energy PG phenomena to the presence of a CO energy gap so that $V_{CO} \sim \Delta_{PG}$. Thus, the presence of the zero-field low-energy PG phenomena in the hole-type cuprate superconductors may be considered as the result of $V_{CO} > \Delta_{SC}$. Conversely the absence of the PG and Fermi arc phenomena in the electron doped cuprates may be attributed to $V_{CO} < \Delta_{SC}$.

This scenario assumes that superconductivity and competing orders are together responsible for the observed unconventional cuprate phenomena. We refer to this scenario

as the “two-gap" model. This scenario supposes that the unconventional phenomena in cuprates may be accounted for by including both Bogoliubov quasiparticles from superconductivity and collective excitations from competing orders to describe the low-energy excitations. Therefore, the unconventional phenomena observed in cuprates are assumed to arise from a ground state of superconductivity and a competing order, and T* is assumed to be the competing order transition temperature, while T_C is the superconducting transition temperature. This CO model will be explored more in Chapter 3.

The existence of various CO besides superconductivity in the ground state of the cuprates may be attributed to the complexity of the cuprates and the strong electronic correlation, which is in stark contrasts to conventional superconductors where SC is the sole ground state. The presence of COs in both hole- and electron-type cuprates has been verified by various experiments including inelastic neutron scattering, muon spin resonances, and angle-resolved photo emission spectroscopy (ARPES) [26–30]. Moreover, theoretical evidences for COs have been provided by analytical modeling and numerical simulations [2–5,31–42] in particular various CO spin density waves (SDW), pair density waves (PDW), *d*-density waves (DDW) or charge density waves (CDW). Recent STS studies of the hole-type $YBa_2Cu_3O_{7-\delta}$ in a magnetic field and of the vortex state spectra have also provided clear evidence for V_{CO} (CDW) > Δ_{SC} [6]. The CO phenomena will be explored more in Chapter 3.

In 2008 a new type of high-temperature superconductors based on iron was discovered [43]. These iron based superconductors also demonstrate many interesting phenomena, although the electron correlation energy is much reduced in comparison to the cuprates. Similar to the cuprates, the ferrous superconductors are type II unconventional

superconductors and are layered materials with magnetic instabilities [44]. Structurally, the iron superconductors form FeX (X = As, P, S, Se, Te) tri-layers that consists of a square array of Fe residing between two checkerboard layers of X [44]. As with the cuprates, where the CuO_2 layers are responsible for superconductivity, the FeX tri-layers provide the same role in the iron-based superconductors. There are four basic types of iron-based superconductors: the "1111", "122", and "111' pnictides and the "11" type iron chalcogenides. Each type of iron superconductor has distinct temperature vs. doping

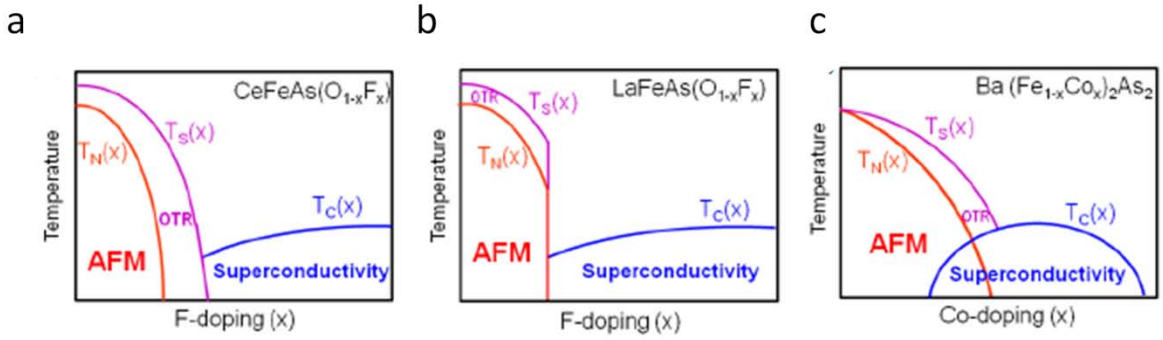

Figure 1.4 :Schematics of three representative phase diagrams for different types of ferrous superconductors. Here $T_S(x)$ denotes the phase boundary for a structural phase transition from a tetragonal phase at $T > T_S$ to an orthorhombic (OTR) crystalline structure at $T < T_S$; $T_N(x)$ is the Néel temperature for the onset of an antiferromagnetic (AFM) phase at $T < T_N$; and T_C (x) represents the doping dependent superconducting transition temperature. Images taken from [44].

phase diagram. Examples of the doping vs. temperature phase diagrams are shown for various compounds in Figure 1.4.

In contrast to the cuprate superconductors whose parent compound is a Mott insulator, the parent compounds of the ferrous superconductors are semimetals [44]. Moreover, as shown by the phase diagrams in Figure 1.3 superconductivity

antiferromagnetic phases may or may not coexist for a range of doping levels. Similar to the competing order phenomena found in the cuprates, AFM phases coexist with SC for the "122" systems. However, much experimental work still needs to be performed to determine the exact overlap of AFM and SC.

The ferrous superconductors are believed to be approximately described by a five band model near the Fermi level and that their Fermi surfaces involve multiple disconnected pockets. The presence of multiple bands and multiple disconnected Fermi pockets suggests that inter-Fermi surface interactions are important to the occurrence of ferrous superconductivity [44]. Calculations have predicted that these superconductors should exhibit two-gap superconductivity.

This possible scenario of CO and SC in two very different superconducting systems motivates our STS studies on La-112 and $Ba_1(Fe_{1-x}Co_x)_2As_2$. Performing comparative studies on both the cuprate superconductors and the iron pnictide superconductors may also shed some light on the elusive pairing mechanism of high-temperature superconductivity. Studies of the cuprate superconductors and the iron-based superconductors will be discussed in Chapter 3 and Chapter 4, respectively.

1.2 Dirac Fermions : Graphene and Topological Insulators

In contrast to the cuprate- and iron-based superconductors covered in Section 1.1, Dirac materials, such as graphene, may often be treated theoretically and experimentally as if the electrons are in the noninteracting regime. Dirac materials exploit the mapping of electronic band structures and an embedded spin or pseudospin degree of freedom onto the

relativistic Dirac equation. An interesting property of the Dirac materials is the protection of Dirac fermions against backscattering. Consequently, this feature of Dirac materials provides an excellent counterpoint to the strongly correlated electron systems of the cuprate superconductors and the lesser correlated system of the iron-based superconductors. These materials include graphene and the surface state (SS) of three-dimensional (3D), strong, topological insulators (STI).

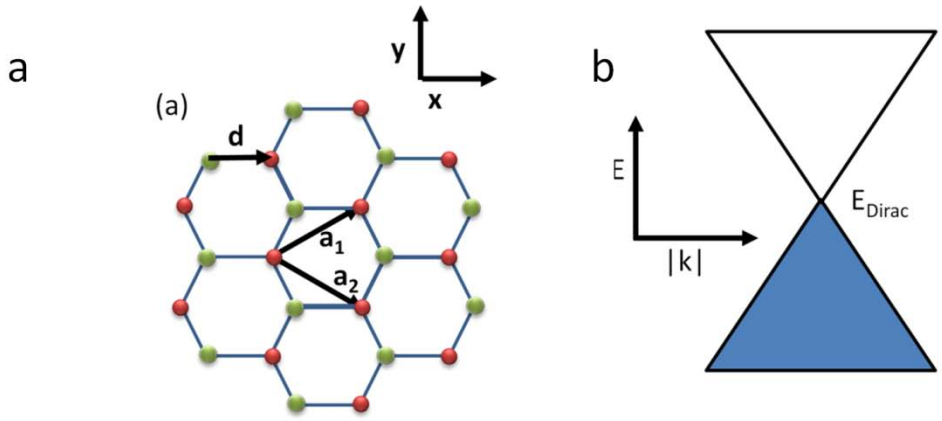

Figure 1.5: Graphene lattice: (a) The real space lattice showing both sublattices with lattice vectors $\overrightarrow{\boldsymbol{a_1}} = \left(\frac{a\sqrt{3}}{2}, \frac{a}{2}\right)$, $\overrightarrow{\boldsymbol{a_2}} = \left(\frac{a\sqrt{3}}{2}, \frac{-a}{2}\right)$, (b) Linear density of states near the K or K' points.

Graphene is a single layer of hexagonally bonded carbon atoms with a Dirac-like energy dispersion relation for small momentum. The structure of graphene is shown in Figure 1.5 Since its isolation in 2004 by A.K. Geim and K. S. Novoselov, graphene has exhibited many remarkable properties, such as Dirac-like band structure, exceptionable physical properties, an ambipolar electric field effect where the concentration of charge

carriers can be tuned continuously from electrons to holes by adjusting the gate voltage [45], exceptionally high mobilities [46–47], the integer and fractional quantum hall effect (IQHE and FQHE) [48–51], and a minimum conductance in the limit of zero charge carriers [52]. The high mobilities make graphene an excellent candidate to be used in components of integrated circuits and may be possible that graphene will become an important supplement to future silicon-based technologies.

However in order to make practical use of graphene in technology, graphene manufacture must be capable of producing large, high-quality graphene sheets in a timely fashion. The original method of graphene production of mechanically exfoliation is simply not feasible. Consequently much experimental effort has been put into finding more efficient means of graphene fabrication of high-quality, large-area graphene sheets and still maintaining the superior electronic characteristics of graphene while in contact with various gate dielectrics and substrates. There have been significant efforts towards synthesis of large area graphene, including ultra-high-vacuum annealing to cause desorption of Si from SiC single crystal surfaces, the deposition of graphene oxide films from a liquid suspension followed by chemical reduction, and chemical vapor deposition (CVD) on transition metals [52–63] such as Ru, Ni, Co, Pt, and Cu.

However, the electronic properties of graphene exhibit significant dependence on the surrounding environment and high susceptibility to disorder because of the single layer of carbon atoms that behave like a thin membrane and because of the fundamental nature of Dirac fermions [45]. Consequently, graphene's interaction with its surrounding environment provides a unique opportunity to study the effects how strain and substrate can perturb a gas of noninteracting Dirac-fermions. For example, nonuniform strain has been

predicted to generate pseudomagnetic fields in graphene lattices and therefore give rise to integer and fractional quantum hall states. In the case of the fractional quantum hall states, however, we must abandon our notion of noninteracting Dirac fermions. The basic physical properties of graphene will be reviewed in Chapter 5. The interaction of graphene with its substrate and disorder will be covered in more detail in Chapter 6.

In addition to graphene, the recent discovery of three-dimensional strong topological insulators also provides a unique opportunity to study Dirac fermions and their interactions with quantum impurities. Topological insulators in two or three dimensions have a bulk electronic excitation gap generated by a large spin-orbit interaction, and gapless edge or surface states on the sample boundary[64]. A novel feature of these TIs is the suppression of backscattering of Dirac fermions due to topological protection that preserves the Dirac dispersion relation for any time-reversal-invariant perturbation. However, while direct backscattering is prohibited in the SS of 3D-STI, sharp resonances are not excluded because Dirac fermions with a finite parallel momentum may be confined by potential barriers [65]. In fact, theoretical calculations for Dirac fermions in the presence of noninteracting impurities have predicted the occurrence of strong impurity resonances [66, 67].

Overview

This thesis is structured into three parts, as follows. In Chapter 2 we will first present the theory of STM technique and instrumentation. In the second portion we will cover STM studies of two different superconductors. In Chapter 3 we will review the physics of electron-type cuprate superconductors in the context of the coexistence of SC

and CO in the ground state, and present magnetic-field-dependent studies of electron-type polycrystalline $La_xSr_{1-x}CuO_2$. In particular we will present quasiparticle tunneling spectral evidence for the existence of commensurate SDW as the CO to superconductivity, as well as present evidence for the first observation of vortices in an electron type cuprate superconductor. In Chapter 4 we cover the basic electronic and structural properties of ferrous superconductors, and present field-dependent STS studies on $Ba_1(Fe_{1-x}Co_x)_2As_2$ single crystals. We find supporting evidence for sign-changing, s-wave, two-gap superconductivity and observe a pseudogap-like feature inside the vortex core.

In the final section we will cover STS studies of two Dirac materials. In Chapter 5 we present the basic electronic properties of graphene and the effects that strain and substrate may have on the density of states of graphene. In Chapter 6 we report on our STS measurements on graphene, particularly the first observation of quantized conductance peaks due to pseudomagnetic fields in strained graphene. In Chapter 7 we present evidence for unitary scattering from quantum impurities in the topological insulator Bi_2Se_3. Finally, in Chapter 8, we conclude with the overall review and discuss possible future work. In Appendix A we include designs for the molybdenum body STM head which replaced a macor body STM head on the probe. Additionally, in Appendix B, Matlab programs for the analysis of tunneling spectra are included.

Chapter 2

Instrumentation

Scanning tunneling microscopy (STM) is a useful and powerful technique to perform noncontact, localized, structural and spectroscopic measurements. Capable of resolving microscopic features ranging in size from 10 microns to 0.1 angstroms, STM has excellent resolution in both topographic and spectroscopic studies. In this thesis we use scanning tunneling spectroscopy (STS) to study the effects of nontrivial strain on the local density of states (LDOS) in graphene, the effects of localized nonmagnetic impurities on the surface state of topological insulators, and to probe the nature of the superconducting gap and low-energy quasiparticle excitations in the iron-based superconductors. Included in its advantages are ultra-high vacuum ($< 10^{-10}$ torr), large magnetic fields (up to 7 Tesla), liquid helium temperatures, and high-energy resolution exceeding 0.05 meV, which enable thorough investigations of the many systems of scientific curiosity.

In order to achieve the atomic resolution necessary for this thesis, the STM probe requires sophisticated equipment and extremely small operational noises. We will describe the STM setup and operational equipment later on in the chapter. However typical tunneling currents measured are on the order of 1 nA to 10 pA with the required signal-to-noise ratio of 1000-to-1. This requires, for most measurements, a base noise level below 1 pA and a precise motor control of the tip-sample separation distance. To meet these

requirements, piezo-electrics are employed to supply the fine motor control of the tip-sample separation distance. Additionally, acoustic, vibrational, and electronic noises must be minimized. The typical piezo-electric crystals used in this thesis provide a 1 nm/V resolution for the motor control. The average tunnel junction resistance defined as the bias voltage divided by the tunneling current, $R_{junction} = V_{Bias}/I$, was on the order of 1 ~ 5 GΩ for the majority of samples.

2.1 Theory and Principles

The technique of STM first demonstrated by Gerd Binning and Heinrich Roehr, in 1982 [68] is largely based on a quantum mechanical process. A conducting probe tip (usually metallic and made from Pt-Ir or W) is attached to a piezo-electric drive that is capable of three-dimensional movement and is by use of the piezo-drive brought to within several angstroms of the sample surface. At this distance the wave-functions of the probe tip will overlap with the wave-functions of the sample surface so that as a bias voltage is applied across the sample, a tunneling current will develop. Electron tunneling is dependent on the bias voltage, tip-sample separation distance, and of the availability of the density of states in both the probe and the tip. The tunneling current, usually between micro-amps and femto-amps, is then amplified by means of a current amplifier and compared to the target tunneling current. The difference is then used to in a negative feedback system to drive the vertical motion of the z-piezo, and by this means a stable tunnel junction is formed with both lateral and vertical subangstrom resolution. This principle of operation is demonstrated in Figure 2.1.

Following Wiesendanger's approach [69], the tunneling current can be determined with a 1st-order perturbation method from its dependence on bias voltage, and the DOS of both the sample and tip which yields

$$I = \frac{4\pi e}{\hbar}\int_{-\infty}^{\infty}[f(E_F - eV + \epsilon) - f(E_F + \epsilon)] \times \rho_S(E_F - eV + \epsilon)\rho_T(E_F + \epsilon)|T|^2 d\epsilon \quad 2.1$$

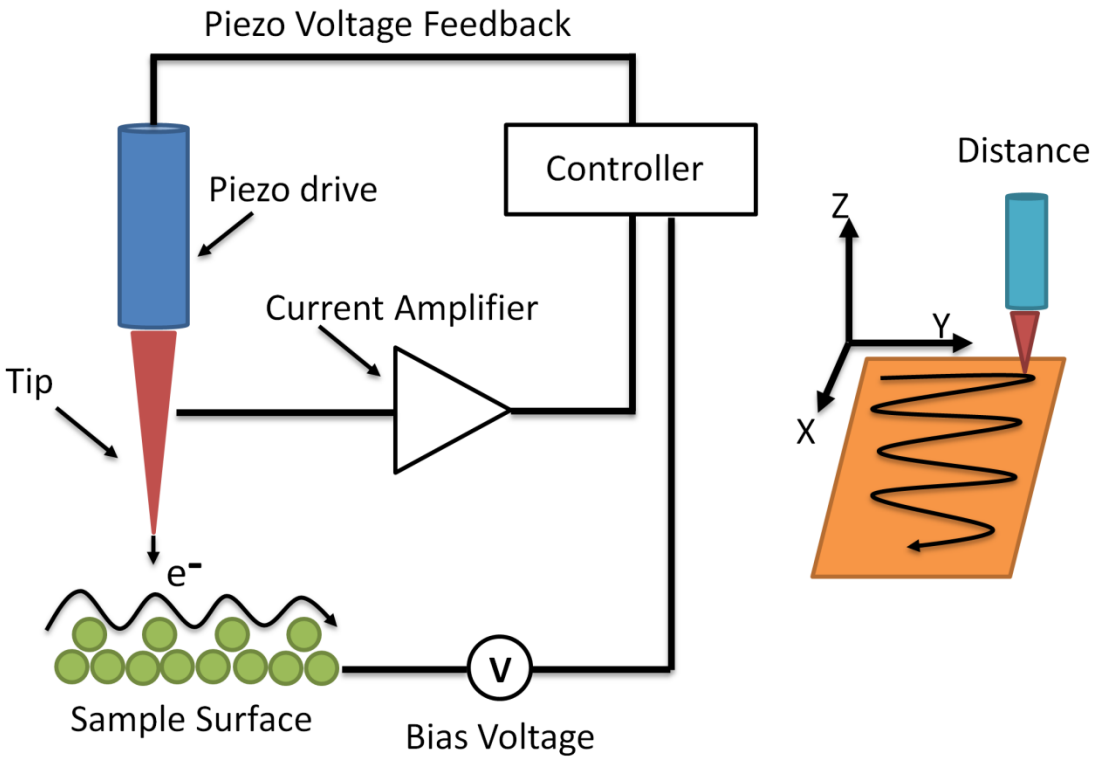

Figure 2.1: Basic demonstration of the principle of STM operation. A bias voltage is applied and the STM tip is brought within several angstroms of the sample surface until the desired tunneling current is detected. The topography is determined by plotting either the voltage feedback to the piezo tube scanner or by measuring the changes in the tunneling current, depending on the operational mode of the STM.

where $f(E)$ is the Fermi distribution function, $f(E) = \{1 + \exp[(E - E_F)/K_B T\}^{-1}$, $\rho_S(E)$ and $\rho_T(E)$ are the DOS for the sample and the tip, respectively, and T is defined as

the tunneling matrix and is a surface integral on a separation distance between the tip and the sample [70]

$$T(eV,\epsilon) = \frac{\hbar}{2m}\int d\boldsymbol{S}\cdot(\chi^*\nabla\psi - \psi\nabla\chi^*) \qquad 2.2$$

where χ and ψ are the wave-functions for the tip and the sample, respectively. The rate of electron transfer is determined by the Fermi golden rule [71]. Eqn. 2.2 can be simplified according to [72]

$$T(eV,\epsilon) \propto e^{-2(d-r)\left(\frac{2m}{\hbar^2}\left(\frac{\phi}{2}-\frac{eV}{2}\right)\right)^{\frac{1}{2}}} \qquad 2.3$$

where d is the tip-sample separation distance, r the radius of the probe tip, and ϕ the convoluted work function of the probe tip and sample. The tunneling matrix depends exponentially on the tip-sample separation distance; as a result, small changes in the vertical height of the tip can result in large changes in the tunneling current, making the current a sensitive measure of tip-sample distance. If K_BT is smaller than the energy resolution of the experiment, the Fermi distribution can be approximated to a step function resulting in

$$I = \frac{4\pi e}{\hbar}\int_0^{eV}\rho_S(E_F - eV + \epsilon)\rho_T(E_F+\epsilon)|T|^2 d\epsilon \qquad 2.4$$

If the current, I, is differentiated with respect to the bias voltage, eV, and we assume that the probe tip (Pt, W) is metallic and has a constant density of states (DOS) over the measurement voltage range, that is, $\partial\rho_T/\partial V \propto 0$, then

$$\frac{dI}{dV} \propto T(eV,\epsilon=eV,d)\rho_T(0)\rho_S(eV) + \int_0^{eV}\rho_S(eV+\epsilon)\rho_T(\epsilon)\frac{dT(eV,\epsilon,d)}{dV}d\epsilon. \qquad 2.5$$

Further if the tunneling matrix, T, behaves monotonically and smoothly with respect to the bias voltage then the final integral can be neglected. The differential conductance can be approximated to

$$\frac{dI}{dV} \propto T(eV, d)\rho_T(0)\rho_S(eV) \quad \text{or} \quad \frac{dI}{dV} \propto \rho_S(E_F - eV). \tag{2.6}$$

Therefore physical information concerning the DOS of the sample can be extracted from the differential conductance making STS an effective probe of the sample's electronic structure. This concept is demonstrated graphically in Figure 2.2. For this thesis, all samples were investigated with Pt-Ir tips, satisfying the above approximations.

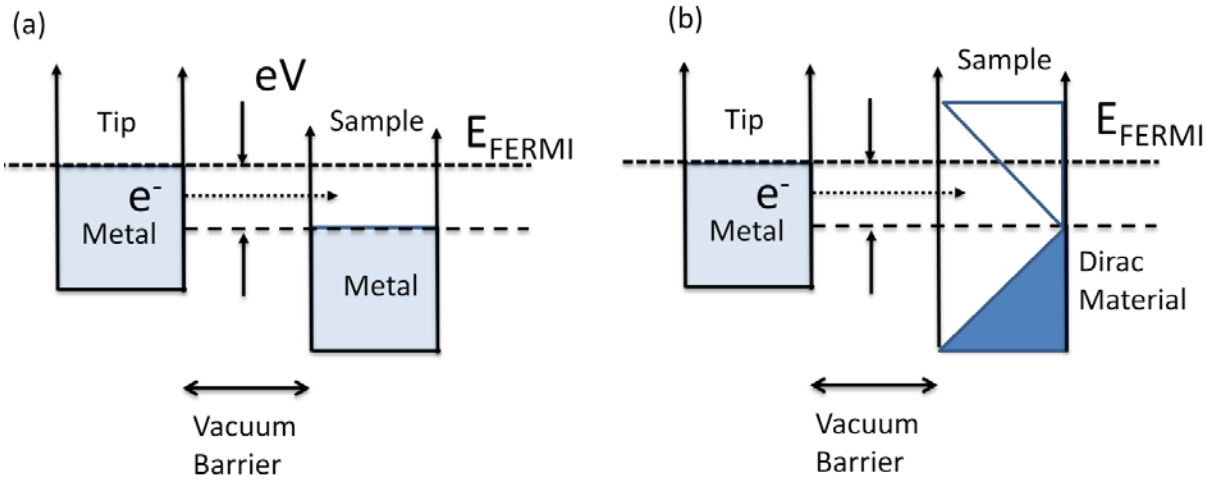

Figure 2.2: Graphical representation of quantum tunneling between two systems. Vertical axis is energy and the horizontal axis is energy: (a) Quantum tunneling between two metals at T=0 K. In both cases the DOS of states are constant. The Fermi level is designated by $E_{FERMI.}$ (b) Quantum tunneling between a metallic tip (Pt/Ir or W) and a Dirac material (graphene). If there are no available states to tunnel into then the tunneling current is zero.

2.1.1 Operational Modes

In this thesis we concern ourselves with three modes of STM operation: constant height imaging, constant current imaging, and constant tip-junction resistance spectroscopy. The primary difference between the first two modes of operation depends on the settings of the feedback control of the STM. As previously mentioned, when the tip-sample separation distance is reduced and a bias voltage is applied, a tunneling current begins to flow which depends exponentially on the tip-sample distance. The tunneling current is then amplified by a current amplifier and sent to the STM controller where it is compared to a target current value. The difference is used in a negative feedback system to drive the z-direction of the piezo-motor controlling the tip-sample separation. The gain and time constant, τ, of the feedback loop determine the ability of the system to respond quickly to changes in the topography of the sample. For the feedback to respond to rough contours in the sample surface the gain and time constant must be optimized, otherwise the tip will crash into the surface, damaging either the sample or resulting in changes in the tip. However, manually controlled touching of the tip to a sample surface can be used to reshape an unfavorable tip geometry to a more favorable one. Necessarily, scan speed is also important to consider when optimizing the gain and time constant. If the scan takes too long, the topography, while allowing the system to average out higher-frequency perturbations, will be susceptible to low-frequency noise. If the scan is too fast then the feedback cannot respond adequately to changes in the topography. Incorrect settings in the feedback can cause false topography images, stressing the importance of feedback optimization.

The first mode, constant height imaging, is achieved by turning off feedback or by increasing the time constant to very long time scales, effectively preventing the system from responding to changes in contours save for long length-scales. With feedback disabled and a constant bias voltage maintained across the tip and sample, the tip is scanned across the sample and only changes in the current are recorded. Due to the exponential dependence of the current on tip-sample distance, the current reflects the "relative distance" of the sample compared to the tip [73]. The relative topography, $z(x, y)$, is determined by the changes in the current. Actual height must be determined from constant current mode. The danger of constant height mode lies that the tip cannot respond to rapid changes in the topography. If the sample's height varies more than the tip-sample separation, it is possible to crash the tip into the sample causing, damage to both, or, for the tip-sample distance to increase, causing the tunneling current to fall below a measureable level for the electronic detection equipment. The benefits of this mode is the relaxation of feedback optimization allowing the STM to perform scans very rapidly, which is limited only by the response time of the current amplifier, the maximum scan speed of the STM tip head (is determined by its lowest mechanical resonance mode), and the data acquisition rate of the STM controller. The Nanonis controller used for this thesis is capable of recording $>10^4$ data points a second, allowing a 100 pixel by 100 pixel scan to occur in just over several seconds. Images taken faster than this rate were found to lose contrast. As an additional advantage is the ability to scan the topography rapidly, this approach allows the researcher to ignore low-frequency noises, ~ < 20 Hz, such as building vibrations or low-frequency mechanical motors, such as the elevator in the Sloan basement.

The second operation mode, constant current, relies on the negative feedback circuit of the STM to maintain a constant tip-sample separation distance and therefore maintains a constant tunneling current. As with the constant height mode, the constant current mode requires the bias voltage remain constant. Topography of the surface, $z(x, y)$, is determined by the voltage applied to the z-component of the piezo tube scanner multiplied by the voltage-to-nm calibration of the piezo tube scanner. This is the preferred method of capturing atomic resolution images or nanostructures such as the images of graphene and silicon nanopillars shown in Figure 2.3. As previously mentioned, the STM feedback and STM scan speed must be optimized to prevent the tip from crashing into the

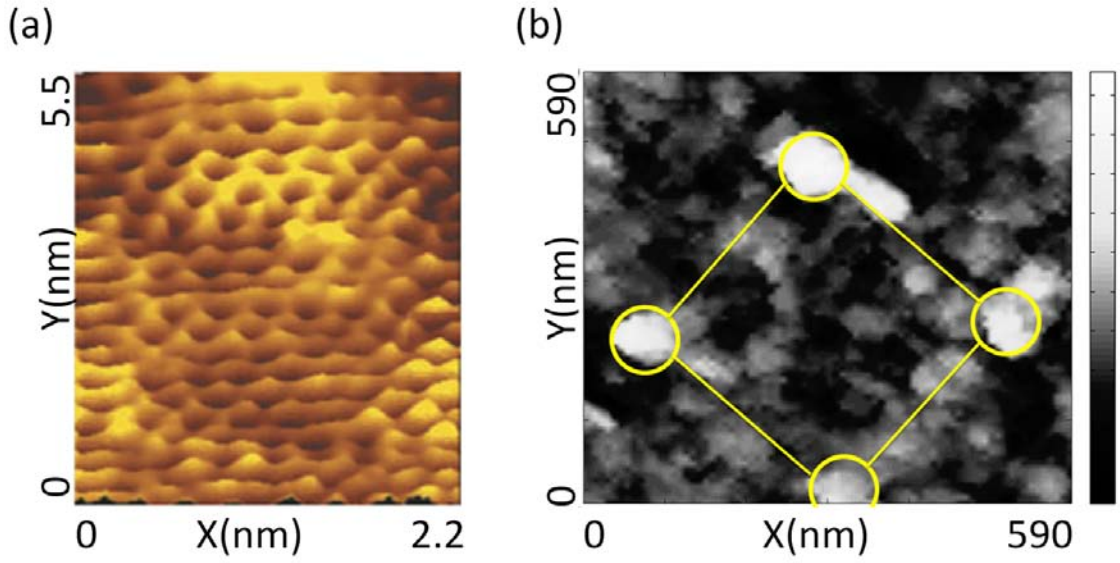

Figure 2.3: Scanning tunneling microscopy topography images of (a) atomically resolved topography on mechanically exfoliated graphene at temperature, T = 77 K, and (b) micron scale topography of silicon nanopillar arrays at temperature, T = 296 K, after chemical etching to remove oxide around the pillars

sample and to allow the tip to respond as rapidly and as accurately as possible to changes in the sample topography. Failure to do so can result in false images or numerous tip changes.

The final mode of STM operation, constant tip-junction resistance spectroscopy, attempts to measure the current vs. voltage, $I(V)$ vs. V, and the differential conductance vs. voltage, $\frac{dI}{dV}$ vs. V, characteristics of the sample. As previously mentioned the DOS of a sample can be related to the differential tunneling conductance, $\frac{dI}{dV}(V)$, with respect to voltage for well-behaved samples and STM tips. In this mode at the point of interest, a stable tunneling junction is established at the determined junction resistance, $R_{junction} = \frac{V_{Bias}}{I}$, with the STM feedback circle enabled. During an initial wait time the tip-sample separation distance is stabilized with constant bias-voltage and constant tunneling current. This initial stabilization period is on the order of a few ~ 100 μs. Once a stable tunnel junction is established, the STM feedback circuit is disabled and the bias voltage is ramped from an initial value to a final value, while the $I(V)$ and $\frac{dI}{dV}(V)$, are recorded for that precise location of the sample. The STM feedback circuit is re-enabled at the previous bias voltage and tunneling current. Constant tip-junction resistance spectroscopy can be repeated at every pixel of an $m \times n$ scan to create a conductance map scan. At every pixel, a stable tunnel junction is established at exactly the sample tunnel junction resistance, the feedback disabled, and bias-voltage varied. The feedback is reestablished, the tip is translated to the next pixel in the scan and the process is repeated. This combines the high spatial resolution of topography scans with spectroscopy information. One can achieve atomic resolution in investigating spatial variations of the local density of states. For the materials considered in this thesis, constant tip-junction resistance spectroscopy roughly eliminates the dependence of surface topography in the spectroscopy scan because at every

location the scan is performed at the same tip-sample separation distance for a relatively flat sample surface. High-voltage crosstalk from the voltage feedback to the piezo tube scanner is eliminated by disabling the STM feedback circuit during the spectroscopy scan. Also as shown in [74], in certain samples taking the normalized conductance, $\frac{dI}{dV} / \frac{I}{V}$, can eliminate the effect of the tunneling matrix, T, when measuring the LDOS of the sample.

In this thesis, two methods were used to measure the differential tunneling conductance, $\frac{dI}{dV}(V)$, directly with the use of a lock-in amplifier and indirectly by numerically calculating the differential conductance, $\frac{dI}{dV}(V)$, from the current, $I(V)$. In order to measure $\frac{dI}{dV}(V)$ directly with a lock-in amplifier, a small ac modulation is added to the base bias voltage V_0. The frequency of this modulation should be significantly above the cutoff frequency of the feedback loop to avoid damaging the tip. If we assume that the V_0 is swept slowly with time and the ac modulation is small in comparison, we can Taylor expand the tunneling current around V_0

$$I(V) = I(V_0 + v\cos\omega t) \tag{2.7}$$

$$I(V) = I(V_0) + I'(V_0)v\cos\omega t + \frac{I''(V_0)}{2!}(v\cos\omega t)^2 + \cdots . \tag{2.8}$$

For small amplitudes of v the first derivative will be proportional to the first harmonic term, the second derivative will be proportional to the second harmonic term, and so on. To perform a spectroscopy scan, one must measure the first harmonic term using a lock-in amplifier while slowly performing an $I(V)$ vs. V measurement. The lock-in amplifier substantially reduces frequency-dependent noise in the data. However, when choosing a modulation frequency, care must be taken to avoid low frequencies and harmonics of 60

Hz. A problem of this method is the need to wait a time τ dependent on the time constant of the lock-in amplifier after changing the bias voltage before recording $I(V)$ and $I'(V_0)$. Unfortunately this drastically increases the time needed to perform a spectroscopy measurement.

In contrast, the differential conductance can be numerically calculated directly from $I(V)$ vs. V. A tunnel junction is established at the given tunnel junction resistance, the STM feedback circuit is disabled and the bias voltage is swept while the resulting tunneling current is measured directly. Using mathematical analysis programs the differential conductance is then numerically calculated. The Matlab analysis programs used in this thesis are detailed in Appendix B. This approach is exemplified in Figure 2.4.

The primary advantage of this method is the speed at which constant tip-junction resistance spectroscopy maps can be taken, which is an important concern when the measurements are being taken at low temperatures. As detailed later in this chapter, magnetic field measurements using the superconducting magnet must be completed in 3 days due to limited liquid helium capacity of the dewar. However this method is more susceptible to noise contamination than the lock-in technique and care must be taken to avoid creating artifacts in the $\frac{dI}{dV}(V)$ curves due to taking the numerical derivative of discrete data. For this thesis the $I(V)$ vs. V method was the preferred method for finding the differential conductance. In the next section we will describe the STM instrumentation used in performing these measurements.

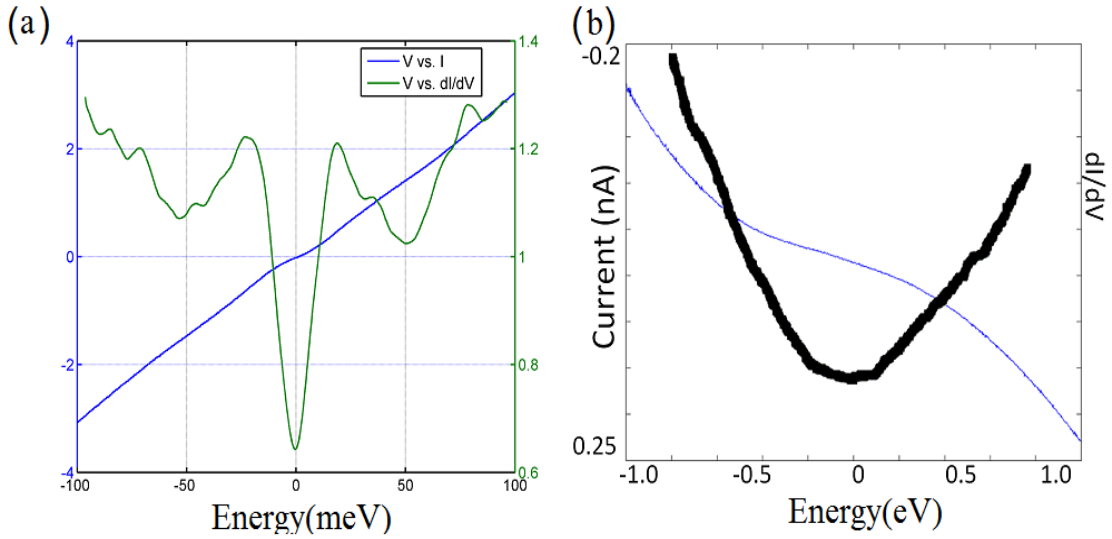

Figure 2.4: Numerical calculation of the differential conductance from $I(V)$ vs. V curves: (a) $I(V)$ vs. V curve of the cuprate superconductor YBCO with the numerically calculated $\frac{dI}{dV}(V)$ at T=7 K. (b) $I(V)$ vs. V curve of CVD grown graphene on copper foil with the numerically calculated $\frac{dI}{dV}(V)$ at T = 77 K.

2.2 Instrumentation

2.2.1 STM Probe

The requirement of bringing the STM probe tip to within angstroms of the sample surface requires a complicated and an optimized feedback circuit as described earlier. However, this step alone is not sufficient for measurement of the materials considered in this thesis. The STM must also include vibration isolation, acoustical and electronic noise reduction, and specialized electronics to amplify, shield, and filter the currents and voltages needed. In addition, temperature control and measurement, large magnetic fields, ultra-high vacuum, and cryogenic systems are required, and high-quality STM tips as well as clean sample surfaces were crucial for the measurements in this thesis. In this section we will describe the STM in detail along with the support systems.

The microscope used in this thesis was previously designed and built by Ching-tzu Chen and Nils Asplund [75]. The basic overview of the STM probe is shown in Figure 2.5. The STM consists of the STM probe head, the cryogenic probe, and the vibration isolation table. The STM probe head consists of the piezo-electric tube scanner which provides fine X,Y, and Z motion, course Z-approach stage, the tip and sample. The probe head was later modified by Andrew Beyer and the author to possess a course motion X-Y sample stage and in fall 2011 the macor body of the STM head was replaced with a molybdenum body.

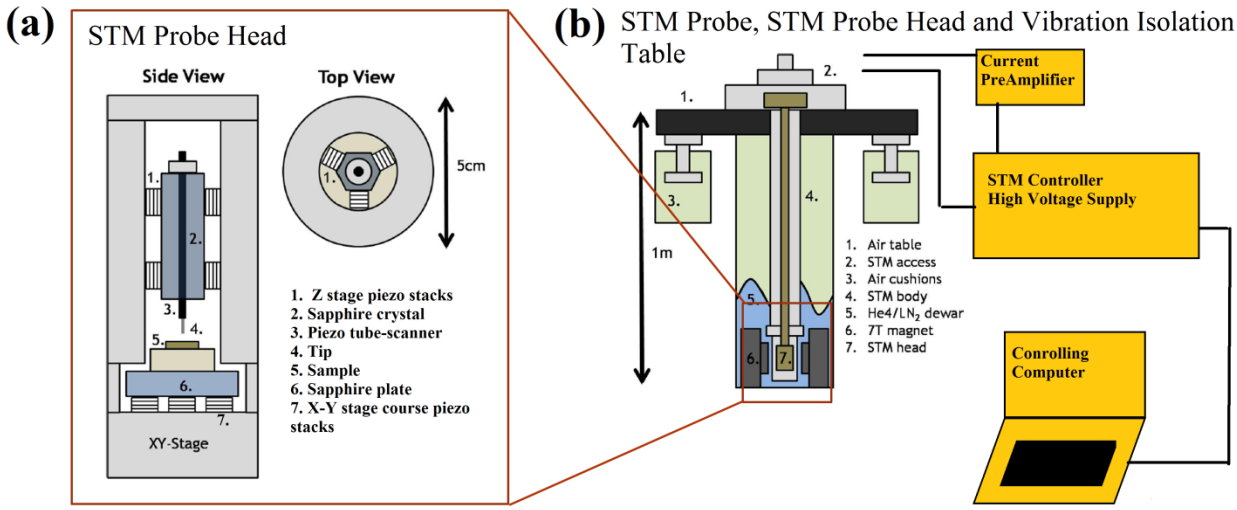

Figure 2.5: Schematic showing the generalized layout of the STM probe, STM jacket, STM dewar, the vibration isolation system, and the support electronics. (a) The STM head with tube scanner, both Z and XY course movement stages, the tip and the sample. (b) The STM probe inserted into stainless steel vacuum jacket which is mounted in the Oxford cryogenic dewar where the liquid helium, liquid nitrogen or nitrogen gas can contact the vacuum jacket. The Oxford dewar is set on a three-inch-thick aluminum plate mounted on four air-damped pneumatic legs to reduce mechanical vibrations.

The STM tips used in this thesis were Pt-Ir, consisting of 90% platinum and 10% iridium, and were made primarily via mechanical shearing followed by electrochemical etching to polish the tip [76]. The tips were mechanically cut from 10 mil Pt wire until they were optically sharp, as observed under an optical microscope. The cut tips were then

electrochemically etched for approximately 10 seconds in a solution of 35 grams of $CaCl_2 2(H_2O)$, 200 ml of de-ionized water , and 10 ml of acetone at 10–15 V_{AC} using a common variac. The mechanically cut tips were immersed into the solution to a depth of 1-3mm. Early investigations were also made into the feasibility of using Pt and Ni tips made with a two-stage chemical etching process [77]. For mechanically exfoliated graphene samples, only Pt-Ir tips made using the two-stage chemical etching process exhibited the necessary optical sharpness needed to align the tip and sample. STM tips used in this thesis were tested on HOPG graphite for atomic resolution and clean tunneling conductance spectra followed by cleaning on a gold sample surface as demonstrated in [78]. After the tips were made and cleaned in an ethyl alcohol bath they were loaded into the tip holder as shown in Fig 2.6.

The tip holder is connected to the piezo-electric tube scanner which provides fine motion control required for sub-angstrom resolution. The piezo-electric tube scanners as show in Figure 2.6 are cylindrical and coated in gold on both the interior (the z-piezo voltage connection ,V_Z) and exterior of the tube which is divided into four quadrants on the exterior (V_x, V_{x-} , V_y , V_{y-}). The four quadrants can be sheared simultaneously to control tip-sample separation distance, while the x, x- or y, y- quadrants can be sheared oppositely to scan the tip along the x or y directions. Shearing occurs when a voltage is applied between the inner surface of the tube scanner, V_z, and any of the other quadrants. By controlling all possible linear combinations of shearing motions using the STM controller, the tip may be scanned and the tip-sample separation controlled for all the modes of STM operation. At room temperature the piezo-electric tube scanner has a max lateral scan range of 10 micron which is reduced to 3 microns at liquid helium temperatures

using the Nanonis controller, and a max vertical extension and retraction distance of 1.0 micron at room temperature and 0.5 microns at 4.2 K.

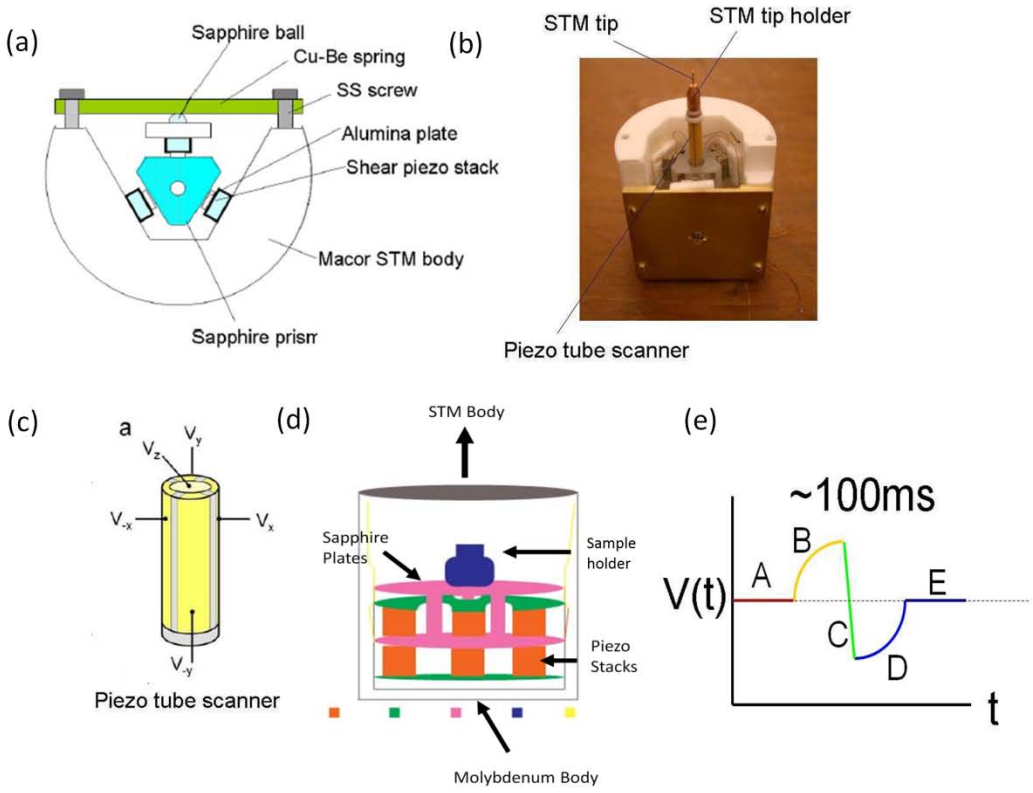

Figure 2.6: Schematic images of the STM head probe, tube scanner and course stages. (a) Schematic top view of the macor/molybdenum STM head. Six piezo stacks capped by smooth alumina plates, hold a sapphire prism in the Z-stage design. Voltages may be applied to the shear piezo stacks to move the sapphire prism. The STM tip holder, STM tip, and piezo tube scanner all connect to the sapphire prism so that when it moves, the STM tip and piezo tube scanner move with it. (b) Image of the STM head as shown in (a). (c) Schematic representation of the tube scanner showing four separate quadrants (V_x V_{x-} V_y V_{y-}) on the exterior with the interior being $V_{Z.}$ (d) Schematic drawing of the course X-Y stage. Voltages applied to the piezo stacks can shear the sapphire plate in either the x-direction or the y-direction by having half the piezo crystal rotated 90 degrees out of phase with the others. Maximum motion of the sample is 1.0 mm in any direction. (e) Illustration of the voltage waveform applied to each piezo stack to take one course step. Polarity direction maybe reversed to take a step in the reverse direction. Image modified with permission from A. Beyer [79].

The sample is mounted on the sample holder which consists of a 1.0-cm-diameter OFHC copper cylinder 1.0 cm in height, which is itself mounted on a sapphire plate of the course X-Y movement stage. The samples are attached to the copper block by means of silver epoxy, silver glue or by a metallic clip depending on whether the sample bulk is conductive. Temperature control of the sample above cryogenic temperatures is achieved by a small resistive heater located between the sapphire plate and the copper cylinder. Actual temperature control is maintained by a Lakeshore 340 Temperature controller. The temperature of the sample block is measured using a Cernox calibrated resistor. As will be described later on sample preparation depends on the sample in question. For air sensitive samples, the sample would be loaded onto the sample stage in an argon environment in a glove box.

The course X-Y stage is show in Figure 2.6. The course X-Y stage allows one to investigate large arrays of nanostructures that exceed in size the maximum scan range of the tube scanner or to avoid nonoptimal regions of the sample surface such as an amorphous carbon region of a CVD grown graphene sample. The motion of the X-Y stage is accomplished through the use of six shear piezo-electric stacks based on the slip and stick principle. Three beryllium copper springs provide the tension to hold the sapphire plate firmly against each stack. The stacks are sheared by applying a slowly increasing the voltage to each stack. The stacks shear together slowly enough that the sapphire plate moves with the stacks due to friction. Suddenly the voltages to each stack are rapidly reversed, causing each stack to shear in the opposite direction, whereas the sapphire plate slips against each stack due to the rapid change and remains in its position. Lastly the voltage to each stack is removed and the stage returns to its original state but with sapphire

plate having translated a small distance ~ < 1.0 micron along the shear direction. The max voltage applied during each step is 200 V and maximum of 3 steps per second can be taken. The corresponding voltage waveform is shown in Figure 2.6(e).

Similar in operation is the course Z-stage except that it translates the tip holder and tube scanner vertically by a course distance of ~ 0.2–1.0 micron, depending on temperature. The tip holder and the tube scanner are connected to a sapphire prism instead of a sapphire plate and is held between the six piezo stacks firmly by a single beryllium copper plate. During approach the STM will take exactly one course step forward and then the piezo-electric tube scanner extends forward to see if the tip is within range to generate a measurable quantum tunneling current. If a threshold tunneling current is not detected, the coarse step is repeated.

The STM head is attached to the end of a cryogenic probe and is loaded into a stainless steel vacuum jacket containing a cryogenic charcoal pump at the base. Unfortunately only ultra-high vacuum can be achieved at liquid helium temperatures by use of the charcoal pump. The probe is pumped down to < 10^{-6} torr at room temperature by an Alcatel ATP150 turbo-molecular pump and the pressure is measured using Alpert-Bayard ion gauge with Perkin Elmer Digital Gauge controller. At liquid helium temperatures (T = 7 K) the charcoal pump reduces the pressure in the STM to ~ 10^{-9} torr.

The STM probe and jacket is mounted in an Oxford cryogenic dewar with a 7 T superconducting magnet with a three-inch-bore radius. The dewar holds 40 liters of helium, with a boil-off rate of ~ 10 liters per day, allowing for 3 days, magnetic field measurements with a full dewar of helium. Helium level is determined by use of a superconducting resistor inside the dewar. Depending on the required temperature, the dewar is filled with

ambient nitrogen gas for 300 K, with liquid nitrogen for 77 K, or with liquid helium for 7 K. The dewar is attached to a three-inch-thick aluminum plate situated on four pneumatic air dampener legs to isolate the system from building and mechanical vibrations, with added lead bricks and shot to balance the load on the pneumatic legs. In addition the dewar is housed inside an acoustical dampening box located in a room lined with acoustic dampening foam. More details on the vibration isolation and the cryogenic dewar can be found in A. Beyer's thesis [79].

If the tip is within a range of the sample surface to generate a measurable quantum tunneling current, the current is filtered by an RF copper grain filter[80] located on the cryogenic probe above the STM head. The current is then amplified by a FEMTO pre-amplifier, model # DLPCA-200, located outside the stainless steel jacket at the top of the STM probe. The feedback circuitry and current detection is managed by the support electronics which initially consisted of an RHK SPM-100 SPM controller, a PMC-100 piezo motor, a RHK pre-amplifier and controlling computer. These were eventually replaced by a Nanonis RC4 controller, a Nanonis PMD piezo motor controller, a Nanonis HV4 high-voltage supply, and a controlling computer. All support electronics are powered by separate clean power outlets.

Chapter 3

Scanning Tunneling Spectroscopic Studies on the Electron-Type Cuprate Superconductor $La_{0.1}Sr_{0.9}CuO_2$ (La-112)

In this chapter, we report findings from spatially resolved studies of the quasiparticle tunneling spectra of the infinite-layer electron-doped cuprate superconductor (SC) $La_{0.1}Sr_{0.9}CuO_2$ (La-112). We examined La-112 using scanning tunneling spectroscopy (STS) as a function of magnetic field, H, and temperature, T. We observed a spatially homogeneous tunneling spectra in zero magnetic field that exhibits only one set of superconducting peaks with no satellite features in contrast to $YBa_2Cu_3O_{7-\delta}$(Y-123). With the application of magnetic fields we observed spatially resolved vortices. The inside vortex spectra revealed a hidden pseudogap (PG) with energy V_{CO}= 8.5 meV, which is smaller than the superconducting gap, in contrast to the findings of a PG larger than the superconducting gap in Y-123 [13]. The intra-vortex PG features in finite magnetic fields together with Green function analysis of the zero-field tunneling spectra are supportive of the scenario of coexisting competing orders (CO) and superconductivity in the electron-type cuprate superconductors. Additionally, comparison of STS with ARPES and inelastic neutron scattering data further suggest that the CO is likely commensurate spin density waves (SDW) with an energy gap smaller than the superconducting gap, which is in

contrast to the incommensurate charge density waves (CDW) found in hole-type cuprates [26–30].

.

3.1 Introduction

Since the discovery of high-temperature superconducting cuprates in 1986 [1] intense theoretical and experimental research efforts have been made to unravel the elusive pairing mechanism for high-T_C superconductivity. Superconductivity in the cuprates arises from doping antiferromagnetic (AFM) Mott insulators with electrons or holes. The doped compounds become superconducting only over a range of doping concentrations, whether doped with holes or electrons. In fact, various ground-state phases besides superconductivity may emerge from doping the AFM Mott insulators [2]. Consequently, the ground state of cuprates may consist of coexisting competing orders and superconductivity. A schematic illustration of the doping vs. temperature phase diagram is shown in Figure 3.1. A common feature of the cuprates is the presence of CuO_2 planes, where holes or electrons are doped into these planes and are responsible for superconductivity. There are many unconventional phenomena exhibited by the cuprates. Two of the most widely discussed phenomenon in hole type cuprates are the pseudogap [12, 24] and Fermi arcs [12, 22–24] above the superconducting transition of the underdoped and optimally doped samples. In contrast, both features are absent in the electron-type cuprates. Several models, including the one and two-gap models, have been proposed to explain many of the unconventional phenomena observed.

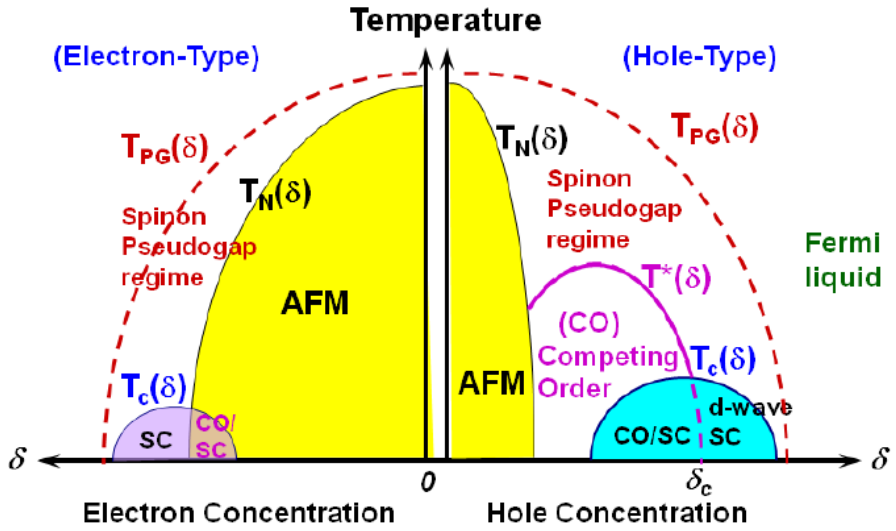

Figure 3.1: A zero-field temperature (T) versus doping level (δ) phase diagram for electron and hole-type cuprates [44]. AFM: antiferromagnetism, CO: competing order, SC: superconductivity, δ: doping level, T_N: Néel temperature, T_C: superconducting transition temperature, T*: low-energy pseudogap (PG) temperature, T_{PG}: high-energy pseudogap temperature

The one gap model is associated with the "preformed pair" conjecture that asserts strong phase fluctuations in the cuprates so that formation of Cooper pairs may occur at a temperature well above the superconducting transition [81]. The two-gap model considers coexistence of COs and SC with different energy scales in the ground state of the cuprates [6]. Recently there appears to be a consensus that the two-gap model can consistently account for most experimental phenomena [6]. However, the occurrence of COs does not exclude the possibility of preformed Cooper pairs [20].

To examine the two-gap model, we begin with the mean-field Hamiltonian

$$H_{MF} = H_{SC} + H_{CO} \qquad 3.1$$

that consists of coexisting SC and a CO at T = 0 K [12–17, 22, 82]. We also assume that the SC gap Δ_{SC} vanishes at T_C and that the CO order parameter vanishes at T^* and that both T_C and T^* are 2nd-order phase transitions [44]. The SC Hamiltonian is given by

$$H_{SC} = \sum_{\boldsymbol{k},\alpha} \xi_{\boldsymbol{k}}\, c^{\dagger}_{\boldsymbol{k},\alpha} c_{\boldsymbol{k},\boldsymbol{\alpha}} - \sum_{\boldsymbol{k}} \Delta_{\boldsymbol{SC}}(\boldsymbol{k}) \left(c^{\dagger}_{\boldsymbol{k},\uparrow} c^{\dagger}_{-\boldsymbol{k},\downarrow} + c_{-\boldsymbol{k},\downarrow} c_{\boldsymbol{k},\uparrow} \right) \qquad 3.2$$

where $\Delta_{\boldsymbol{SC}}(\boldsymbol{k}) = \Delta_{\boldsymbol{SC}}(cosk_x - cosk_y)/2$ for $d_{x^2-y^2}$ –wave pairing, **k** denotes the quasiparticle momentum, $\xi_{\boldsymbol{k}}$ is the normal-state eigen energy relative to the Fermi energy, $c^{\dagger}$ and c are the creation and annihilation operators, and α =↑,↓ refers to the spin states. The CO Hamiltonian is specified by the energy V_{CO}, a wave vector **Q**, and a momentum distribution δ**Q** that depends on a form factor, the correlation length of the CO and also on the degree of disorder [44]. While there are many possible CO's we will consider two possibilities relevant to Y-123 and La-112. If charge density waves (CDW) is the relevant CO, the incommensurate wave vector $\mathbf{Q}_1$ is found to be parallel to the CuO_2 bonding direction (π,0) or (0,π) and nested to the Fermi surface so that the CO Hamiltonian is

$$H_{CDW} = -\sum_{\boldsymbol{k},\alpha} V_{CDW}(\boldsymbol{k}) \left(c^{\dagger}_{\boldsymbol{k},\alpha} c_{\boldsymbol{k}+\boldsymbol{Q_1},\boldsymbol{\alpha}} + c^{\dagger}_{\boldsymbol{k}+\boldsymbol{Q_1},\alpha} c_{\boldsymbol{k},\boldsymbol{\alpha}} \right). \qquad 3.3$$

For Y-123, the relevant CO is CDW. If the relevant CO is a commensurate SDW (as we will see is the case for electron-type La-112), the SDW wavevector becomes $\mathbf{Q_2}$= (π,π) and the CO Hamiltonian becomes

$$H_{SDW} = -\sum_{\boldsymbol{k},\alpha} V_{SDW}(\boldsymbol{k}) \left(c^{\dagger}_{\boldsymbol{k}+\boldsymbol{Q_2},\alpha} \sigma^3_{\alpha\beta} c_{\boldsymbol{k},\beta} + c^{\dagger}_{\boldsymbol{k},\alpha} \sigma^3_{\alpha\beta} c_{\boldsymbol{k}+\boldsymbol{Q_2},\boldsymbol{\beta}} \right) \qquad 3.4$$

where $\sigma^3_{\alpha\beta}$ denotes the matrix element αβ of the Pauli matrix σ^3. If we incorporate realistic band structures and Fermi energies for different families of cuprates with a given doping and by specifying the SC pairing symmetry and the form factor for the CO, the H_{MF} can be diagonalized to obtain the bare Green function $G_0(\mathbf{k},\omega)$ for momentum **k** and energy ω

[44]. We can also include quantum phase fluctuations between the CO and SC by solving the Dyson's equation selfconsistently for the full Green function G(**k,**ω). Using the Green function we can find the quasiparticle spectral density function *A*(**k,**ω)

$$A(\mathbf{k},\omega) = \frac{-\mathrm{Im}\,\{G(\mathbf{k},\omega)\}}{\pi}. \qquad 3.5$$

From there we can calculate the density of states *N(ω)*

$$N(\omega) = \sum_{\boldsymbol{k}} A(\boldsymbol{k},\omega). \qquad 3.6$$

Based on the above Green function analysis for a specific CO, the zero-field quasiparticle spectra *N(ω)* at T = 0 K can be fully determined. For finite temperatures, the temperature Green function is employed to account for the thermal distributions of quasiparticles. Using this analysis we can accurately fit temperature-dependent quasiparticle tunneling spectra in La-112 using $d_{x^2-y^2}$ wave SC with commensurate SDW. Moreover, the commensurate SDW with an energy gap smaller than the SC gap can account for the non-monotonic momentum dependent energy gap observed by ARPES in the pairing state [22].

We should note that for this analysis if $V_{CO} > \Delta_{SC}$, such as in the case of under- and optimally doped hole-type cuprates, then we will observe sharp SC coherence peaks at $\omega=\Delta_{SC}$ and satellite features at $\omega= \Delta e_{ff}$ (where $\Delta e_{ff} =(V_{CO}^{\ 2} + \Delta_{SC}^{\ 2})^{(1/2)}$ is an effective excitation gap for $T < T_C$). This also explains the appearance of a PG for temperatures $T_C < T < T^*$. This is consistent with reports for the hole-type cuprates Y-123 and $Bi_2Sr_2CaCu_2O_{(8+x)}$ (Bi-2212). In contrast, if $V_{CO} < \Delta_{SC}$ then we will observe single set of features at Δe_{ff} and no PG above T_C as is the case in the electron type cuprates.

The above analysis provides an interesting possibility. If in a magnetic field we suppress SC in the vortex state, we should observe a PG-like feature in the tunneling

spectra instead of bound states, as is the case for a conventional superconductor [95]. As is the case with the hole-type cuprates where a PG is observed inside the vortex [12–13], we would expect a PG inside the vortex state of La-112 [82]. Therefore the tunneling spectra in the vortex state can provide direct information about the appropriate CO while SC is suppressed.

3.2 $La_{0.1}Sr_{0.9}CuO_2$ Sample Preparation and Considerations

The infinite layer cuprates, $Ln_xSr_{1-x}CuO_2$ (Ln= La, Gd, Sm) have the simplest structure of the cuprate superconductors. The unit cell of La-112 is nearly cubic, with the a-b plane and c-axis lattice constants being 0.395 nm and 0.341 nm, respectively. The superconducting coherence length in the CuO_2 plane is $\xi_{ab} \sim 4.86$ nm and along c-axis is $\xi_c \sim 0.52$ nm, which is longer than the c-axis lattice constant [83]. Various bulk properties such as the anisotropic upper critical fields and irreversibility fields of this system have been characterized previously [84].

The crystalline lattice is outlined in Figure 3.2. The samples used in this thesis were prepared by Professor Sung-Ik Lee using a high-temperature (950 °C) and high-pressure (4 GPa) process outlined in reference [85]. The high-density granular $La_{0.1}Sr_{0.9}CuO_2$ samples were single phase, as measured by x-ray diffraction (XRD) measurements [86]. Scanning electron microscopy (SEM) and x-ray photoemission spectroscopy (XPS) both observed random grain orientations and typical grain sizes on the order of a few microns [85, 86]. Magnetization measurements showed nearly 100% superconducting volume for the

samples, with T_C = 43 K. The system was also homogeneous in stoichiometry based on XPS measurements [86].

$La_{0.1}Sr_{0.9}CuO_2$ crystals are highly 3-dimensional in nature and cannot easily or cleanly be cleaved in contrast to Bi-2212. Therefore, the surface of the $La_{0.1}Sr_{0.9}CuO_2$

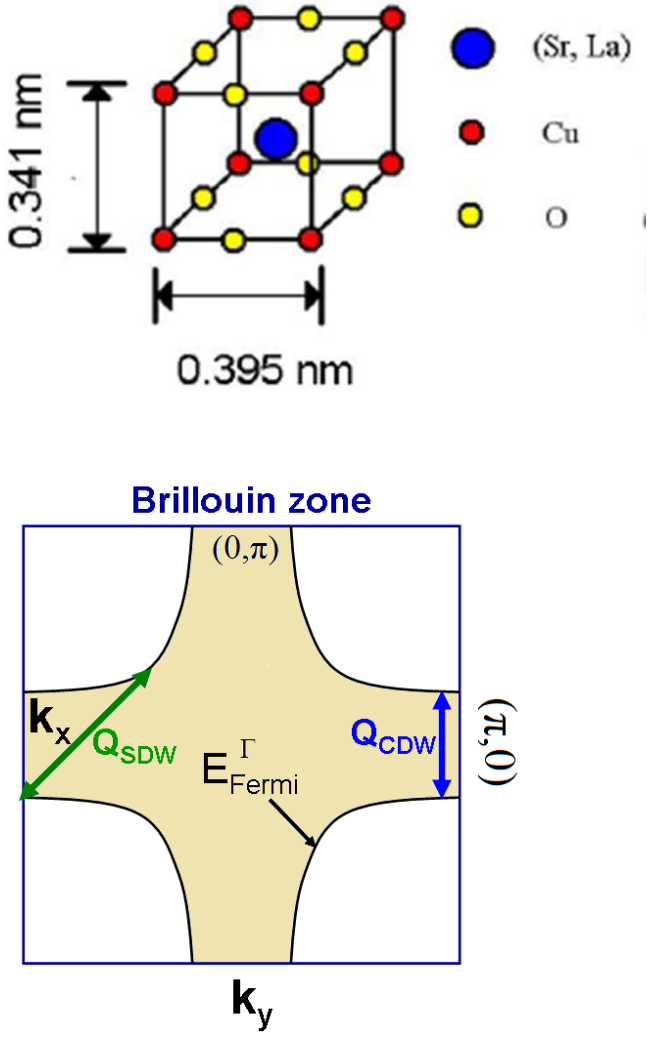

Figure 3.2 : (top panel)The crystalline structure of the infinite layer La-112. (bottom panel) The Brillouin zone of La-112 showing possible SDW and CDW **Q** wave vectors.

polycrystalline sample was prepared by chemical etching with 0.5–2% bromine in dry ethanol for 30 seconds to 4 minutes. The sample was then rinsed in pure ethanol to remove any bromides and was then dried by blowing cold-trap filtered helium gas onto the sample. According to [86], bromine etching reveals a nearly stoichiometric surface as seen by x-ray photoemission spectroscopy (XPS). Unfortunately the etched surface of La-122 does not permit sufficient topographic sensitivity to allow for imaging of individual atoms or imaging the crystalline lattice in topography scans. However, we can still measure tunneling spectra and the etched surface topography with atomic-level resolution. As noted in [87] this is due to the etched sample surface and the nature of the wave functions of the surface of La-112. After the sample surface was prepared, the sample was quickly transferred to the STM, which was brought to a pressure of $< 10^{-9}$ torr and a temperature T = 6 K. At which point STS studies were performed at several magnetic field strengths, H = 0, 1, 1.5, 2, 3.5, 4.5, and 6 Tesla.

3.3 Zero-Field Studies

In this section we present STS studies on La-112 in zero magnetic field. Multiple zero-field scans were performed over 64×64 nm^2 regions and the quasiparticle tunneling spectra was found to be homogenous throughout the sample (Figure 3.3 (b)). This finding is in stark contrast to the nanoscale spectral variations in optimal and underdoped Bi- 2212 [88]. In all tunneling spectra we can identify two superconducting coherence peaks and define a peak-peak separation distance : $2\Delta_{pk\text{-}pk}$. Figure 3.3(a) presents a representative quasiparticle spectrum with the data in black circles, and a $\Delta_{pk\text{-}pk}$ gap map over a

representative region, with the corresponding histogram of gap values. We can perform a Lorentzian fit of the histogram of $\Delta_{pk\text{-}pk}$ values, where we find a average $\Delta_{pk\text{-}pk}$ = 12.2 meV with a Lorentzian line width of 0.8 meV.

In Figure 3.3(a), the representative tunneling spectrum is normalized to a high energy background according to the methods described in [89]. Three different theoretical fitting curves are also plotted in the image with the inset showing a zoom-in comparison of the data and the three theoretical fittings. The fitting curves that assume pure s-wave SC (green), pure $d_{x^2-y^2}$-wave SC (red) are not as effective in fitting the data as coexisting $d_{x^2-y^2}$-wave SC with commensurate SDW (blue). We therefore tentatively identify $\Delta_{pk\text{-}pk}$ as Δ_{eff} following our previous arguments in Section 3.1. We should note that in contrast to STS studies on Y-123 we do not observe any satellite features in the quasiparticle tunneling spectra of La-112.

Investigations of the temperature dependence of the $\Delta_{pk\text{-}pk}$ reveal the gap shrinking with increasing temperature and finally closing at T = 43 K. Above T_C the tunneling spectra shows a purely metallic-like LDOS with no evidence of a pseudogap feature as is found in the hole-type cuprates. This is consistent with the absence of a pseudogap at $T_C < T < T_{PG}$ for all other electron doped cuprates. The temperature evolution of the effective gap is illustrated Figure 3.4, with the inset showing the temperature dependence of Δ_{eff} which appears to follow a BCS-like behavior.

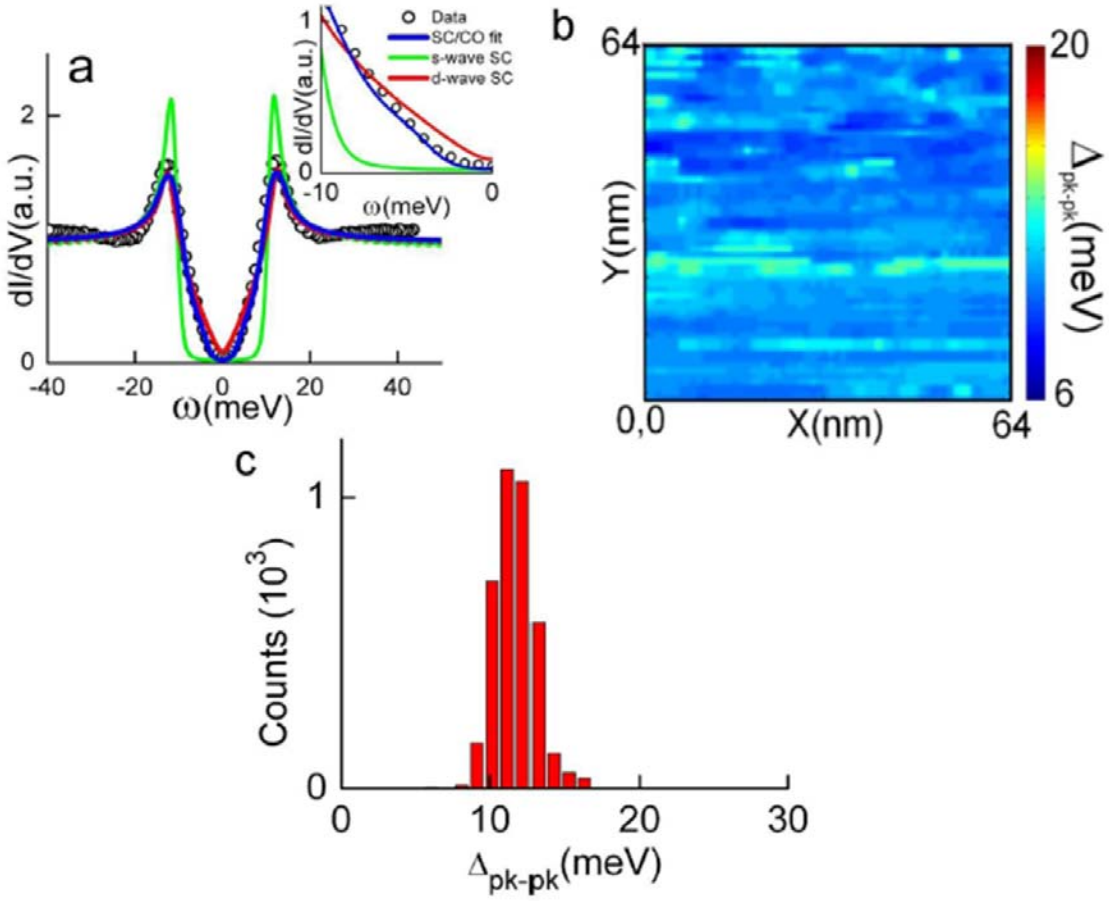

Figure 3.3: (a) A representative normalized dI/dV spectrum (open circles) fort H = 0 and T = 6K with attempts to fit the data using BCS superconductivity alone as solid-lines for pure s-wave (green) and pure d-wave (red) pairing symmetry and using a model of coexisting superconductivity and a competing order as another solid-line (blue) on top of the data. The attempts to fit the data all use Δ_{SC} = 12.0meV. The competing order model assumes a gapped spin-density wave for the competing order and uses values of $V_{CO} = V_{PG}$ = 8.0 meV and density-wave vector Q=(π,π) to generate the fit. Neither fitting that assumes pure superconductivity can sufficiently account for the gapped spectra and the subgap states, while the fitting of SC and a gapped SDW more closely models the data. Inset: A closer view of the subgap quasiparticle tunneling spectra that better shows the inability of d-wave and s-wave BCS spectra to fit the data, while the SC/CO fitt better accounts for the subgap states. We further note that the incorporation of SC and commensurate SDW in electron-type cuprates is consistent with inelastic neutron scattering experiments [93] and is also essential to account for the nonmonotonic momentum-dependent energy gap found in ARPES studies [22]. (b) A map of Δ_{pk-pk} values over a 64 nm × 64 nm area. (c) A histogram of Δ_{pk-pk} values from (b)

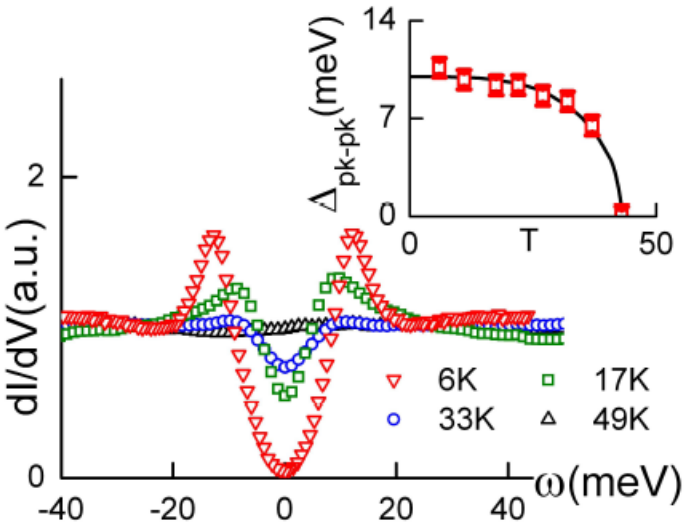

Figure 3.4: Representative tunneling spectra as a function of temperature in zero magnetic field for T = 6, 17, 33 and 49 K. No PG feature is observed above T_C. Inset: Δ_{pk-pk} vs. temperature showing a BCS-like dependence

3.4 Magnetic Field Studies

In this section we present spatially resolved STS as a function of magnetic field at low temperatures. In order to investigate the vortex state, all measurements were performed below the c-axis irreversibility field of H = 10 Tesla at T = 0 K as determined in [84]. The size of vortex cores for superconductors is determined by the relevant coherence lengths and in anisotropic superconductors, such as the cuprates, depends on the crystalline plane examined. For tunneling currents parallel to the c-axis, or {001} surface, vortices will be circular in shape and have a core radius given by the a-b plane coherence length, ξ_{ab}. We note that the observed vortices in these studies had radii comparable to ξ_{ab}; so we conclude that the vortex-state spectroscopic studies were performed by tunneling along the c-axis and also with applied magnetic fields parallel to the c-axis.

Upon applying magnetic fields H with the condition $0 < H < H_{c2}^{ab,c}$, the quasiparticle tunneling spectra exhibit strong spatial inhomogeneity, as exemplified in Figure 3.5 (b) for H = 1.5 Tesla over a 152 × 160 nm^2 area. We have plotted the square of the conductance power ratio

$$\frac{(dI/dV|_{\omega=\Delta\text{eff}})^2}{(dI/dV|_{\omega=0})^2} \qquad 3.7$$

in order to accentuate the presence of vortices. This follows the supposition in Section 3.1 that the coexistence of CO with $\Delta_{CO} < \Delta_{SC}$ would result in intra-vortex pseudogap. However, since SC is suppressed inside the vortex core and spectral weight must be conserved, we expect a decrease in intra-vortex spectra weight in the tunneling conductance at $\omega = \Delta_{eff}$ and an increase in spectra weight at $\omega = 0$ meV. Consequently plotting conductance power ratio will enhance the presence of vortices in the image where we can find that the presence of vortices is associated with the local minimum of the conductance power ratio. In comparison to the H= 1.5 Tesla plots, the conductance power ratio plots of the same region at H = 0 Tesla are very homogenous as exemplified in Figure 3.5(a). Contrasting the two allows us to identify presence of 18–19 highly disordered vortices, which is in agreement with expected number of vortices for an Abrikosov vortex lattice in a 152 × 160 nm^2 area. We also note that the average radius of the vortices is comparable to the superconducting coherence length, ξ_{ab}.

Given that we are primarily interested in achieving high spatial resolution in order to investigate the inter- to intravortex spectral evolution, we next focus on smaller spatial maps in finite fields. As shown in Figure 3.6 (a,b) we have plotted conductance power ratio

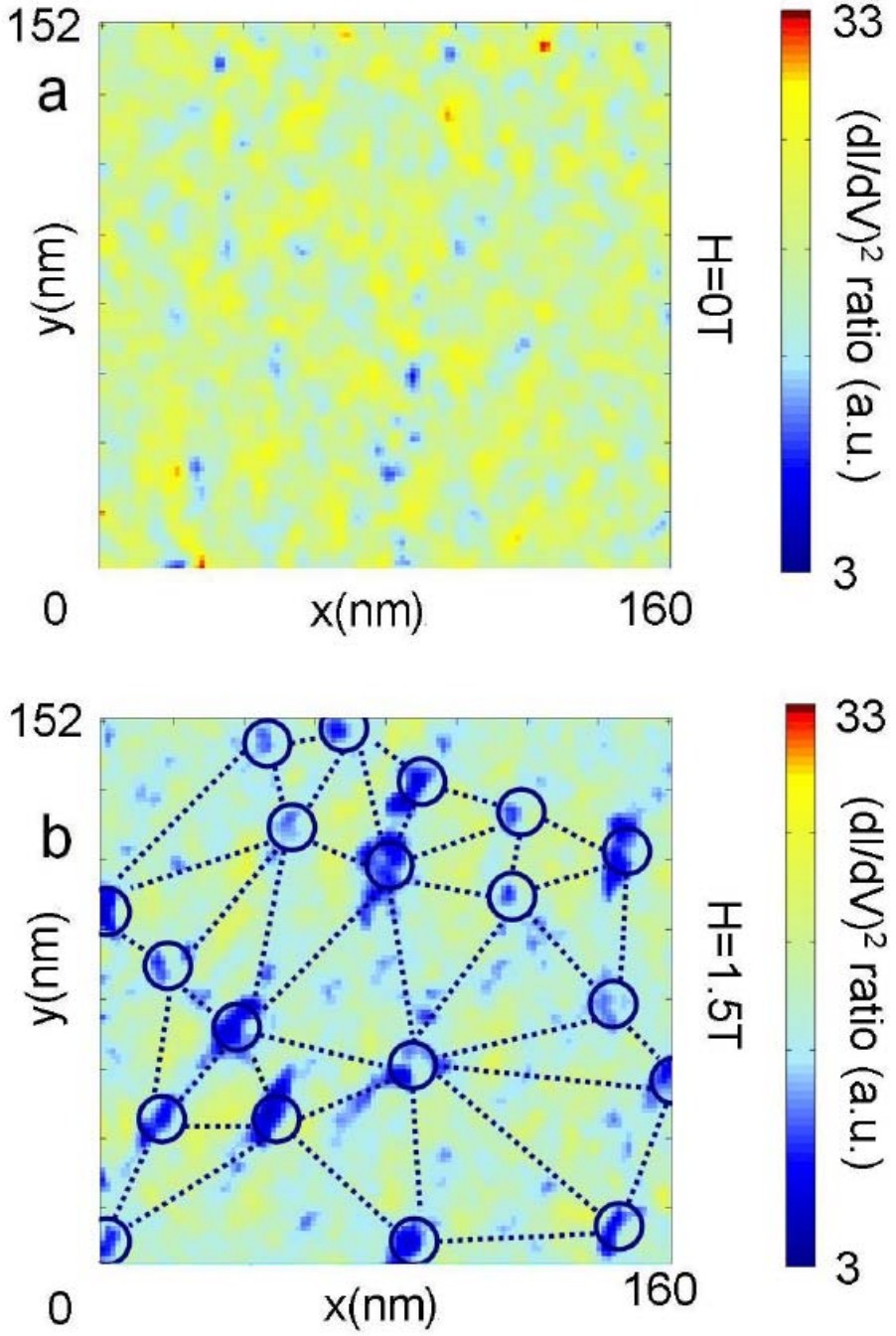

Figure 3.5 (a) Conductance ratio map of a 152 nm × 160 nm region at H = 0 Tesla showing nearly uniform conductance. (b) Conductance ratio map of same region in (a) at H = 1.5 Tesla revealing the presence of 18 vortices. The vortices are revealed as minimum in the conductance ratio.

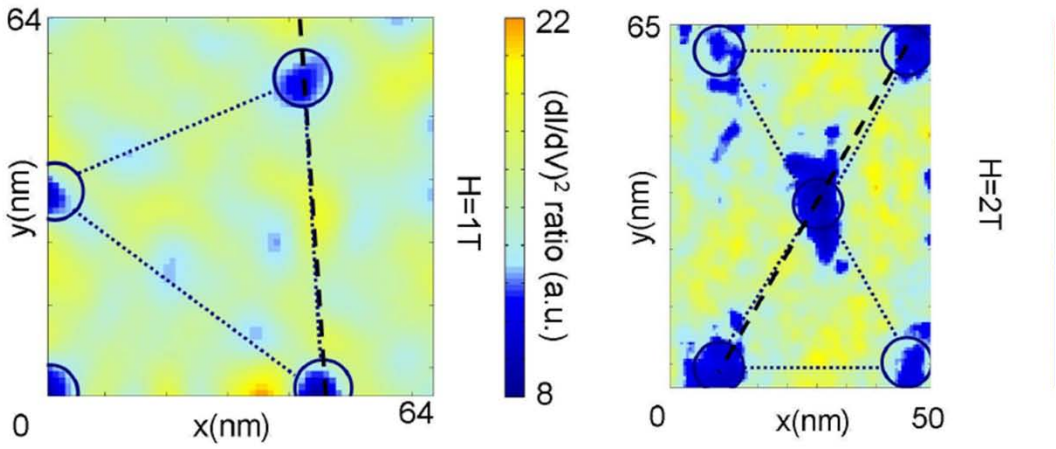

Figure 3.6: Conductance ratio maps for (a) H = 1 Tesla for a 64 nm × 64 nm region with 3 visible vortices. (b) H = 2 Tesla for a 65 nm × 50 nm region with 5 visible vortices

maps for H = 1 Tesla (64×64 nm^2) and H = 2 Tesla (65×50 nm^2) For the smaller maps, vortices are still clearly visible at both H = 1 and 2 Tesla with averaged vortex lattice constants a_B = 52 nm and 35 nm, respectively, which are comparable to the theoretical values given by $a_B = 1.075(\Phi_0/B)^{1/2}$. However, the shape of vortices observed in the experiments is generally irregular. Possible causes for the irregular vortex shape may be due to microscopic disorder in the sample, surface roughness after chemical etching, or possible interaction between the STM tip and the vortices.

We note that all spectra observed for Figure 3.6(a,b) are gapped and that there are no zero-bias conduction peaks anywhere in either map, even in the vortex cores. The presence of PG-like features inside the vortex is similar to the findings in hole-type Bi2212 and Y-123 [7, 91, 92].

To better illustrate the spatial evolution of the tunneling spectra, we present spatial linecuts through two vortices at H = 1 Tesla and through 3 vortices at H = 2 Tesla for the conductance maps in Figure 3.6 and are indicated by black dashed lines. These linecuts are shown in Figure 3.7.

We find that the value of $\Delta_{pk\text{-}pk}$ is lower inside vortices than $\Delta_{pk\text{-}pk}$ for outside the

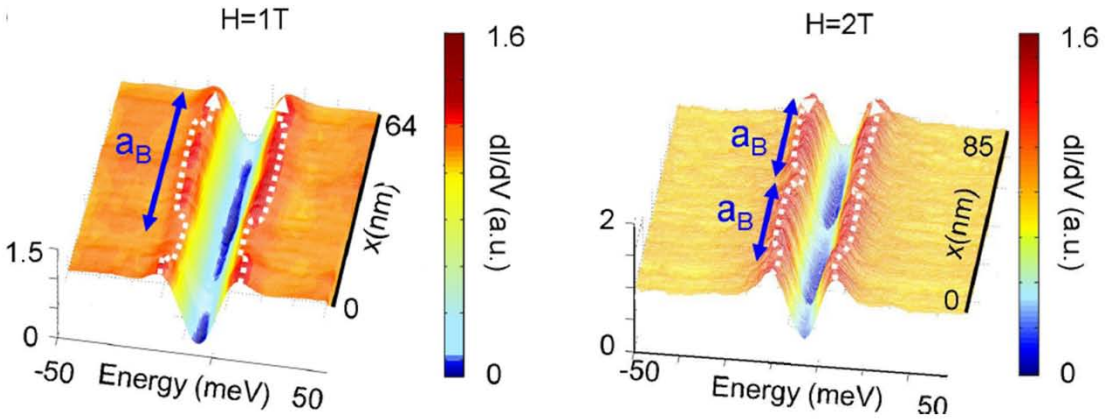

Figure 3.7 : Linear linecuts of tunneling spectra along the black dashed lines in Figure 3.6 (a) Vortex linecut in H= 1 Tesla. (b) Vortex linecut in H=2 Tesla. We find modulations in the zero-bias conductance (ω= 0) and slight modulations in the peak-to-peak energy gap ($\Delta pk_{\text{-}pk}$). The modulations track the periodicity of a_B. The zero-bias conductance is maximum inside vortices, while the ω= $\Delta_{pk\text{-}pk}$ conductance is a minimum inside vortices.

vortices. The value of $\Delta_{pk\text{-}pk}$ is ~ 8.5 meV (which we identify as V_{CO}) inside vortex cores for both H = 1 and 2 Tesla, while the average, outside vortex core $\Delta_{pk\text{-}pk}$ equals 11 meV for H = 1T and 10.5 meV for H = 2T. The spatial linecuts at H = 1 T and H = 2 T also reveal modulations induced in the quasiparticle spectra by the vortices. Specifically, we note modulations in the zero-bias conductance as it increases inside the vortices and modulations at $\Delta_{pk\text{-}pk}$ which decreases inside the vortices. The modulations track the periodicity of a_B, as expected. The pseudo-gap energy inside the vortices is smaller than

the Δ_{eff} as measured at H = 0 Tesla. Upon increasing magnetic field, the energy associated with the peak features at $\Delta_{pk\text{-}pk}$ outside vortices decreases slightly and the line width of the peaks broadens, whereas the PG-energy at V_{CO} inside vortices remains constant, as shown in Figure 3.8(a–d) for comparison of representative inter- and intra-vortex spectra taken at *H* = 1, 2, 3.5, and 6 T. For magnetic fields H > 2 Tesla, the contrast

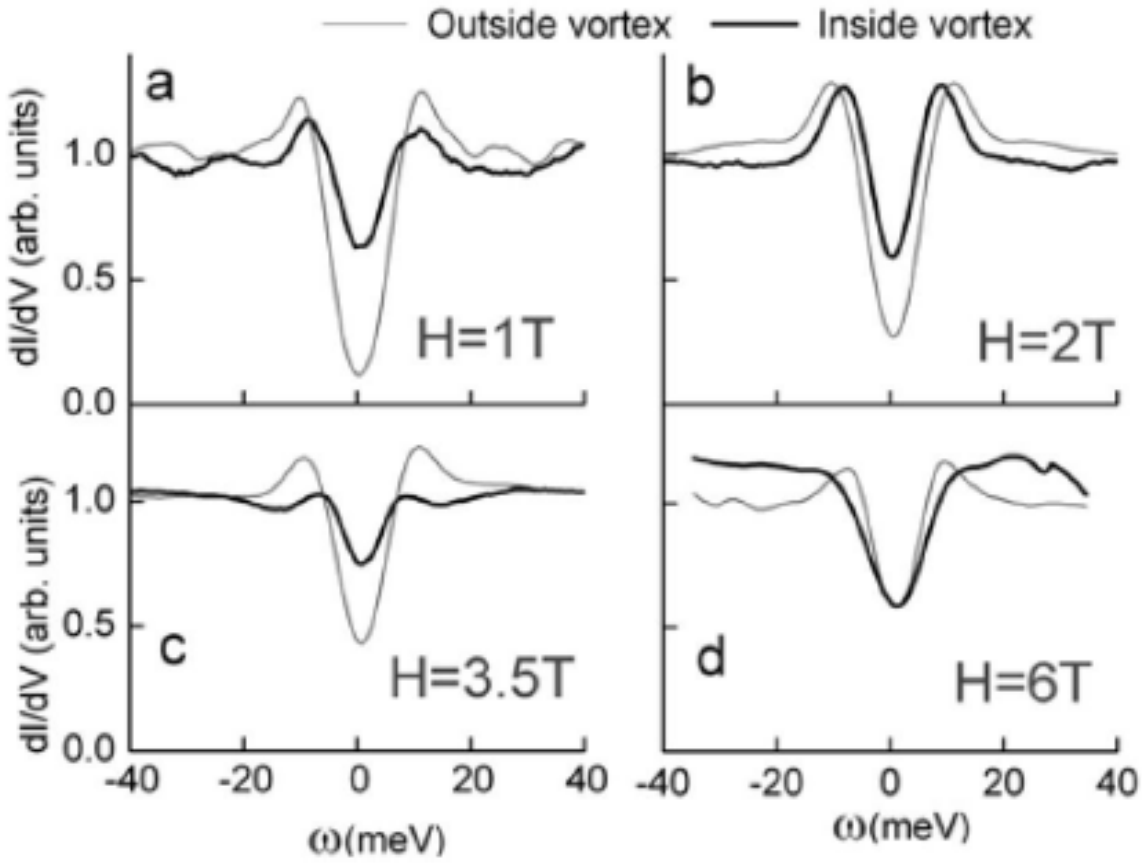

Figure 3.8: Comparison of inter- and intra-vortex spectra for several magnetic fields. (a) H = 1 Tesla. (b) H = 2 Tesla. (c) H = 3.5 Tesla. (d) H = 6 Tesla. We find pseudogap-like spectra in the vortex cores, shown as thick lines. Spectra well outside of vortices are shown as thin lines. The peak features around $\omega = \Delta_{pk\text{-}pk}$ broaden as H increases. The zero-bias conductance of the spectra outside vortices increases with H.

between inter- and intra-vortex spectra begins to diminish, making identification of vortices difficult.

To better understand the tunneling spectra evolution with increasing fields, we plot histograms of $\Delta_{pk\text{-}pk}$ as a function of magnetic field for H = 0, 1, 2, 3, 3.5, 4.5, and 6 Tesla. The histograms were generated from all spectra taken over spatial maps varying in size from 50 × 50 nm^2 to 100 × 100 nm^2. We find that each histogram can be fit by a Lorentzian and we associated the peak energy with Δ_{eff} which decreases slightly with increasing magnetic field. The vast majority of the observed $\Delta_{pk\text{-}pk}$ values appeared above an apparent low-energy "cutoff" at V_{CO} = 8.5 ± 0.6 meV for all histograms, as illustrated by the pale blue wall in Figure 3.9(a). This behavior is in contrast to the histograms expected for a conventional type-II superconductor with no CO as shown in Figure 3.9(b). In this situation we would expect as H increases, the quasiparticles in the vortex state of a conventional type-II superconductor shift to lower energy and a peak at ω= 0 appears. The downshifted spectral weight is approximated by the ratio of the vortex core area relative to the Abrikosov vortex unit cell, $\left(\pi {\xi_{ab}}^2/2\right)/\left(\sqrt{3}a_B^2/4\right)$. This is shown in Figure 3.9(c).

3.5 Discussion

To understand the absence of zero bias conductance peaks in the vortex-state quasiparticle spectra, the pseudogap-like behavior inside the vortex core, and the existence of a low-energy cutoff at V_{CO} requires the scenario of coexisting CO and SC and cannot be explained by the scenario of pure SC in the ground state. In Figure 3.3 we plotted a representative tunneling spectra for H = 0 Tesla with three different fittings. The fittings

assumed pure *s*-wave SC (green), pure $d_{x^2-y^2}$-wave SC (red), and coexisting $d_{x^2-y^2}$-wave SC and commensurate SDW(blue) with the following fitting parameters: SC gap Δ_{SC} = 12.0 ± 0.2 meV, CO energy V_{CO} = 8.0 ± 0.2 meV, and CO wave vector **Q** = (π, π) for the SDW. We note that the consideration of commensurate SDW [93] as the relevant CO is consistent with neutron scattering data from electron-type cuprate superconductors [94].

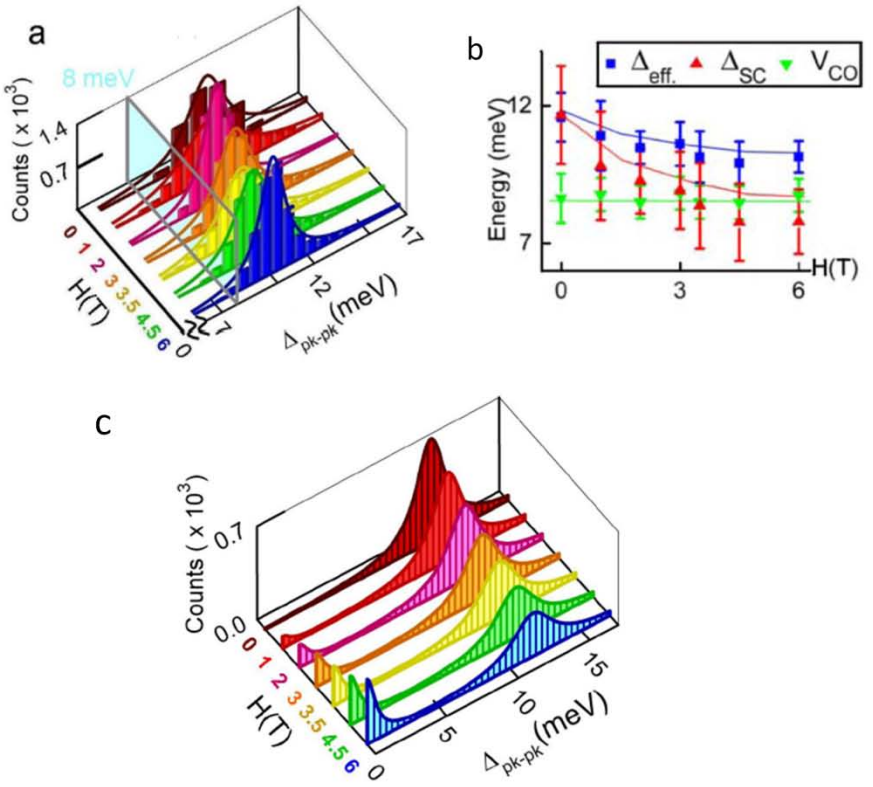

Figure 3.9 : Histograms of the $\Delta_{pk\text{-}pk}$. (a) Histograms $\Delta_{pk\text{-}pk}$ determined from quasiparticle tunneling spectra reveal the spectral evolution for H > 0. The value of $\Delta_{pk\text{-}pk}$ decreases as we increase field, but never seems to drop below $\Delta_{pk\text{-}pk}$ = 8:5±0.6 meV, the low-energy cutoff. Each histogram is fit by a Lorentzian form, shown as solid lines on top of the histograms. (b) Δ_{eff} , Δ_{SC} , V_{CO} vs. H obtained from Lorentzian fits and Green function analysis of tunneling spectra. As H increases V_{CO} remains constant while Δ_{SC} and Δ_{eff} decrease in size. (c) Predicted $\Delta_{pk\text{-}pk}$ vs. H for a conventional BCS superconductor

The analysis suggests the best fit for zero-field spectra is the scenario of CO with SC. Moreover, ARPES studies of the energy gap in electron-type cuprates revealed non-monotonic momentum dependence [96], which can only be explained by considering coexisting SC and commensurate SDW, as discussed in [22] and reproduced below in Figure 3.10.

Interestingly, the CO energy derived from the zero-field analysis, $V_{CO} = 8.0 \pm 0.2$ meV, is consistent with the PG energy observed inside the vortex core, implying that the intra-vortex PG has the same physical origin as the zero-field CO. Additionally, the CO scenario can account for the temperature dependence of the zero-field tunneling spectra, as shown in the main panel of Fig. 3.4, where the theoretical fits(not shown) to the experimental data are obtained by using the temperature Green's function and temperature-dependent Δ_{SC} and V_{CO} values that yield the correct empirical $\Delta_{eff}(T)$. This finding suggests that the commensurate SDW coexists with SC for La-112. Although it is generally not conclusive to determine the CO wave-vector from Green function fitting to the tunneling spectra that only contains integrated momentum information, the successful account of the momentum-dependent energy gap determined by ARPES (see Figure 3.10) consistently corroborates with our STS studies and provides strong support for the scenario of coexisting superconductivity and commensurate SDW in electron-type cuprates [22].

We can compare these results with studies [13] on the hole-type Y-123 which also revealed PG-like features and field-induced modulations inside the vortices. In those studies, however, the PG energy is larger than Δ_{SC}. The larger energy associated with the PG-like features inside vortices of Y-123 is consistent with the presence of a zero-field PG

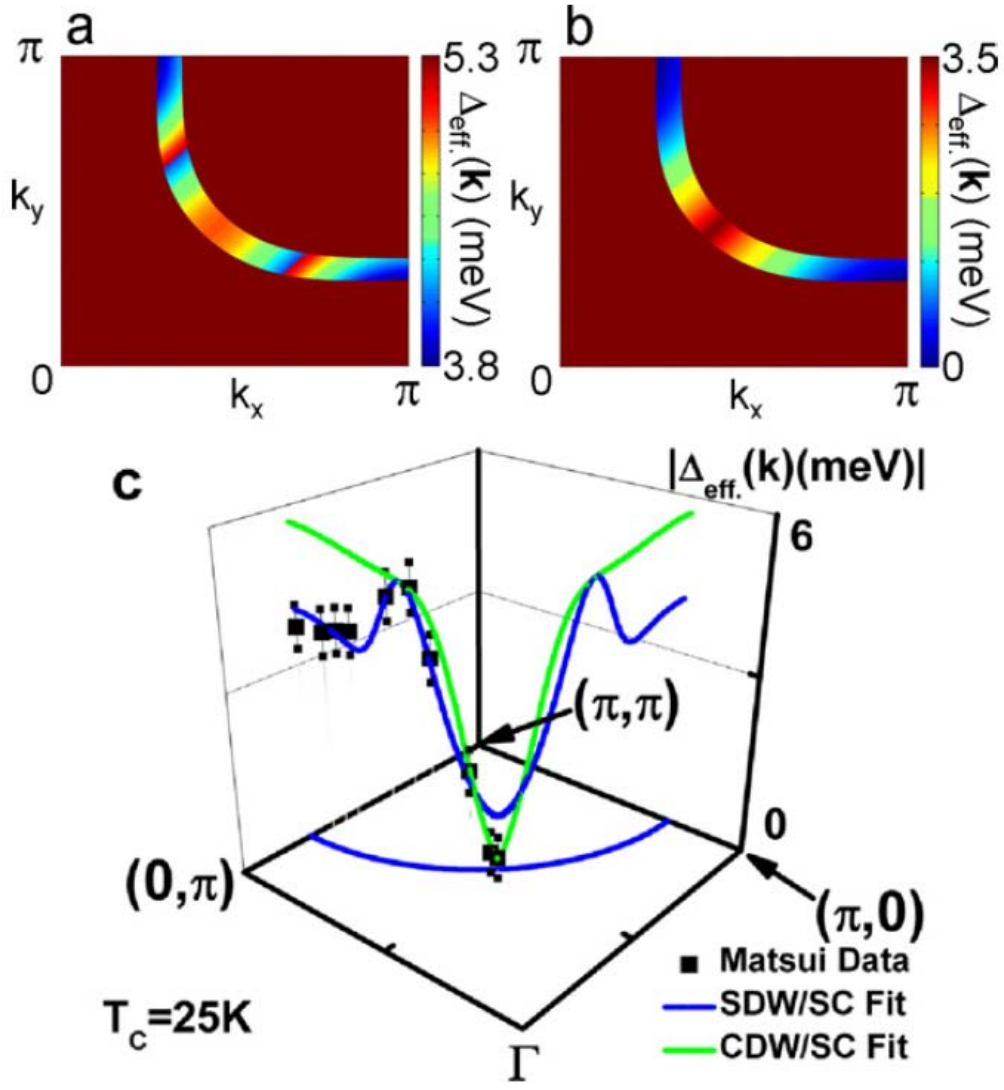

Figure 3.10: Simulations of $\Delta_{eff}(\mathbf{k})$ in the first quadrant of the Brillioun zone of the electron-type cuprate $Pr_{0.89}$ $LaCe_{0.11}CuO_4$ at (a) T = 0 and (b) T = 0.9 T_C . (c) Momentum-dependent ARPES leading edge data from [97] together with theoretical fitting for two types of CO's, CDW and SDW. The navy line corresponds to Q =(π,π) for SDW, and the green line corresponds to Q =(π,0) or (0,π) for CDW. Clearly the fitting curve with Q =(π,π) for SDW agrees much better with ARPES data. Image from [22].

at a temperature higher than T_C. These findings from the vortex-state quasiparticle spectra of Y-123 are in contrast to those of La-112 where in the latter no zero-field PG exists above T_C and the field-induced PG energy is smaller than Δ_{SC}.

We should also note that this work is the first and remains the only observation of vortex state in the electron-type cuprates. The difficulty of observing vortices in the electron-type cuprates may be due to the smaller superconducting gap energies in the electron-type cuprates which are very close to competing order energies, V_{CO}, and so reduces the contrast between inter- and intra-vortex spectra.

In this section we have presented STS magnetic field studies of the electron type superconductor La-112. Spatially resolved quasiparticle tunneling spectroscopy revealed a hidden pseudogap inside vortices and unconventional spectral evolution with temperature and magnetic field dependence. The scenario of coexisting CO and SC provided the best explanation for experimental data of both electron- and hole-type cuprate studies.

Chapter 4

Scanning Tunneling Spectroscopic Studies of the Electron-Doped Iron Pnictide Superconductor $Ba(Fe_{1-x}Co_x)_2As_2$

Building on our experimental findings and analysis for the cuprate superconductors, specifically the electron type cuprate $La_{0.1}Sr_{0.9}CuO_2$ (La-112), we now consider for contrast and comparison the ferrous superconductor $Ba(Fe_{1-x}Co_x)_2As_2$. The recent discovery of a new class of iron-based superconductors in 2008 [98] has caused a renewed interest in both experimental and theoretical research of high-temperature superconductivity. Similar to the cuprate superconductors, the exact pairing mechanism in these ferrous superconductors is not known and therefore these superconductors provide an excellent ground for comparative studies. Scanning tunneling spectroscopic studies of temperature, doping, and magnetic field dependence were conducted on $Ba(Fe_{1-x}Co_x)_2As_2$ single crystals with doping levels x = 0.06, 0.08, 0.12 and T_C =14 , 24, 20 K respectively . In this chapter, evidence is presented for sign-changing two-gap superconductivity which is in agreement with ARPES studies and theoretical predictions. For all doping levels, both superconducting gaps decrease monotonically in size with increasing temperature and disappear for temperatures above the superconducting transition temperature, T_C. Magnetic resonant modes that follow the temperature dependence of the superconducting gaps are also identified in the tunneling

quasiparticle spectra. Together with quasiparticle interference (QPI) analysis and magnetic field studies—our findings provide strong evidence for two-gap, sign-changing s-wave superconductivity. In the presence of a magnetic field, a pseudogap (Δ_{PG} ~ 11–12 meV) is observed inside the vortex core, which is in contrast to theoretical predictions for pure s-wave superconductivity and suggests the coexistence of a competing order with superconductivity in the ground state. Moreover, the strong presence of a QPI wave-vector that doubles the wave-vector associated with the antiferromagnetic spin-density waves (SDW)is consistent with the presence of charge density waves (CDW) induced by spin density waves (SDW). We begin with an overview of the basic physical properties of $Ba(Fe_{1-x}Co_x)_2As_2$.

4.1 Introduction

In this section the basic structural and electronic properties of the ferrous superconductors and more precisely $Ba(Fe_{1-x}Co_x)_2As_2$ are reviewed. Similar to the cuprates, the ferrous superconductors are type II unconventional superconductors and are layered materials with magnetic instabilities [44]. The basic chemical structure is FeX, where X = As, P, S, Se, Te. Structurally, FeX forms a tri-layer that consists of a square array of Fe residing between two checkerboard layers of X [44]. Similar to the cuprates where the CuO_2 layers are responsible for superconductivity, the FeX tri-layers provide the same role in the iron-based superconductors. The origin of superconductivity resides with the *d*-electrons of Fe in the FeX tri-layers, with the X-layer contributing to delocalizing the *d*-electrons [99–101]. The FeX tri-layers are separated by the layers of alkali, alkaline-earth, or rare-earth atoms and oxygen/fluorine. There are four basic types of iron-based

superconductors: the “1111”, “122”, and “111’ pnictides and the “11” type iron chalcogenides. The basic structure of the “122” iron pnictides is shown in Figure 4.1(a).

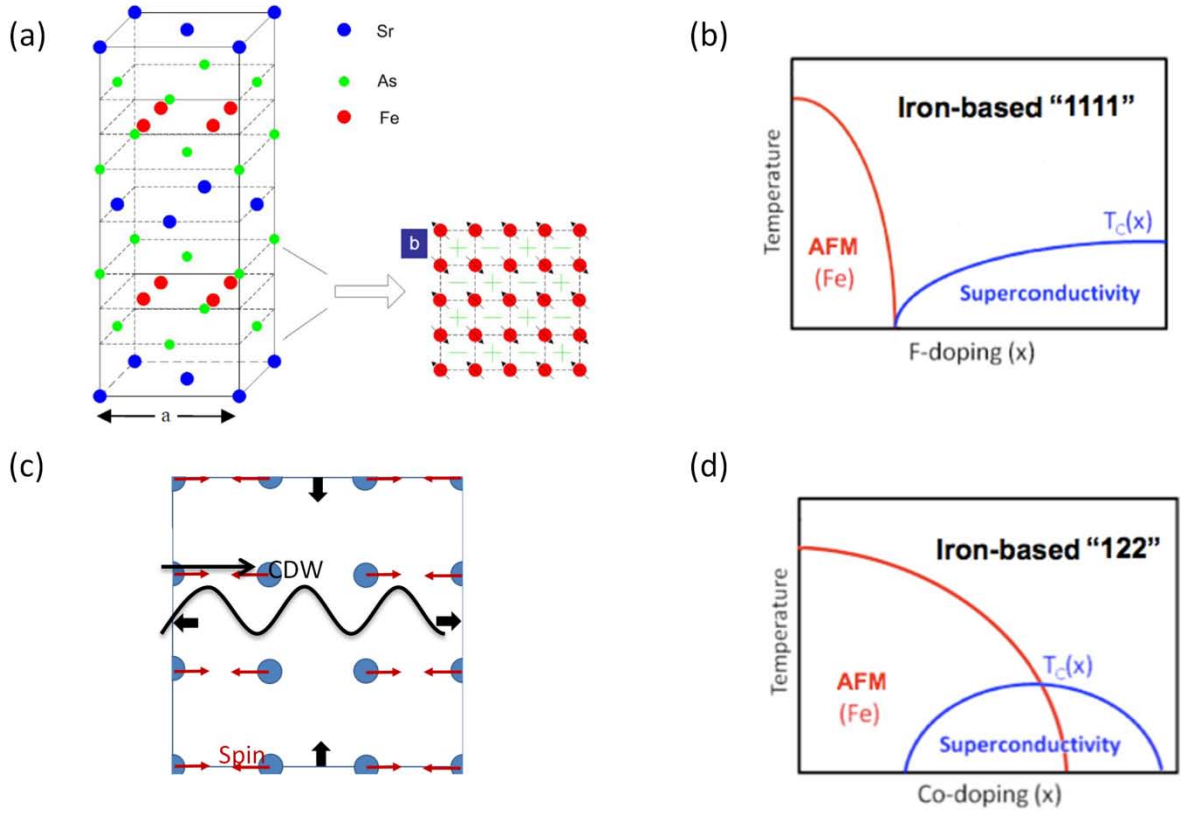

Figure 4.1: Lattice structure and doping vs. temperature phase diagrams. (a) Three-dimensional image of the “122” iron pnictides [117]. For $Ba(Fe_{1-x}Co_x)_2As_2$, Co is doped into the Fe. (b),(d) Doping vs. temperature phase diagrams for both the “1111” and the electron doped “122” systems. We observe that only in the “122” system is there an overlap of superconductivity and the AFM order. (c) Two dimensional cut of the crystal lattice along the Fe planes. The arrows show the Fe-Fe elongation in directions parallel to the direction of antiferromagnetic spin coupling and contraction in directions parallel to the ferromagnetic spin coupling, where the red arrows denote the spin configurations. This results in the occurrence of CDW modulations[44], which are observable in our STS studies.

The “122” systems have the chemical formulas $(A_{1-x}B_x)Fe_2As_2$ where A = Ba or Sr, and B = K or Cs for the hole type [102]. If Co is instead substituted in for Fe, the

substitution leads to the electron type "122", such as $Ba(Fe_{1-x}Co_x)_2As_2$ [103, 104]. The lattice constants for $Ba(Fe_{1-x}Co_x)_2As_2$ are (a,b) = 0.56 nm and c_0 = 1.239 nm above structural phase transition at T_S , below which the system transforms from a tetragonal phase to a orthorhombic structure. This phase transition will have important consequences for STS measurements. In contrast to the cuprate superconductors whose parent compound is a Mott insulator, the parent compounds of the ferrous superconductors are semimetals [44]. On the other hand, as shown by the phase diagrams in Figure 4.1(b,d) for the "122" systems, superconductivity and antiferromagnetic (AFM) phases are predicted to coexist for a range of doping levels, similar to the competing order (CO) phenomena found in the cuprates. For most of the ferrous superconductors, the parent compounds exhibit AFM at ambient pressures. This magnetic order couples with the aforementioned tetragonal to orthorhombic structural distortion. For the stoichiometric "122" system such as the $Ba(Fe_{1-x}Co_x)_2As_2$ [90], first-order structural and AFM transitions occur at the same temperature. In the low-temperature phase, the a-b plane Fe-Fe distance elongates in the direction parallel to the antiferromagnetically coupled magnetic moment and contracts in the direction perpendicular to it (Figure 4.1(c)). Consequently for the "122" systems there is a possibility of coexistence of competing orders with superconductivity. However, the exact doping level at which this coexistence occurs remains unclear. On the other hand, the situation is different for the "1111" systems where the doping-dependent phase diagrams demonstrate that superconductivity and the AFM order do not coexist[44] as shown schematically by Figure 4.1(d). The difference in the doping-dependent phase diagram has strong consequences for the vortex core states of both the "122" and "1111" systems. Following our analysis of the cuprate superconductors, the doping-dependent phase diagrams suggest

that different ferrous superconductors should exhibit different intra-vortex quasiparticle spectra, depending on if AFM coexists with superconductivity in the ground state. If CO coexists with superconductivity, we would expect to observe a pseudogap inside the vortex state for the "122" systems and bound states inside the vortex state for the "1111" systems [44].

The ferrous superconductors are believed to be approximately described by a five band model near the Fermi level according to theoretical calculations based on density functional theory [104, 106–108] and that their Fermi surfaces involve multiple disconnected pockets. The presence of multiple bands and multiple disconnected Fermi pockets suggests that inter-Fermi surface interactions are important to the occurrence of ferrous superconductivity [44]. Calculations of magnetic susceptibility have shown that these ferrous compounds should indeed have an AFM order, and the wave vectors associated with the AFM coupling coincide with those connecting the centers of the electron and hole Fermi pockets [108, 109]. These theoretical findings have led to the conjecture of two-gap superconductivity mediated by AFM spin fluctuations, with sign-changing *s*-wave order parameters for the hole and electron Fermi pockets [44]. Figure 4.2(a) shows the predicted Fermi surface of the iron-based superconductors along with the predicted AFM wave vectors. These properties of the iron-based compounds are in contrast to the cuprates with are primarily described by an effective one band model with a large Fermi surface and are one-gap superconductors described by predominately a $d_{x^2-y^2}$ pairing symmetry.

The theoretical prediction for sign changing s-wave pairing symmetry in the iron-based superconductors has been verified by inelastic neutron scattering experiments [111–114]. The inelastic neutron scattering experiments show a neutron resonance at the AFM ordering wave vector as expected theoretically below T_C for sign changing s-wave pairing. Specifically, the magnetic susceptibility in the superconducting state of a multiband superconductor is governed by the sign change of the superconducting gaps at the ‘‘hot spots’’ of the Fermi surface and the following energy conservation formula for inelastic scattering of the Bogoliubov quasiparticles on the Fermi surface [110, 116]:

$$\Omega^{vv'}\left(\vec{\boldsymbol{k}}_{\boldsymbol{F}}, \vec{\boldsymbol{q}}\right) = \left|\boldsymbol{\Delta}^{\boldsymbol{v}'}_{\vec{\boldsymbol{k}}_{\boldsymbol{F}}}\right| + \left|\boldsymbol{\Delta}^{\boldsymbol{v}}_{\vec{\boldsymbol{k}}_{\boldsymbol{F}}+\vec{\boldsymbol{q}}}\right| \tag{4.1}$$

where *v* and *v*’ represent different energy bands and the wave vectors $\vec{\boldsymbol{q}}$ are between various pieces of the Fermi surface that have opposite sign in the superconducting pairing potential $\Delta^{v}_{\vec{k}+\vec{q}}$.

The elastic scattering of quasiparticles by impurities will be dependent on whether the superconducting order parameter has opposite signs on electron and hole pockets of the Fermi surface. That is, in zero magnetic field:

$$\left|\boldsymbol{\Delta}^{\boldsymbol{v}}_{\vec{\boldsymbol{k}}_{\boldsymbol{F}}}\right| = \left|\boldsymbol{\Delta}^{\boldsymbol{v}'}_{\vec{\boldsymbol{k}}_{\boldsymbol{F}}+\vec{\boldsymbol{q}}}\right|. \tag{4.2}$$

Nonmagnetic impurities will cause strong scattering of quasiparticles between pieces of the Fermi surface that have opposite sign in the pairing potential while suppressing the scattering between pieces of the Fermi surface with the same sign in the pairing potential [44]. Conversely, magnetic impurities (or nonmagnetic impurities in the presence of a magnetic field) will cause strong scattering of quasiparticles between pieces of the Fermi

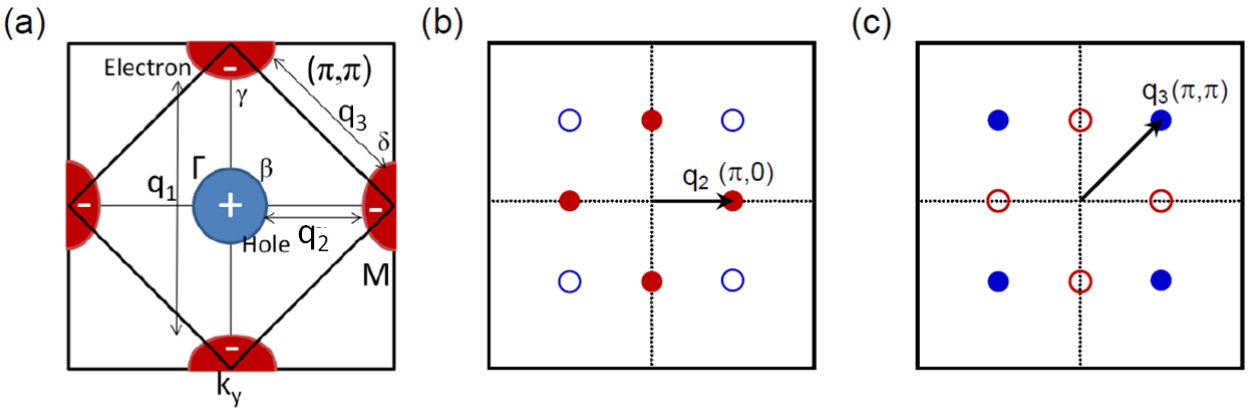

Figure 4.2: Fermi surface and expected quasiparticle wave vectors. (a) Two-dimensional cut of the Fermi surface of the ferrous superconductors in the one iron unit cell showing both electron (γ,δ) and hole (α,β) pockets. Also plotted are quasiparticle interference wave vectors connecting different parts of the Fermi surface: $\boldsymbol{q}_1, \boldsymbol{q}_2,$ and $\boldsymbol{q}_3$. (b) Theorectical prediction for quasiparticle interference intensities for scattering from nonmagnetic impurities in zero field at the superconducting gap energies. We note that $\boldsymbol{q}_2$ should be strongly apparent and $\boldsymbol{q}_3$ suppressed. If CDW waves are present then $\boldsymbol{q}_1 = \boldsymbol{2q}_2$ may appear. (c) Theoretical prediction for quasiparticle interference intensities for scattering from magnetic impurities in zero field or nonmagnetic impurities in a magnetic field at the superconducting gap energies. We note that $\boldsymbol{q}_3$ should be apparent and $\boldsymbol{q}_2$ reduced in strength.

surface with the same sign in the pairing potential and suppress scattering of quasiparticles between pieces with opposite sign. Consequently, quasiparticle interference analysis of elastic scattering in experimental tunneling data would be able to verify a sign changing s-wave pairing symmetry in the ferrous superconductors. Figure 4.2(a–c) shows the distinct wave vectors expected for quasiparticle scattering from nonmagnetic impurities in zero magnetic field and from magnetic impurities (or from nonmagnetic impurities in a nonzero magnetic field).

Tunneling spectra can also provide important information about inelastic scattering at higher tunneling energies. T. Das et al. argued that a multiband superconductor with sign

changing gaps would have multiple spin resonances [110]. These magnetic resonance modes are due to inelastic scattering of quasiparticle interferences by collective modes. The predicted magnetic susceptibility in the random phase approximation is given by

$$\tilde{\chi}_0(q,\Omega) = \frac{M^{vv'}}{N}\sum_k \left\{ \frac{1}{2}\left[1 + \frac{\varepsilon_{k+q}^{v}\varepsilon_{k}^{v'} + \Delta_{k+q}^{v}\Delta_{k}^{v'}}{E_{k+q}^{v}E_{k}^{v'}}\right]\frac{\mathrm{f}\left(E_{k+q}^{v}\right) - \mathrm{f}\left(E_{k}^{v'}\right)}{\Omega - \left(E_{k+q}^{v} - E_{k}^{v'}\right) + i\eta} \right.$$

$$+ \frac{1}{4}\left[1 - \frac{\varepsilon_{k+q}^{v}\varepsilon_{k}^{v'} + \Delta_{k+q}^{v}\Delta_{k}^{v'}}{E_{k+q}^{v}E_{k}^{v'}}\right]\frac{1 - \mathrm{f}\left(E_{k+q}^{v}\right) - \mathrm{f}\left(E_{k}^{v'}\right)}{\Omega + \left(E_{k+q}^{v} + E_{k}^{v'}\right) + i\eta}$$

$$\left. + \frac{1}{4}\left[1 - \frac{\varepsilon_{k+q}^{v}\varepsilon_{k}^{v'} + \Delta_{k+q}^{v}\Delta_{k}^{v'}}{E_{k+q}^{v}E_{k}^{v'}}\right]\frac{\mathrm{f}\left(E_{k+q}^{v}\right) + \mathrm{f}\left(E_{k}^{v'}\right) - 1}{\Omega - \left(E_{k+q}^{v} + E_{k}^{v'}\right) + i\eta}\right\} \qquad 4.3$$

where we define the quasiparticle energy E_k^v in the "n"-th band with momentum k by the relation, $E_k^v = [(\varepsilon_k^v)^2 + (\Delta_k^v)^2]^{1/2}$. Consequently, , where ε_k^v is the normal-state eigen-energy relative to the Fermi level, and $\mathrm{f}(E_k^v)$ denotes the Fermi function for quasiparticles resonances will occur at energies

$$\Omega_{r1} = \left|\Delta_\beta\right| + \left|\Delta_{\gamma/\delta}\right| \sim 1.5\left|\Delta_{\gamma/\delta}\right|$$

$$\Omega_{r2} = \left|\Delta_\alpha\right| + \left|\Delta_{\gamma/\delta}\right| \sim 2\left|\Delta_{\gamma/\delta}\right| \qquad 4.4$$

where $\Delta_\alpha, \Delta_\beta,$ and $\Delta_{\gamma/\delta}$ are the different superconducting gaps on different pieces of the Fermi surface [110]. Generally, $\Delta_\alpha \approx \Delta_{\gamma/\delta} \approx 2\Delta_\beta$ where α , β represents the inner and outer hole pockets at Γ and γ/δ represents the electron pockets at the two M high-symmetry points of the Brillouin zone, as shown in Figure 4.2(a) [110]. These magnetic resonances scale with the superconducting gaps and should disappear above T_C. At sufficiently high energies, these resonances should be observable in the tunneling spectra.

In the remaining parts of this chapter we present experimental STS studies that provide evidence for two-gap superconductivity with sign changing s-wave pairing potential.

4.2 Experimental Methods and Sample Preparation

Similarly to the cuprate superconducting samples described in Chapter 5, surface preparation of the samples is extremely important. The $Ba(Fe_{1-x}Co_x)_2As_2$ single crystals are air sensitive and will degrade quickly in any ambient atmosphere due to the reaction of Ba with CO_2, which would create an effective dead layer on the surface. This is potentially devastating as STM is a highly surface-sensitive measurement. To prevent contamination of the sample surface, the sample must be prepared in an inert gas atmosphere or at ultra-high vacuum. Previous iron pnictide STM studies of the hole type and electron type "122" systems [117–119] cleaved the samples *in situ* in ultra-high vacuum conditions at cryogenic temperatures. The resulting sample surfaces all exhibited strong (2x1) reconstruction of the Fe(Co)-layer and STS measurements of the tunneling spectra revealed a single highly inhomogeneous superconducting gap [117, 118]. In the nonsuperconducting limit, nematic surface reconstructions were observed [119]. In contrast, for this thesis, the $Ba(Fe_{1-x}Co_x)_2As_2$ single crystals were first cleaned in a ethanol wash. The crystals were cleaved at room temperature in a pure argon environment inside a glove box with all Teflon tools. Here we note that the sample preparation temperature was above the tetragonal-to-orthorhombic structural phase transition. The samples were then loaded into the STM probe inside the glove box according to the method outlined in Chapter 2. The STM was then loaded into a cryogenic dewar and rapidly pumped downed

to pressures < 10^{-7} torr and quickly cooled to a temperature of T = 6 K , where the charcoal pump inside the STM probe became activated so that the overall vacuum was down to ~ 10^{-10} Torr. It should be noted that even in cryogenic temperatures and ultra-high vacuum conditions with a residual argon atmosphere, the surface layer of the crystal still continues to degrade, forming an eventual dead layer. The timeframe for this degradation is ~ 7–8 days, after which the surface is no longer superconducting. The sample must then be removed from the STM and the above surface preparation process repeated. The single crystals were grown from the flux method [120], with details of the synthesis and characterization described elsewhere [120–122].

Once at T= 6 K, topographic and spectroscopic studies were performed over numerous regions of the samples. The average scan consisted of a 6 nm × 6 nm area with a resolution of 128 pixels × 128 pixels. The tunnel junction resistance was maintained at ~ 1.0 GΩ along the c-axis. At each pixel the tunneling conductance (dI/dV) vs. energy (eV), topography, and tunneling current were measured simultaneously.

4.3 Experimental Results

4.3.1 Zero-Field Measurements

In Figure 4.3 we present representative normalized tunneling spectra for both underdoped (x = 0.06, T_C = 14 K) and overdoped (x = 0.12, T_C = 20 K) $Ba(Fe_{1-x}Co_x)_2As_2$ single crystals for two different temperatures below T_C at T = 6 K and T = 10, 14 K for underdoped and overdoped, respectively, and also for one temperature above T_C for both samples. The tunneling data are shown in open symbols. Two predominant tunneling gap

features are observable for both doping levels. As shown in Figure 4.3(a–b) both gaps shrink with increasing temperature and eventually disappear above T = T_C. The sizes of each gap for T = 6 K are $\Delta_\beta \sim 4$ meV and $\Delta_{\alpha,\gamma/\delta} \sim 8$ meV for the underdoped sample and $\Delta_\beta \sim 5$ meV and $\Delta_{\alpha,\gamma/\delta} \sim 10$ meV for overdoped sample. We have assigned Δ_β for the smaller gap and $\Delta_{\alpha,\gamma/\delta}$ for the larger gap. The measured gap values are in relatively good agreement with ARPES data [123–125]. To analyze the spectra, fittings of the T= 6 K tunneling spectra were made using a phenomenological fitting generalized from Dynes formula [126] and we restricted the analysis to two-gap superconductivity. Specifically, the normalized tunneling conductance $\bar{G}$ for a metal-insulator-superconductor junction in the case of a two-gap superconductor may be given by:

$$\bar{G} = A + \sum_{i=\beta,(\alpha,\gamma/\delta)} B_i \int Re\left[\frac{(E-i\Gamma_i)\left({}^{df}/_{dE}\right)_{E-eV}}{\sqrt{(E-i\Gamma_i)^2-\Delta_i^2}}\right] dE \qquad 4.5$$

where A and Bi are positive constants, Γ_i denotes the quasiparticle scattering rate associated with the superconducting gap Δ_i and f(E) is the Fermi function. From this fitting we can derive temperature-dependent values of both gaps. Both fittings are shown in Figure 4.3(a–b) as solid black lines and are in fair agreement with experimental data but are not ideal as Dyne's formula does not explicitly consider sign changing s-wave superconductivity nor the possibility of coexisting competing orders with superconductivity. Using this crude approximation we find that the quasiparticle scattering rates for under- and overdoped sample are fairly large $\left(\Gamma_{\alpha,\gamma/\delta}/\Delta_{\alpha,\gamma/\delta}\right) = 0.4$ and 0.5 for x = 0.06 and x = 0.12 and with $\left(\Gamma_\beta/\Delta_\beta\right) = 0.1$ for both x = 0.06 and x = 0.12.

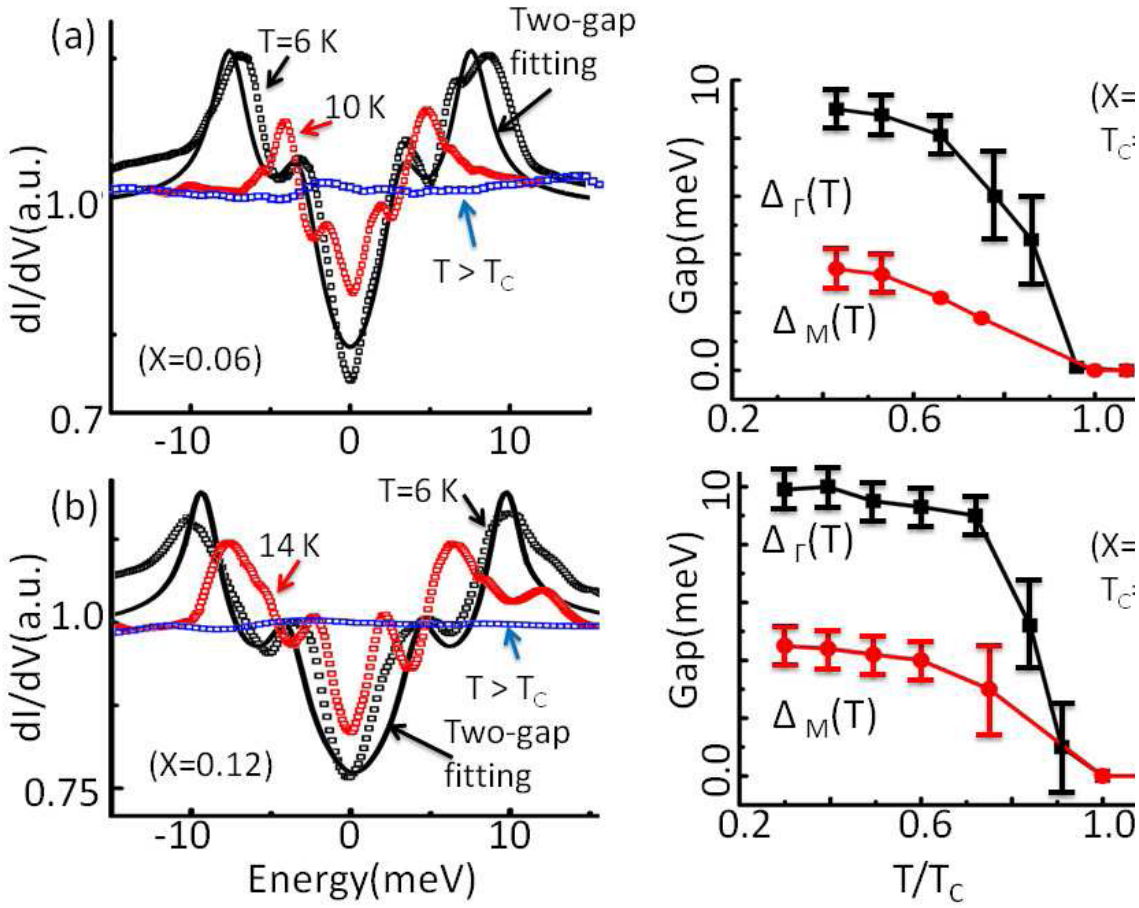

Figure 4.3 : Quasiparticle tunneling spectra and temperature vs. gap. (a)(left panel) Tunneling spectra (open symbols) for underdoped (x = 0.06) $Ba(Fe_{1-x}Co_x)_2As_2$ at T = 6 ,10, and 15 K. Below T_C both tunneling spectra exhibit two gap features that close above T_C. A Dynes fitting (solid black curve) for the T = 6 K curve. (right panel) Superconducting gap vs. temperature for both gap features that shows both gaps disappearing above T_C. (b)(left panel) Tunneling spectra (open symbols) for underdoped (x = 0.12) $Ba(Fe_{1-x}Co_x)_2As_2$ at T = 6 ,14, and 21 K. Below T_C both tunneling spectra exhibit two-gap features that close above T_C. A Dynes fitting (solid black curve) for the T = 6 K curve. (right panel) Superconducting gap vs. temperature for both gap features that shows both gaps disappearing above T_C

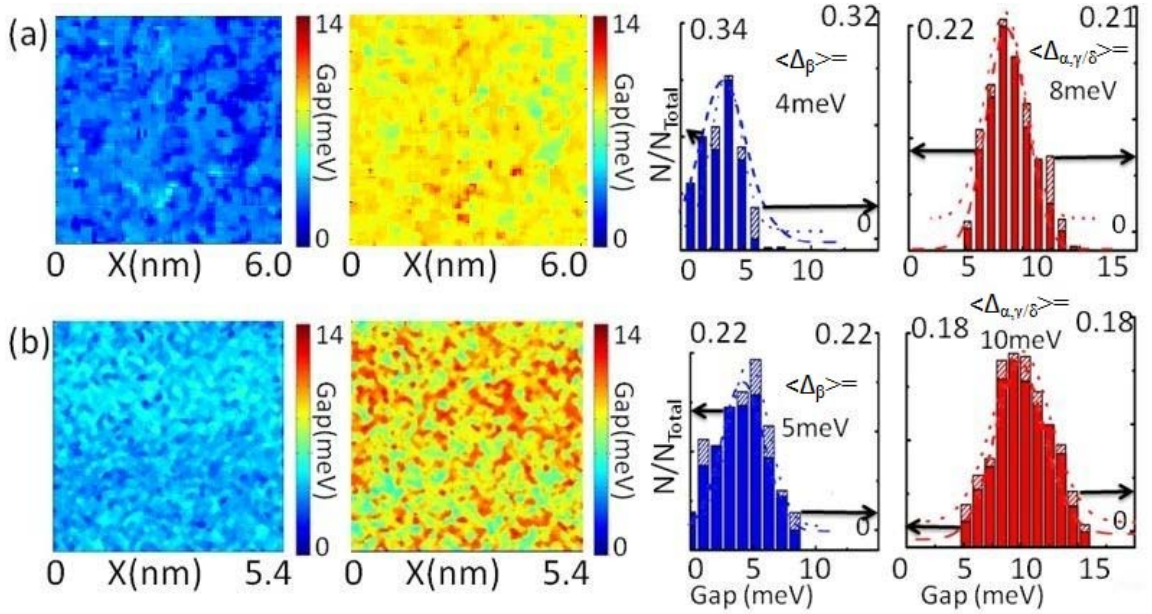

Figure 4.4: Gap maps and gap histograms. (a)(from left to right) Gap maps for the underdoped sample for both Δ_β and $\Delta_{\alpha,\gamma/\delta}$ with the corresponding histograms for both gaps respectfully. The solid bars represent quasiparticle gaps and the shaded bars represent quasihole gaps. The histograms show particle symmetry in the superconducting gaps. (b)(from left to right) Gap maps for the overdoped sample for both Δ_β and $\Delta_{\alpha,\gamma/\delta}$ with the corresponding histograms. The solid bars represent quasiparticle gaps and the shaded bars represent quasihole gaps.

In Figure 4.4(a-b), we have plotted the 2D gap maps for both Δ_β and $\Delta_{\alpha,\gamma/\delta}$ of both the under- and overdoped samples where the value at every pixel is the calculated superconducting gap from tunneling spectra. The average superconducting gap values, $(\Delta_\beta = 4\ \text{meV})$ and $(\Delta_{\alpha,\gamma/\delta} = 8\ \text{meV})$ for underdoped (a) and $(\Delta_\beta = 5\ \text{meV})$ and $(\Delta_{\alpha,\gamma/\delta} = 10\ \text{meV})$ for overdoped (b), are determined empirically. The plots are over regions of $6 \times 6\ \text{nm}^2$ and $5.4 \times 5.4\ \text{nm}^2$ area. Also plotted in Figure 4.4(a–b, right panels) are the resulting histograms for the superconducting gap maps. We can observe that the superconducting gaps are particle-hole symmetric for both doping levels.

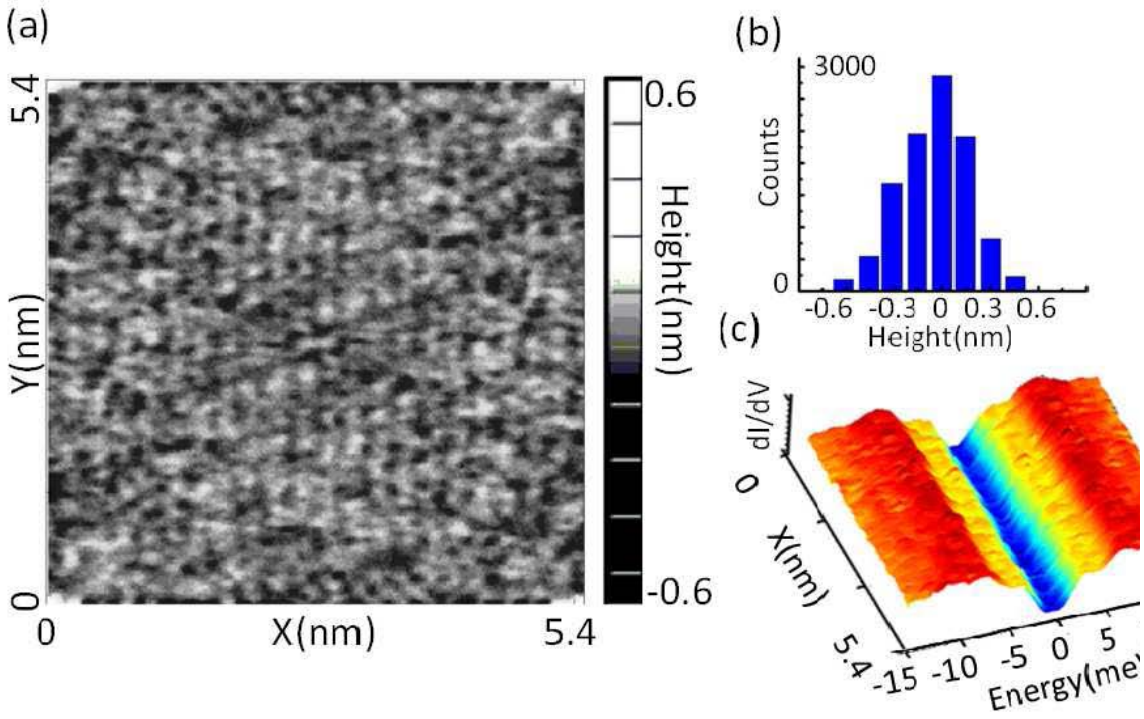

Figure 4.5: Topographic studies. (a) Atomically resolved topographic map that shows a fragmented surface but no apparent (2 x 1) surface reconstruction. (b) A histogram of the height variations of the topography in (a) showing a max variation less than one c-axis lattice constant. (c) A (dI/dV) vs. V linecut showing spatial evolution of the two gaps as a function position. The two gaps are consistent for ~ 90% of the spectra across the sample surface.

Topographic studies of both crystals reveal fragmented surfaces with no evident surface reconstruction as seen in other studies [117–119]. An example of an atomically resolved surface topography of the overdoped sample is shown in Figure 4.5(a) along with a height variation histogram (b). The overall height variations are limited to within one c-axis lattice constant of c_0 = 1.239 nm. We believe that apparent difference in results in comparison to other studies is due to our procedure of cleaving the samples at room temperature in an argon atmosphere above the structural phase transition temperature. Despite the fragmented surfaces, we observe consistent two-gap feature throughout the

scanned areas. This is demonstrated in Figure 4.5(c) where we have plotted a linecut of tunneling spectra vs. position. These results are in contrast to other studies [117–120] where the samples are cleaved at ultra-high vacuum at cryogenic temperatures and consequently only one superconducting gap is observed.

In Figure 4.6(a–b) we examine the spatial variations in the tunneling conductance at the gap energies, Δ_β and $\Delta_{\alpha,\gamma/\delta}$ by plotting conductance maps as well as their corresponding fast Fourier transforms. By taking the fast Fourier transform of the tunneling conductance, we can analyze the quasiparticle interference wave vectors. We find three dominate quasiparticle interferences occurring at three wave vectors. First we observe $\boldsymbol{q}_1$ across the two electron pockets in the Brillouin zone, $\boldsymbol{q}_1 \sim (\pm 2\pi, 0)$ or $(0, \pm 2\pi)$. The strong intensity of $\boldsymbol{q}_1 = \boldsymbol{2q}_2$ is in strong agreement with the presence of CDWs as describe previously. Secondly, we observe $\boldsymbol{q}_2$ resulting from scattering across the hole and electron pockets at Γ and M $\boldsymbol{q}_2 \sim (\pm\pi, 0)$ or $(0, \pm\pi)$, as seen in Figure 4.6(c). Third, we observe $\boldsymbol{q}_3$ between two electron pockets $\boldsymbol{q}_3 \sim (\pm\pi, \pm\pi)$ primarily for the overdoped sample. For the underdoped sample in Figure 4.6, we observe clear $\boldsymbol{q}_1$ and $\boldsymbol{q}_2$ while $\boldsymbol{q}_3$ occurs only faintly, which is consistent with the theoretical calculations for scattering from non-magnetic impurities in sign changing s-wave superconductivity as mentioned in Section 4.1. For the overdoped sample (Figure 4.6 (d)), $\boldsymbol{q}_1$,$\boldsymbol{q}_2$, and $\boldsymbol{q}_3$ are all strongly observed in the Fourier transform. While $\boldsymbol{q}_1$ and $\boldsymbol{q}_2$ are understood as above, the strong

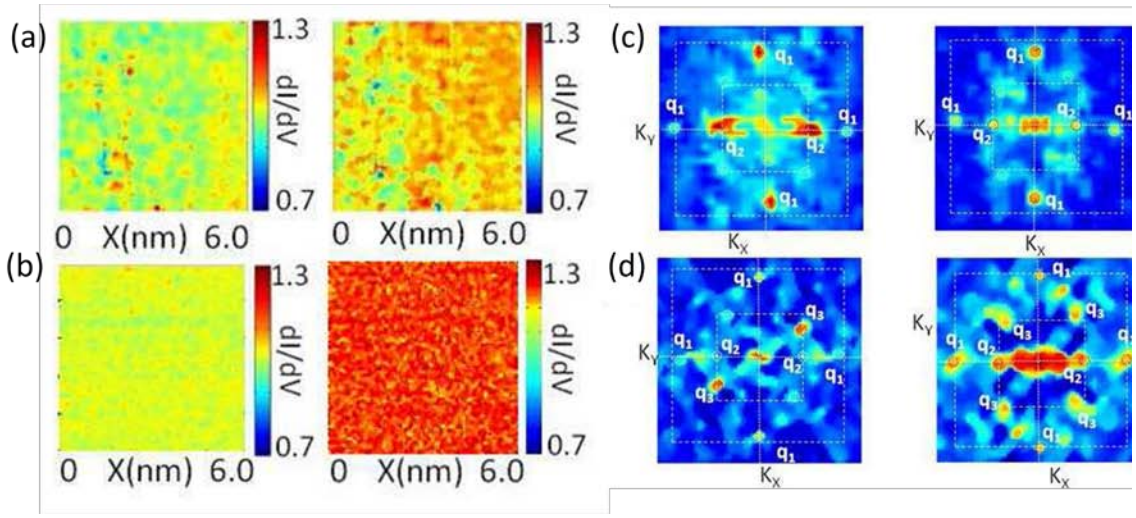

Figure 4.6 : Tunneling conductance maps of $Ba(Fe_{1-x}Co_x)_2As_2$ sample at the superconducting gap energies :$E = \Delta_\beta/e$, $\Delta_{\alpha,\gamma/\delta}/e$ for (a) underdoped (x=0.06) and (b) overdoped (x=0.12). (c) Fast Fourier transforms of the conductance maps in (a). The thin white lines represent the first and second Brillouin zones in momentum space. (d) Fast Fourier transforms of (b)

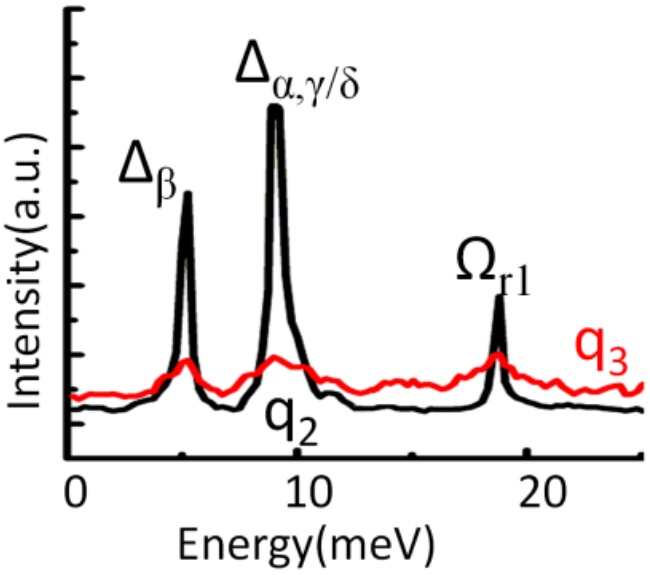

Figure 4.7 : $F(\boldsymbol{q},\omega)\ vs.\ \omega$ for underdoped $Ba(Fe_{1-x}Co_x)_2As_2$, showing only strong peaks at the $\omega=\Delta_\beta$, $\Delta_{\alpha,\gamma/\delta}$, and Ω_{r1} for wave vectors $\mathbf{q_2}$ (black) and $\mathbf{q_3}$ (red). The sharp QPI intensities occurring only at the superconducting gaps and magnetic resonance exclude the possibility of attributing these wave-vectors to Bragg diffractions of the reciprocal lattice vectors.

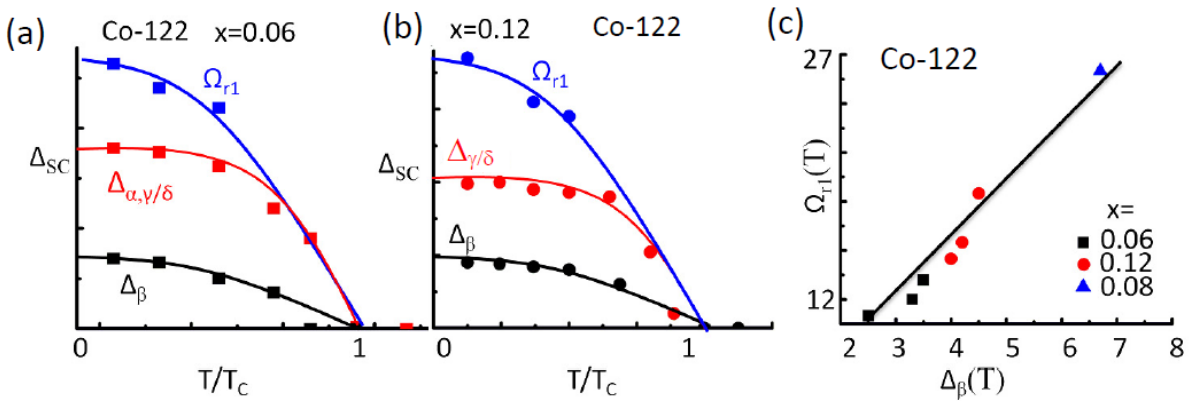

Figure 4.8: Temperature dependence of the superconducting gaps, $\Delta_\beta, \Delta_{\alpha,\gamma/\delta}$ and the magnetic resonance mode Ω_{r1} for both the (a) underdoped (x = 0.06) and (b) overdoped (x = 0.12) samples. (c) Correlation of the magnetic resonance mode Ω_{r1} and the superconducting gap Δ_β for three doping levels (x = 0.06, x = 0.08, and x = 0.12). The slope of the data points agree with the relation $\Omega_{r1} = |\Delta_\beta| + |\Delta_{\gamma/\delta}| \sim 1.5\,|\Delta_{\gamma/\delta}|$.

presence of $\boldsymbol{q}_3$ in the overdoped sample can be explained due to the larger density of Co-atoms on the surface Fe/Co layers. Unlike those in the bulk, the charge transfer from the surface Co-atoms is incomplete and so they may behave like magnetic impurities [106]. In both dopings, $\boldsymbol{q}_2$ has a preferred direction, which may be attributed to the orthorhombic nature of these samples. We note that the observed wave vectors exhibit energy and doping dependence. The sharp QPI intensities which occur only at the SC gap and magnetic resonance energies (as shown in Figure 4.7) exclude the possibility of attributing these wave-vectors to Bragg diffractions of the reciprocal lattice vectors, because Bragg diffraction points would *not* possess energy and doping dependence.

In all tunneling spectra, we observe the presence of magnetic resonance modes. The mode manifests as a spectra peak in the tunneling conductance. As shown in Section 4.1, the magnetic resonances should satisfy $\Omega_{r1} = |\Delta_\beta| + |\Delta_{\gamma/\delta}| \sim 1.5\,|\Delta_{\gamma/\delta}|$ and

$\Omega_{r2} = |\Delta_\alpha| + |\Delta_{\gamma/\delta}| \sim 2\ |\Delta_{\gamma/\delta}|$. We observe only one magnetic resonance Ω_{r1} in the overdoped sample due to a vanished α pocket where for the underdoped sample we observe the $\Omega_{r2} \sim 16$ meV. As predicted, the magnetic resonance modes scale with the superconducting gaps and vanish for $T > T_C$. In Figure 4.8(a–c) the correlation between temperature dependent superconducting gaps and magnetic resonances is shown.

In contrast to the underdoped and overdoped samples, STS studies on the optimally doped sample (x = 0.08 with T_C = 24 K) revealed that the majority of the sample showed only one large superconducting gap $\Delta_{\alpha,\gamma/\delta}$ ~14 ± 2 meV with a highly suppressed secondary gap $\Delta_\beta \sim 6 \pm 2$ meV. A magnetic resonance mode was also observed at $\Omega_{r2} = -26 \pm 3$ meV. It is unknown why the optimally doped sample exhibits a much weaker two gap-superconductivity, although a possible explanation is that strong fluctuation effects may have reduced the superconducting stiffness of the hole pockets, rendering weaker coherence peaks for the smaller gap in the optimally doped sample. A representative tunneling spectrum for the optimally doped sample is shown in Figure 4.9(a).

4.3.2 Magnetic Field Measurements

STS studies were performed on the optimally doped (x = 0.08) $Ba(Fe_{1-x}Co_x)_2As_2$ single crystal in magnetic fields of H = 1, 4 Tesla. All magnetic fields were applied parallel to c-axis of the crystal. All tunneling spectra revealed the presence of a single large superconducting gap $\Delta_{\alpha,\gamma/\delta}$ ~12 ± 2 meV at H = 1 Tesla while measurements at H = 4 Tesla revealed a large superconducting gap $\Delta_{\alpha,\gamma/\delta}$ ~12 ± 2 meV with a smaller gap $\Delta_\beta \sim 5$

± 2 meV. For the effect of magnetic fields on the superconducting gaps, the $\Delta_{\alpha,\gamma/\delta}$ gap values at H = 0 and 1 Tesla are plotted in Figure 4.9(b). The histograms show a clear reduction of the superconducting gap in the presence of a magnetic field as is expected.

Figure 4.10 shows plots of the Fourier transform of the tunneling conductance at the superconducting gap, $\Delta_{\alpha,\gamma/\delta}$ ~ 12, 14 meV for both H = 0 and 1 Tesla for the optimally doped sample. Following the analysis in Section 4.1, for scattering off nonmagnetic impurities in the presence of a finite magnetic field, there should be an enhancement of the quasiparticle interference wave vector $\boldsymbol{q}_3$ and a suppression of the $\boldsymbol{q}_2$ wave vector. As shown in Figure 4.10(a-b), this scenario is observed, providing confirmation for sign changing s wave pairing symmetry in the ferrous superconductors. Additionally, we also note the presence of $\boldsymbol{q}_1 = \boldsymbol{2q}_2$ in the Fourier transforms of the tunneling conductance of both H= 0 and 1 Tesla fields. As stated earlier the existence of $\boldsymbol{q}_1$ can only occur if a CDW

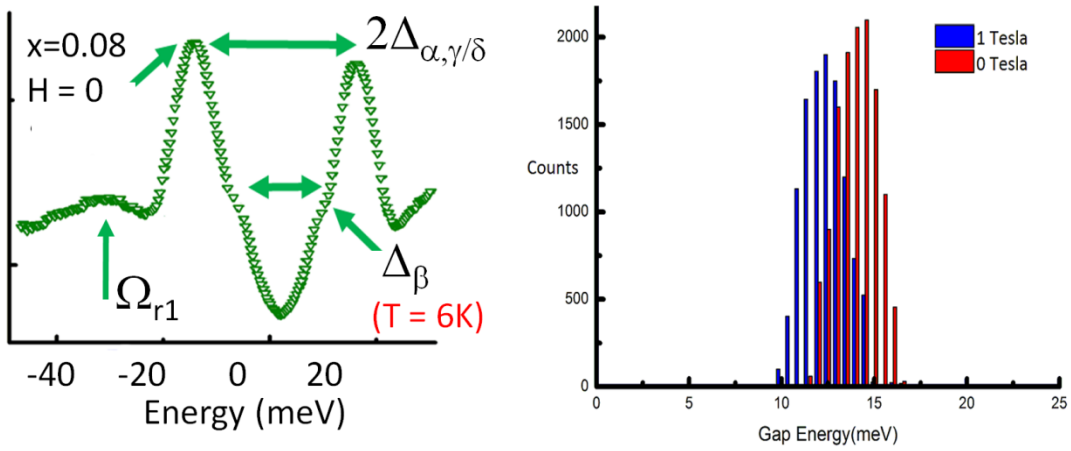

Figure 4.9: Optimally doped tunneling spectra. (a) H= 0 Tesla tunneling spectra for optimally doped $Ba(Fe_{1-x}Co_x)_2As_2$ showing two superconducting gaps at $\Delta_{\alpha,\gamma/\delta}$ ~ 14 meV and $\Delta_\beta \sim 6$ meV and the Ω_{r1} magnetic resonance. (b) Histogram of the $\Delta_{\alpha,\gamma/\delta}$ superconducting gap for both H = 0 and 1 Tesla

exists in the superconducting state. Similar to the cuprates, the presence of a CO would suggest the occurrence of a pseudogap like feature inside the vortex core.

Plotting the ratio of the tunneling conductances at energies $\omega = \Delta_{\alpha,\gamma/\delta}$ to $\omega = 0$ in a magnetic field (H=1 Tesla) reveals the presence of anisotropic vortices. The measured vortex separation distance is approximately 49 nm which is in good agreement with the expected vortex lattice constant, $a_0 \sim \sqrt{\Phi/B}$, which for H = 1 Tesla is ~ 49 nm. The anisotropic vortices have approximate dimensions of 5.0 nm x 2.5 nm. In Figure 4.11(a–c) we plot the vortex maps for H = 1 Tesla as well as a linecut of representative tunneling spectra through one of the observed vortex cores showing the evolution of tunneling spectra. Spectra from outside the vortex core reveal a single superconducting gap, $\Delta_{\alpha,\gamma/\delta}$ ~12 meV. This spectra closely resembles data taken at H= 0 Tesla. Spectra from inside the vortex core reveals single pseudogap-like feature with no superconducting characteristics. This finding is in contrast to previously published STS studies on the vortex-state of the iron-based superconductors that varied greatly [127, 128]. In one study [127], asymmetric vortex bound states appearing as sub gap peaks inside the vortex cores were observed in a hole-type 122 system $(Ba_{0.6}K_{0.4})Fe_2As_2$, which implied pure superconductivity in the ground state. In contrast, STS studies of an electron-type 122 system $Ba(Fe_{0.9}Co_{0.1})_2As_2$ found complete suppression of SC coherence peaks but no apparent sub gap peaks inside the vortex cores [128].

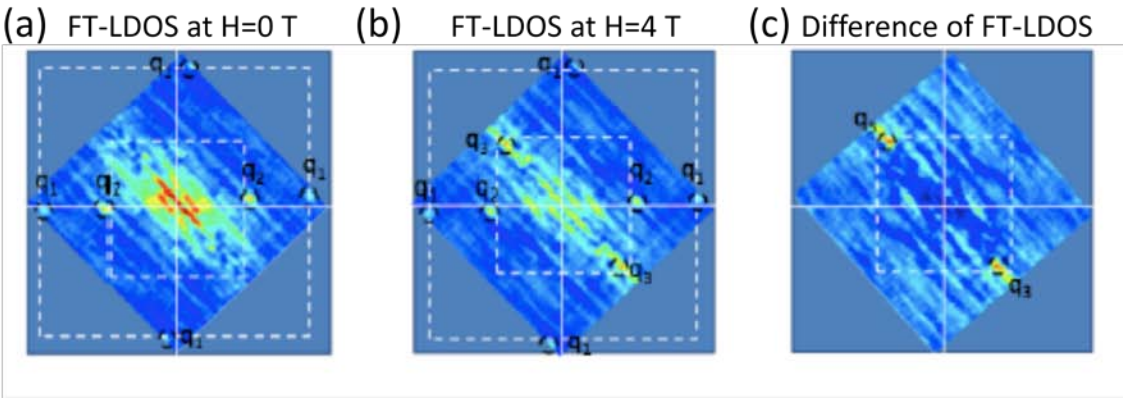

Figure 4.10: (a)-(b) Fourier transform of the conductance maps at ω= $\Delta_{\alpha,\gamma/\delta}$ for the optimally doped sample at H = 0 Tesla (a), H = 1 Tesla (b), and the difference of the two Fourier transforms (c). As shown in (c), the $\boldsymbol{q}_3$ wave vector is greatly enhanced in H = 1 Tesla as compared to H = 0 Tesla. The $\boldsymbol{q}_1 = \boldsymbol{2q}_2$ wave vector is present in both (a) and (b).

The presence of a pseudogap inside the vortex core seems to confirm the coexistence of a competing order and superconductivity. Without a competing order the inside vortex tunneling spectra should reveal the presence of Andreev-bound states due to the suppression of superconductivity. The presence of a pseudogap therefore suggests that the optimally doped sample resides in the region of the phase diagram where AFM spin density waves and superconductivity coexist. Representative single point, inter- and intra-vortex tunneling spectra in H = 4 Tesla are plotted in Figure 4.12(a–d). As we can observe, unlike H = 0 and 1 Tesla, the Δ_β superconducting gap is less suppressed, while the magnetic resonance mode at Ω_{r1} is greatly enhanced. The enhanced magnetic mode may be understood as enhanced inelastic scattering of quasiparticles between the

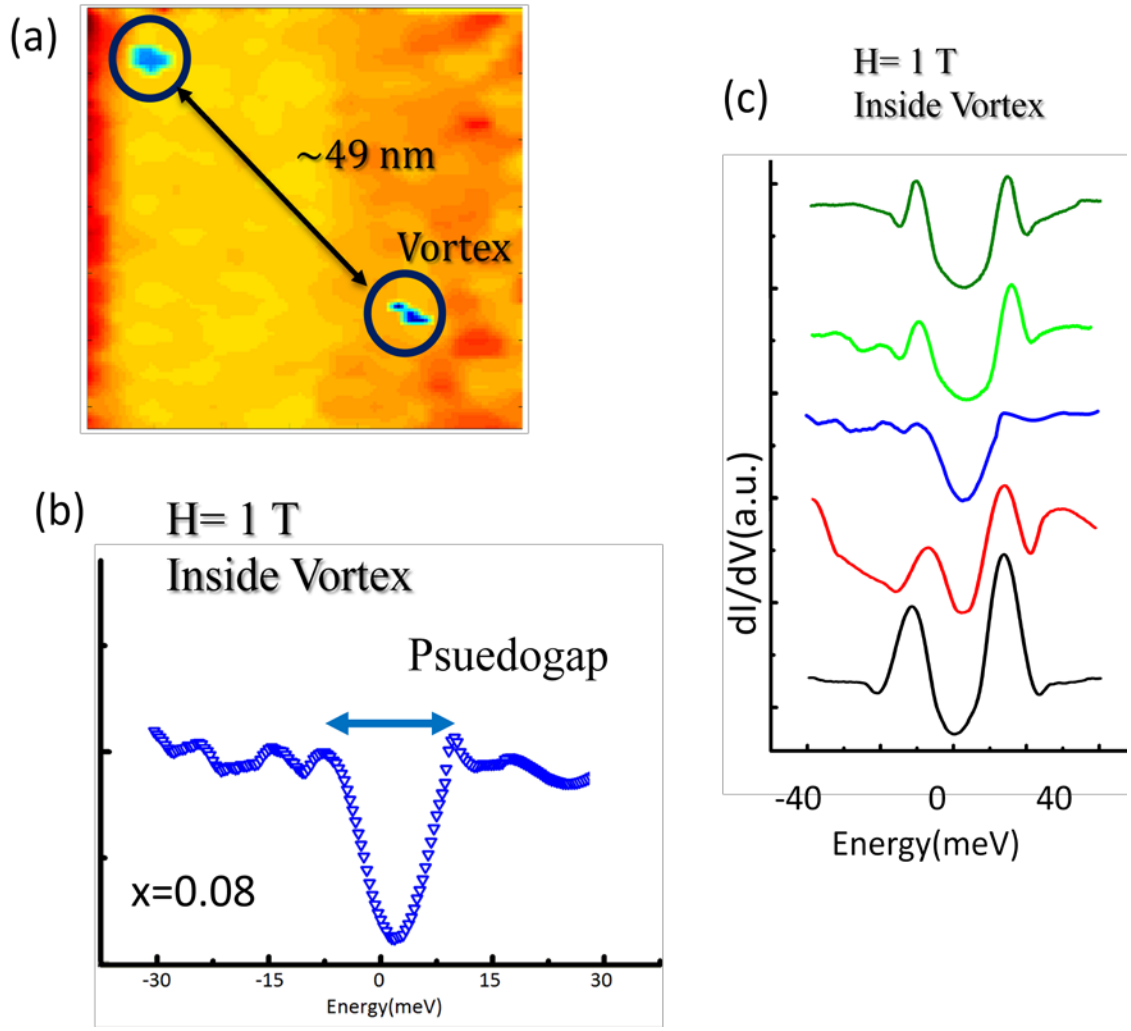

Figure 4.11: (a) Conductance ratio plot revealing two anisotropic vortices. The vortex separation agrees with the predicted vortex lattice constant of ~ 49 nm. (b) Representative spectra from inside the vortex core showing pseudogap. (c) A linecut of tunneling spectra for the top vortex in (a) showing evolution of a superconducting gap to a pseudogap to a superconducting gap

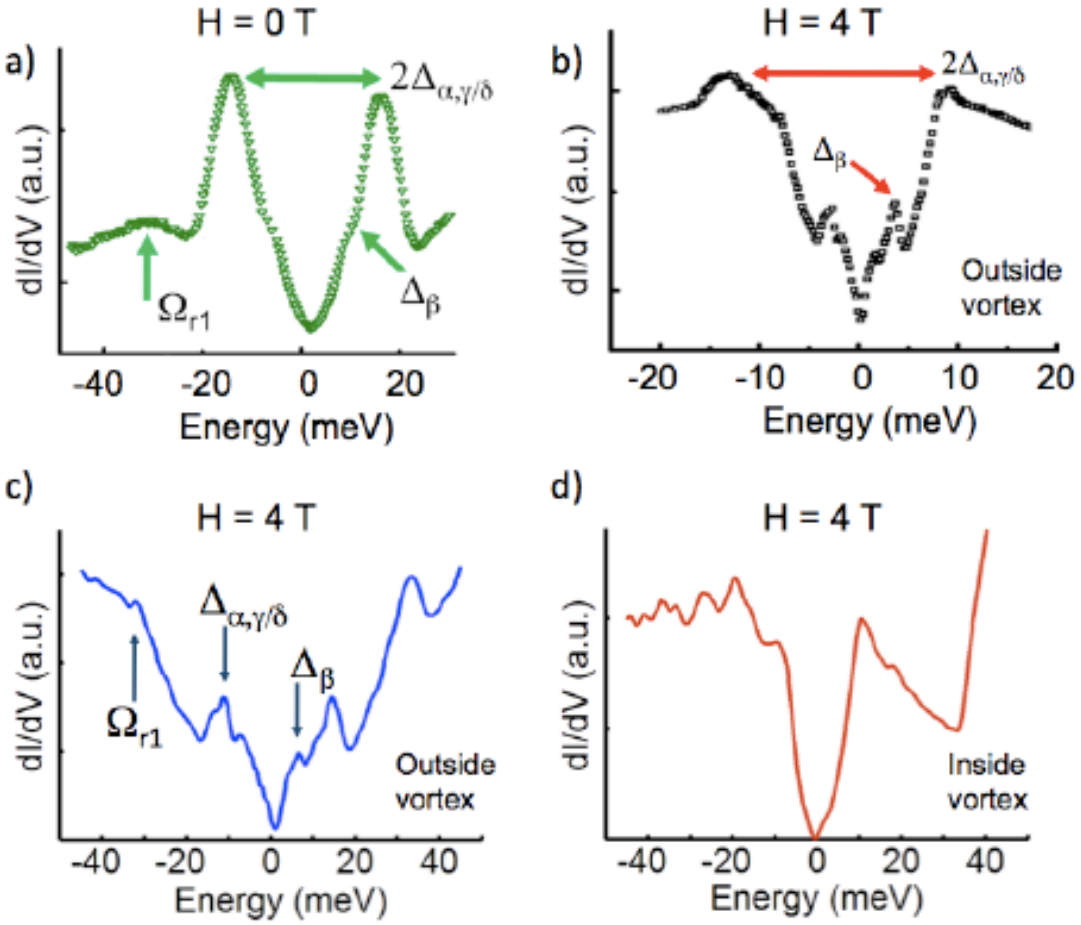

Figure 4.12: Optimally doped tunneling spectra in a field. (a) Representative spectra of the optimally doped sample with H = 0 T. (b) A representative outside vortex core spectra at H = 4 T. $\Delta_{\alpha,\gamma/\delta}$ ~ 12 ± 2 meV and Δ_{β} ~ 5 ± 2 meV. (c) Another outside vortex core spectra $\Delta_{\alpha,\gamma/\delta}$ ~ 13 ± 2 meV, Δ_{β} ~ 6 ± 2 meV, and Ω_{r2} ~ -30 ± 2 meV. The magnetic resonance mode is enhanced when compared to H = 0 T. (d) Inside vortex core spectra at H = 4 T, showing pseudogap like characteristics. Images (c–d) courtesy of R. Wu.

electron pockets of the Fermi surface in a magnetic field. The 4 Tesla intravortex spectra (Figure 4.12(d)) appears to have pseudogap characteristics, much like the intravortex spectra at 1 Tesla. The measured vortex lattice constant is approximately 25 nm, which is

comparable to the theoretically predicted value of 24.5 nm. The presence of a pseudogap inside the vortex core in both H = 1 and 4 Tesla magnetic fields lends further support towards the coexistence of competing orders with superconductivity in the electron doped "122" systems.

4.4 Discussion

In summary, we have observed two-gap superconductivity for multiple doping levels in the $Ba(Fe_{1-x}Co_x)_2As_2$ single crystals. Both superconducting gaps decrease monotonically in size with increasing temperature and disappear for temperatures above the superconducting transition temperature, T_C. Magnetic resonant modes that follow the temperature dependence of the superconducting gaps have been identified in the tunneling quasiparticle spectra. Together with quasiparticle interference (QPI) analysis and magnetic field studies, this provides strong evidence for two gap sign-changing s-wave superconductivity.

Chapter 5

Electronic Properties of Graphene

Dirac materials are a new class of matter that offer promising new physics and a new fertile ground for possible applications. The charge carriers of such materials obey the Dirac equation for relativistic particles and can be thought of as Dirac fermions. Foremost among these materials are graphene and three-dimensional topological insulators. In this chapter the basic electronic and structural properties of graphene are discussed. Graphene with its unique physical properties and its potential uses in nanoscale applications make it a particularly compelling area of study.

5.1 Graphene Band Structure

Graphene, a mono-atomic layer two-dimensional (2D) crystal, consists of six carbon atoms bonded together in a hexagonal lattice with the charge carriers forming a two-dimensional electron gas with a relativistic dispersion near two Dirac points in the Brillouin zone. Graphene was mechanically isolated in 2004 by A.K. Geim and K.S Novoselov from the University of Manchester [45]. In the short time since it was successfully isolated, many remarkable electronic and structural properties have been found in graphene, such as the Dirac-like band structure; an ambipolar electric field effect where the concentration of charge carriers can be tuned continuously from electrons to holes by adjusting the gate voltage [45]; exceptionally high mobilities [46, 47], the integer and fractional quantum Hall

effect (IQHE and FQHE) [48–51]; and a minimum conductance of $4e^2/\hbar\pi$ in the limit of zero charge-carriers[52]. The high mobilities make graphene an excellent candidate to be used in components of integrated circuits and it may be possible that graphene will become an important supplement to future silicon-based technologies. In this section we review the 2D band structure of graphene.

Each carbon atom in graphene has four valence electrons; three of these electrons are covalently bonded to neighboring carbon atoms through sp^2 hybridization while the remaining electron is in the $2p_z$ orbital which is perpendicular to the graphene plane [130] and participates in conduction throughout the graphene sheet. To describe the electronic band structure of graphene, it is appropriate to use the tight binding model where the atomic description of isolated atoms is used but where the overlap of atomic functions is large enough to require corrections.

Thus, we follow the derivation in Dresselhaus [130]. The wave function ψ for a single isolated atom and the full wave-function of the lattice are substantially different as are the Hamiltonians for each. Accordingly, the Schrödinger wave equation for a single isolated atom is given by

$$H_{atom}\psi_{atom} = E\psi_{atom} \tag{5.1}$$

where H_{atom} is the Hamiltonian for an individual isolated atom, ψ_{atom} is the wave function for an individual isolated atom, and E is the energy eigenvalue. In the case of a lattice, because of the translational symmetry of the unit cells in the direction of the lattice vectors, $\overrightarrow{\boldsymbol{a_i}}$, any wave function of the lattice,Ψ, should satisfy the Bloch' theorem

$$T_{a_i}\Psi = e^{i\vec{k}\cdot\vec{a_i}}\Psi \tag{5.2}$$

where T_{a_i} is a translational operation along the lattice vector, $\overrightarrow{\boldsymbol{a_i}}$, and $\vec{\boldsymbol{k}}$ is the wave vector. A possible Bloch wave function that satisfies this requirement is given by

$$\Phi_i(\vec{\boldsymbol{k}},\vec{\boldsymbol{r}}) = \frac{1}{\sqrt{N}}\sum_{\vec{\boldsymbol{R}}}^{N} e^{i\vec{\boldsymbol{k}}\cdot\overrightarrow{\boldsymbol{a_i}}}\phi_i(\vec{\boldsymbol{r}}-\vec{\boldsymbol{R}}) \quad (\mathrm{i} = \mathrm{A}, \mathrm{B}) \tag{5.3}$$

and $\vec{\boldsymbol{R}}$ is the position of the atom and ϕ_i denotes the atomic wave-function. N represents the total number of unit cells in the lattice. The unit cell of graphene contains two atoms typically denoted as A and B atoms or two equivalent carbon sublattices. The real space unit vectors $\overrightarrow{\boldsymbol{a_1}}$ and $\overrightarrow{\boldsymbol{a_2}}$ of the hexagonal lattice are expressed as

$$\overrightarrow{\boldsymbol{a_1}} = \left(\frac{a\sqrt{3}}{2}, \frac{a}{2}\right), \quad \overrightarrow{\boldsymbol{a_2}} = \left(\frac{a\sqrt{3}}{2}, \frac{-a}{2}\right) \tag{5.4}$$

where a is the lattice constant of 0.246 nanometers as illustrated in Figure 5.1(a). Correspondingly the reciprocal lattice wave vectors are defined as

$$\overrightarrow{\boldsymbol{b_1}} = \left(\frac{2\pi}{a\sqrt{3}}, \frac{2\pi}{a}\right), \quad \overrightarrow{\boldsymbol{b_2}} = \left(\frac{2\pi}{a\sqrt{3}}, \frac{-2\pi}{a}\right). \tag{5.5}$$

An image of the carbon lattice, the unit cell lattice vectors, and the reciprocal lattice is shown in Figure 1. The wavefunction of the lattice can be expressed by a linear combination of the Bloch functions, $\Phi_{j'}$ as follows

$$\Psi_{\mathrm{j}}(\vec{\boldsymbol{k}},\vec{\boldsymbol{r}}) = \sum_{\mathrm{j}'=1}^{\mathrm{n}} \mathrm{C}_{\mathrm{j}\,\mathrm{j}'}(\vec{\boldsymbol{k}})\Phi_{j'}(\vec{\boldsymbol{k}},\vec{\boldsymbol{r}}) \tag{5.6}$$

where the coefficients, $\mathrm{C}_{\mathrm{j}\,\mathrm{j}'}$, must be determined. Generically we would consider a wave function of the form $\Psi = C_A\Phi_A(\vec{\boldsymbol{r}}) + C_B\Phi_B(\vec{\boldsymbol{r}}-\vec{\boldsymbol{d}})$ where A and B represent the two inequivalent carbon atoms at A and B as shown in Figure 5.1. The j[th] eigenvalue $E_j(\vec{\boldsymbol{k}})$ of the lattice's wave function, $\Psi_{\mathrm{j}}(\vec{\boldsymbol{k}},\vec{\boldsymbol{r}})$, as a function of $\vec{\boldsymbol{k}}$ is given by

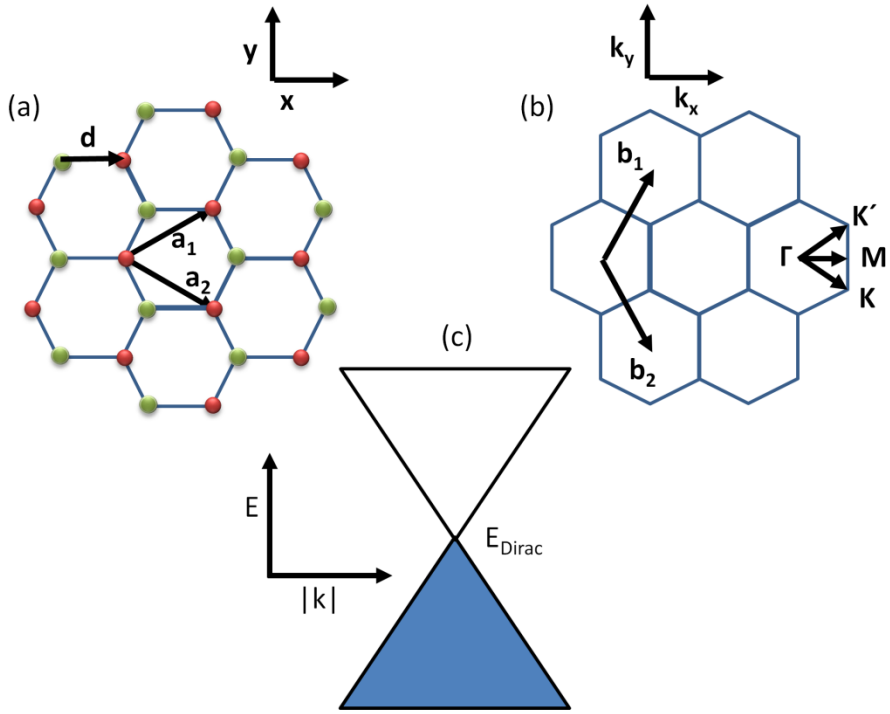

Figure 5.1: Graphene lattice: (a) The real space lattice showing both sublattices with lattice vectors $\overrightarrow{\boldsymbol{a_1}} = \left(\frac{a\sqrt{3}}{2}, \frac{a}{2}\right)$, $\overrightarrow{\boldsymbol{a_2}} = \left(\frac{a\sqrt{3}}{2}, \frac{-a}{2}\right)$, (b) Reciprocal space lattice showing reciprocal lattice vectors $\overrightarrow{\boldsymbol{b_1}} = \left(\frac{2\pi}{a\sqrt{3}}, \frac{2\pi}{a}\right)$, $\overrightarrow{\boldsymbol{b_2}} = \left(\frac{2\pi}{a\sqrt{3}}, \frac{-2\pi}{a}\right)$, (c) Linear density of states near the K or K' points

$$E_j(\vec{\boldsymbol{k}}) = \frac{\langle \Psi_j | \mathrm{H_{lat}} | \Psi_j \rangle}{\langle \Psi_j | \Psi_j \rangle} \qquad 5.7$$

if we define the following, $\mathrm{H_{jj'}}$ and $\mathrm{S_{jj'}}$, as the transfer integral matrices and overlap integral matrices, they are explicitly given by

$$\mathrm{H_{jj'}} = \langle \Phi_j | \mathrm{H_{lat}} | \Phi_{j'} \rangle, \mathrm{S_{jj'}} = \langle \Phi_j | \Phi_{j'} \rangle. \qquad 5.8$$

We can substitute Equation 5.6 into Equation 5.7 and with a change of subscripts the following is obtained

$$E_i(\vec{\boldsymbol{k}}) = \frac{\sum_{j,j'=1}^{n} C_{ij}^{*} C_{ij'} \langle \Phi_j | H_{lat} | \Phi_{j'} \rangle}{\sum_{j,j'=1}^{n} C_{ij}^{*} C_{ij'} \langle \Phi_j | \Phi_{j'} \rangle} = \frac{\sum_{j,j'=1}^{n} H_{jj'}(\vec{\boldsymbol{k}}) C_{ij}^{*} C_{ij'}}{\sum_{j,j'=1}^{n} S_{jj'}(\vec{\boldsymbol{k}}) C_{ij}^{*} C_{ij'}}. \quad 5.9$$

The coefficients C_{ij} are found by minimizing $E_i(\vec{\boldsymbol{k}})$. If we set the derivative of $E_i(\vec{\boldsymbol{k}})$ with respect to C_{ij} equal to zero and multiply both sides by $\sum_{j,j'=1}^{n} S_{j,j'}(\vec{\boldsymbol{k}}) C_{ij}^{*} C_{ij'}$ we can obtain the following condition for finding eigenvalues, $E_i(\vec{\boldsymbol{k}})$,

$$H_{lat} C_i = E_i(\vec{\boldsymbol{k}}) S \boldsymbol{C_i} \quad 5.10$$

$$\boldsymbol{C_i} = \begin{pmatrix} C_{i1} \\ \cdots \\ C_{iN} \end{pmatrix}$$

Solving for the coefficients is equivalent to solving the secular equation for E which is given by

$$det[H_{lat} - ES] = 0 \, . \quad 5.11$$

So in order to obtain the band structure of graphene we solve Equation 5.11. For the tight binding model we consider only nearest-neighbor interactions (the A atom and its three neighboring B atoms) when calculating the matrix elements of H and S. Solving for the off diagonal terms of the Hamiltonian and noting $H_{AB} = H_{BA}^{*}$,we find

$$H_{AB} = t\left(e^{i\vec{\boldsymbol{k}}\cdot\overrightarrow{\boldsymbol{R_1}}} + e^{i\vec{\boldsymbol{k}}\cdot\overrightarrow{\boldsymbol{R_2}}} + e^{i\vec{\boldsymbol{k}}\cdot\overrightarrow{\boldsymbol{R_3}}}\right) = t f(k) \quad 5.12$$

where $\overrightarrow{\boldsymbol{R_i}}$ denotes the locations of the three nearest neighbors and t is the nearest neighbor hopping constant. Using *x*, *y* coordinates we find that $f(k)$ is

$$f(k) = e^{ik_x a/\sqrt{3}} + 2e^{-ik_x a/2\sqrt{3}} \cos\left(\frac{k_y a}{2}\right). \quad 5.13$$

Taking $H_{AA} = H_{BB} = \epsilon_{2p} = 0$, this results in finding the following matrices for the Hamiltonian and the overlap function matrix as

$$H_{lat} = \begin{pmatrix} 0 & tf(k) \\ tf(k)^* & 0 \end{pmatrix} \; S = \begin{pmatrix} 1 & sf(k) \\ sf(k)^* & 1 \end{pmatrix} \qquad 5.14$$

resulting in the energy dispersion relation

$$E(\vec{\boldsymbol{k}}) = \frac{\pm t\omega(\vec{\boldsymbol{k}})}{1 \pm s\omega(\vec{\boldsymbol{k}})} \qquad 5.15$$

where $\omega(\vec{\boldsymbol{k}}) = \sqrt{|f(\boldsymbol{k})|^2}$**.** The tight-binding Hamiltonian in terms of creation and annihilation operators can also be written as [65]

$$H = -t\sum_{\langle i,j\rangle,\sigma}\left(a^{\dagger}_{\sigma,i}b_{\sigma,j} + h.c.\right) - t'\sum_{\langle i,j\rangle,\sigma}\left(a^{\dagger}_{\sigma,i}a_{\sigma,j} + b^{\dagger}_{\sigma,i}b_{\sigma,j} + h.c.\right) \quad 5.16$$

where $a^{\dagger}_{\sigma,i}(a_{\sigma,j})$ creates (annihilates) an electron with spin σ ($\sigma = \uparrow, \downarrow$) on sublattice A, $b^{\dagger}_{\sigma,i}(b_{\sigma,j})$ creates (annihilates) an electron with spin σ on sublattice B. The t and t' represent the nearest neighbor hopping energy (from one sublattice to another) and next nearest neighbor hopping energy (hopping in the same sublattice), respectively. In the limit of nearest neighbor interaction, we take t' to be zero. Using the parameters s = 0.129<<1 and t = -3.0033 eV ~ 3 eV [110] and inserting them into Equation 5.15, we find in two-dimensional Cartesian coordinates that

$$E_{2D}(k_x, k_y) = \mp 3\sqrt{1 + 4\cos\left(\frac{\sqrt{3}k_x a}{2}\right)\cos\left(\frac{k_y a}{2}\right) + 4\cos^2\left(\frac{k_y a}{2}\right)}\,. \quad 5.17$$

Hence, in this nearest-neighbor tight-binding approximation, there are two bands, bonding and antibonding and are degenerate at the K points. There are six K points where two bands meet within the Brillouin zone as shown in Figure 5.2. The 2D graphene energy band is ot discontinuous. Rather, the valence band (bonding) and the conduction band

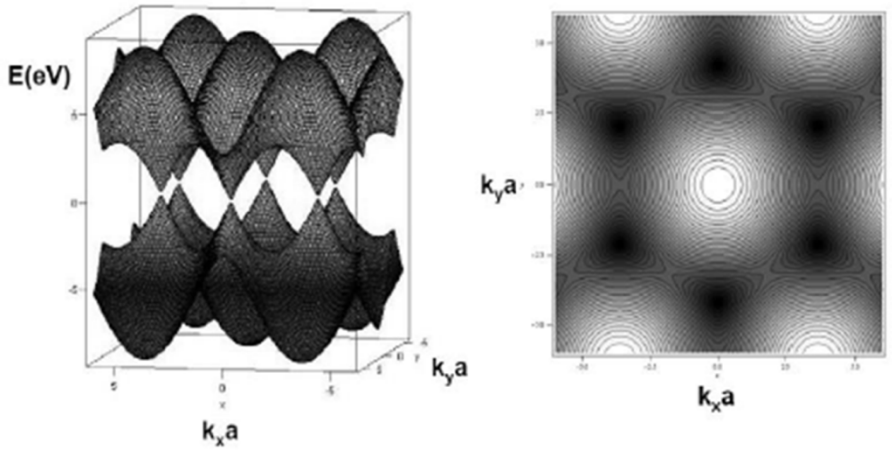

Figure 5.2: (a) Three-dimensional E vs. momentum (k_x,k_y) plot of Equation 5.17 showing linear dispersion relation at the K and K' points. (b) Contour plot of the lower band showing the K and K' points. Image taken from [149].

(antibonding) touch at these points. At the apex of the cones which is known as the Dirac point, the electrons and holes are degenerate. For this reason graphene is known as a semi-metal or a zero-gap semiconductor. Taylor expanding the Equation 5.17 at or near the two inequivalent K and K' points in the 1st Brillouin zone gives[130]

$$E_{2D}(k_x, k_y) \approx \pm v_f \hbar |\vec{\boldsymbol{k}}| \qquad 5.18$$

where v_f is the Fermi velocity with a value of $c/300$[45]. The linear relation between energy and momentum is demonstrated in Figure 5.2. As a result of this conical band structure, the charge carriers of graphene at energies near the Dirac energy (E_d) have a vanishing effective mass and obey the Dirac equation for relativistic particles, with a reduced speed of light equal to the Fermi velocity v_f [132]. Therefore, these charge carriers can be thought of as massless Dirac fermions [132] and the Hamiltonian for these low-energy excitations is that of a (2+1) relativistic quantum system described by the Dirac equation for particles with zero mass and spin ½ [134, 135].

$$H = v_f \hbar \begin{pmatrix} 0 & k_x - ik_y \\ k_x + ik_y & 0 \end{pmatrix} = v_f \hbar \, \vec{\boldsymbol{\sigma}} \cdot \vec{\boldsymbol{k}} \qquad 5.19$$

where $\vec{\boldsymbol{\sigma}}$ denotes the Pauli spin matrices.

5.2 Electronic Properties of Graphene

Experimental studies [46, 47] have shown a remarkably high charge carrier mobility μ in graphene. Specifically, mobilities above $10^5 \frac{V}{cm^2 s}$ [46] at ambient conditions have been recorded in transport measurements in suspended graphene, which are larger than the highest mobilities of many semiconducting materials[46]. This measured value is in agreement with the predicted value assuming charge impurities in the substrate as the main source of scattering. The high-charge carrier mobilities of graphene enable for the observation of the integer quantum Hall effect (IQHE) at room temperatures under real magnetic fields [48, 133]. Graphene also exhibits an anomalous IQHE, where the Hall conductance plateaus occur at

$$\sigma_{xy} = (\pm 4e^2/\hbar)(n + 1/2) \qquad 5.20$$

and are shifted by ½ with respect to the standard Integer Quantum Hall effect sequence[51, 136, 137]. Here $\hbar$ is the Planck's constant divided by 2π, n is the index of the Landau level (LL) and is equal to integer n = …-2,-1,0,1,2,…., and the factor of 4 arises due to double-valley (two inequivalent K points or pseudo-spin) and double-spin degeneracy. Additionally, due to the relativistic nature of the charge carriers of graphene, the energies

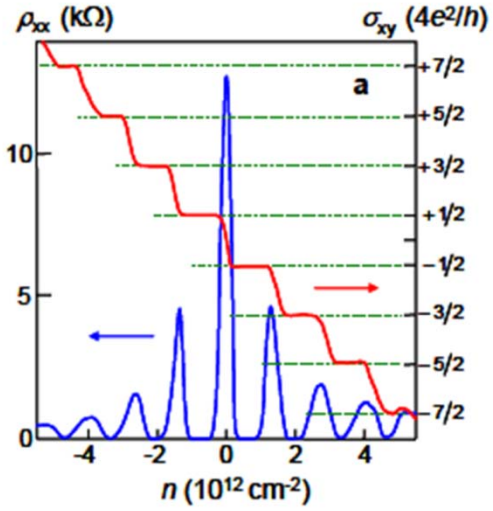

Figure 5.3: Demonstration of the integer quantum Hall effect in graphene on SiO_2. The IQHE is observed as plateaus in σ_{xy} and peaks in the longitudinal conductivity, ρ_{xx} [132].

of the Landau levels in a magnetic field (B) are given by [51, 136, 137]

$$E_n = sgn(n)\sqrt{2e\hbar B|n|} \qquad 5.21$$

instead of the standard $E_n = \pm \hbar\omega_c(n + 1/2)$, where $\omega_c = \frac{eB}{m}$ is the cyclotron frequency. Figure 5.3 demonstrates the IQHE realized experimentally in graphene. The fractional Quantum Hall effect (FQHE) was first observed in 2009 [138] in ultra-clean suspended graphene, supporting the existence of strongly correlated electron states in the presence of a magnetic field.

Graphene also exhibits an ambipolar electric field effect [45], where the concentration of charge carriers can be tuned continuously from electrons to holes by adjusting the gate voltage V_g

$$n_e = (\varepsilon_0\varepsilon/te)\, V_g, \qquad 5.22$$

where ε_0 is the permittivity of free space, ε the permittivity of the substrate, t the thickness, and e the electron charge. For mechanically exfoliated graphene this results in the equation $n_e = 7.2\times10^{-10}\ \mathrm{cm}^{-2}\ \mathrm{V}^{-1}V_g$ if the substrate to graphene is a 300-nm-thick SiO_2 layer on a silicon wafer [46]. The linear dispersion relation in Equation 5.18 results in a linear local density of states.

$$N(E) = \left(\frac{3\sqrt{3}a^2}{\pi}\right)\left(\frac{E}{v_F^2}\right) \qquad 5.23$$

This linear local density of states is expected to give rise to linear tunneling conductance versus bias voltage spectra in STM studies.

5.2.1 Deviation of Electronic Properties

Strain-Induced Vector and Scalar Potentials

The electronic properties described above assume that graphene is a perfect two-dimensional crystal with no disorder. However, the electronic properties of graphene are extremely susceptible to the surrounding environment (particularly the underlying substrate) and to disorder in the crystalline lattice. Examples of disorder that can have an effect on the structure of graphene and on the Dirac fermions are surface ripples, topological defects, vacancies, extended defects including edges, ridgelines, cracks, and charge impurities on the substrate or on top of the graphene itself. The effects of disorder can be generally classified into two types. The first type of disorder can result in a local change in the single-site energy

$$H_{dd} = V_i \sum_i \left(a_i^\dagger a_i + b_i^\dagger b_i\right) \qquad 5.24$$

where V_i is the strength of the disorder potential [65]. The disorder potential acts as a chemical potential shift, which shifts the Dirac point locally[65]. An example of this type of disorder is from charge impurities. A second type of disorder effect arises from changes in the distance or angles between the p_z orbitals. In this case, the hopping energies between different lattice sites are modified, leading to the addition of a new term in the appearance of effective vector, $\vec{\boldsymbol{A}}$, and scalar, Φ, potentials to the Dirac Hamiltonian [65].

$$H_{OD} = \sum_{i,j}\left\{ \delta t_{ij}^{(ab)}\left(a_i^{\dagger} b_j + h.c.\right) + \delta t_{ij}^{(aa)}\left(a_i^{\dagger} a_j + b_i^{\dagger} b_j\right)\right\} \qquad 5.25$$

Where $\delta t_{ij}^{(ab)}$ ($\delta t_{ij}^{(aa)}$) is the change in hopping energy between orbitals on same (different) sublattices [65]. As a consequence, the new spatially varying scalar potential term will result in local charging effects known as selfdoping. The presence of a disorder-induced vector potential $\vec{\boldsymbol{A}}$ in the Hamiltonian indicates an effective magnetic field

$$\vec{\boldsymbol{B}}_S = \left(\frac{c}{ev_F}\right)\boldsymbol{\nabla} \times \vec{\boldsymbol{A}} \qquad 5.26$$

should also be present [65]. (The subscript S denotes the magnetic field induced due to disorder from strain.) This might imply time reversal symmetry is broken although the original problem was time reversal invariant, but in fact this is not the case. Equation 5.25 is for only the Dirac cone at K; the second Dirac cone at K′ is related to the first by time reversal, indicating that the effective magnetic field associated with K' is reversed [65]:

$$-\vec{\boldsymbol{B}}_S = \left(\frac{c}{ev_F}\right)\boldsymbol{\nabla} \times \overrightarrow{\boldsymbol{A}^*}. \qquad 5.27$$

Therefore the global time reversal symmetry is preserved despite the addition of a vector potential, and the new effective magnetic fields are known as pseudomagnetic fields. Distortions of the atomic lattice can give rise to the above disorder effects. As a

consequence a distortion of the graphene lattice should create large, nearly uniform pseudomagnetic fields and give rise to a pseudo-quantum-Hall effect [139]. An elastic strain can be expected to induce a shift in the Dirac point energy from local changes in electron density, and is also predicted to induce an effective vector potential that arises from these changes in the electron-hopping amplitude between carbon atoms [140]. The strong effects of strain open the possibility of tuning the electronic properties of graphene by modifying the mechanical structure of graphene via shear or compression/dilation strain [140] since graphene can be stretched more than 15% and remain intact [141].

The effective vector and scalar potential fields induced by a two-dimensional lattice strain can be derived. If we use the coordinates that are fixed with respect to the honeycomb lattice of graphene in such a way that the *x* axis corresponds to a zigzag direction, we find that the gauge field $\vec{\boldsymbol{A}}$ acting on the charge carriers can be written as [142, 143]

$$A_x = \pm \frac{c\beta}{a}\left(u_{xx} - u_{yy}\right)$$

5.28

$$A_y = \mp \frac{2c\beta}{a}\left(u_{xy}\right)$$

with

$$\beta = \frac{\partial \ln\left(t\right)}{\partial \ln\left(a\right)} \approx 2.$$

Here $\vec{\boldsymbol{A}} = (A_x, A_y)$, a is the carbon-carbon atom separation distance of 0.142 nm, $t \sim$ 3.033 eV is the electron hopping energy between p_z orbitals located at nearest neighbor atoms, c is a numerical constant that depends on the details of atomic displacements within

the lattice unit cell, and u_{ij} is the strain tensor and is related to the two-dimensional displacement field $\vec{\boldsymbol{u}} = (u_x, u_y)$ by the following [144]

$$u_{xx} = \frac{\partial \mathrm{u}_x}{\partial \mathrm{x}} \, , u_{yy} = \frac{\partial \mathrm{u}_y}{\partial \mathrm{y}} \, , u_{xy} = \frac{\partial \mathrm{u}_x}{\partial \mathrm{y}} \, . \qquad 5.29$$

For nontrivial strain that leads to an pseudomagnetic field, $\pm \vec{\boldsymbol{B}}_S = \left(\frac{c}{ev_F}\right) \boldsymbol{\nabla} \times \vec{\boldsymbol{A}}^{(*)}$, the LDOS of Dirac fermions is modified so that LDOS peaks at quantized energies [144]

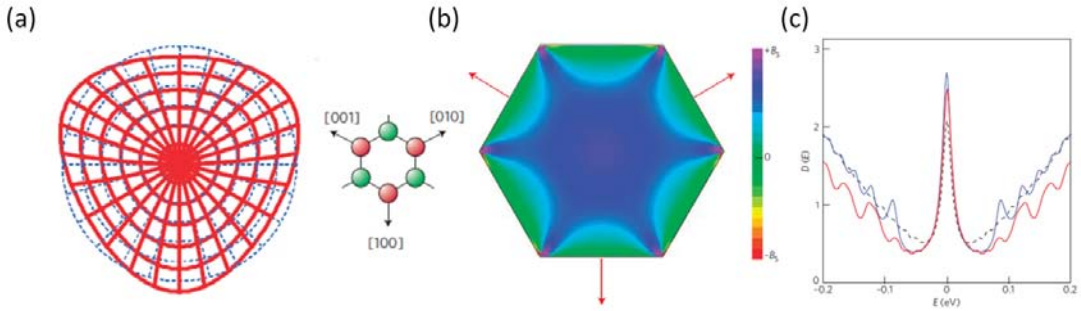

Figure 5.4. Example of a nontrivial strain that gives rise to a vector potential and therefore a pseudomagnetic field. Shown in (c) is the expected density of state resulting from such a strain. Images taken from [139].

$$E_n = sgn(n)\sqrt{2ev_F^2 \hbar B_S |n|} \qquad 5.30$$

in addition to the linear local density of states at low energies from Equation 5.23. A magnetic length may also be defined [139, 152]

$$l_B = \sqrt{\frac{\Phi_0}{2\pi B_S}} \qquad 5.31$$

where Φ_0 is the flux quantum.

These Landau level peaks have been recently observed [140] and are theoretically exemplified in Figure 5.4. In the studies by the Zettl and Crommie group pseudomagnetic fields up to 300 Tesla [140]. Here we note that the strain necessary for inducing a pseudomagnetic field must be *nontrivial* shear strain and that the induced vector potential results in an *out of plane* (perpendicular to the graphene sheet) pseudomagnetic field. Any uniaxial strain would result in a spatially nonvarying vector potential and therefore no pseudomagnetic field. We further emphasize the aforementioned description for strain induced effects assumes noninteracting Dirac fermions in graphene.

If the strain is not purely shear but also contains dilation/compression components, it is theoretically predicted to gives rise to an effective scalar potential

$$V(x,y) = V_0\left(\frac{\partial \mathrm{u}_x}{\partial \mathrm{x}} + \frac{\partial \mathrm{u}_y}{\partial \mathrm{y}}\right) \qquad 5.31$$

where $V_0 = 3\ eV$ is estimated from the linear rise in the work function of graphene under compression [136, 137, 145]. This spatially varying scalar potential will give rise to an effective static charging effect but the charging effect can be largely screened if the height variation of the graphene is much smaller than the magnetic length.

Phonon-Mediated Tunneling

Induced static charging and pseudomagnetic fields are not the only possible effect strain can have on the electronic properties of graphene. Previous scanning tunneling microscopy studies on graphene have produced observed spectra which does not exhibit pure behavior of Dirac-like [146]. It has been predicted that out of plane phonon-mediated inelastic tunneling will also have an effect on the tunneling spectra. This is due to coupling between

the nearly free electron bands at the center of the Brillouin zone and the Dirac fermions in the π bands at K and K′ [147].

According to this scenario, the tunneling DOS from STM spectra is dominated by the DOS of the nearly free electron bands, $N_\Gamma(\omega)$ in graphene. As shown in Chapter 2, the STM tunneling current is determined by the tunneling DOS which is the LDOS at the location of the sample and the tip which is typically within a few angstroms of the sample. For each band, the DOS must be weighted with squared amplitude of the corresponding wave function at the tip-sample separation distance [148]. For graphene the differential conductance can be shown to be [148]

$$\frac{dI}{dV} \approx \Psi_\Gamma^2 N_\Gamma(\omega) + \Psi_K^2 N_\mathrm{K}(\omega) \qquad 5.32$$

where $N_\Gamma(\omega)$ is the density of states and Ψ_Γ is the wave function of the nearly free electron bands while $N_\mathrm{K}(\omega)$ is the density of states and Ψ_K is the wave function of the π bands. As shown in [148] at a tip-sample separation distance of 0.5 nm: $\frac{\Psi_\Gamma}{\Psi_K} \sim 10^4$ which implies that the nearly free electron band will dominate the tunneling DOS.

Wheling et al. [147] developed a model to explain how phonon-mediated tunneling affects scanning tunneling spectroscopy in particular for graphene. The two π bands in graphene give rise to graphene's linear DOS close to the Dirac point and the Dirac fermions at K and K′can be described by the Hamiltonian [147]

$$H_\pi = \sum_{v=\pm,q} v\varepsilon(q)\left(c_v^\dagger c_v\right) \qquad 5.33$$

where v denotes the valence or conduction band and $c_v^\dagger, (c_v)$ represent the creation(annihilation) operator of an electron in this band with momentum q [147]. The

nearly (quasi) free electron bands at Γ have a minimum energy at $E = 3.3\ eV$ and can be approximated by a flat band Hamiltonian

$$H_\sigma = \sum_q d_q^\dagger E_\sigma\, d_q \qquad 5.34$$

where $d_q^\dagger (d_q)$ is the creation (annihilation) operator of an electron in this band with crystal momentum q. Out-of-plane phonons scatter electrons between the π and quasi-free electron bands with the electron-phonon interaction reading as

$$V = \lambda \sum_{v,q,k} \left(d_{k+q}^\dagger c_{v,q} + c_{v,k+q}^\dagger d_q\right)\left(a_k + a_{-k}^\dagger\right) \qquad 5.35$$

where a_k annihilates an out-of-plane phonon carrying crystal momentum k. As stated above, the phonon modes at K and K' will be the most important contributors to inelastic tunneling signals. Around these points, their Hamiltonian can be approximated by $H_{phonon} = \hbar\omega_a \sum_k a_k^\dagger\, a_k$ where $\hbar\omega_a$ being the energy of the out of plane phonons at at K and K′.

The noninteracting electron Green's function is described by [148]

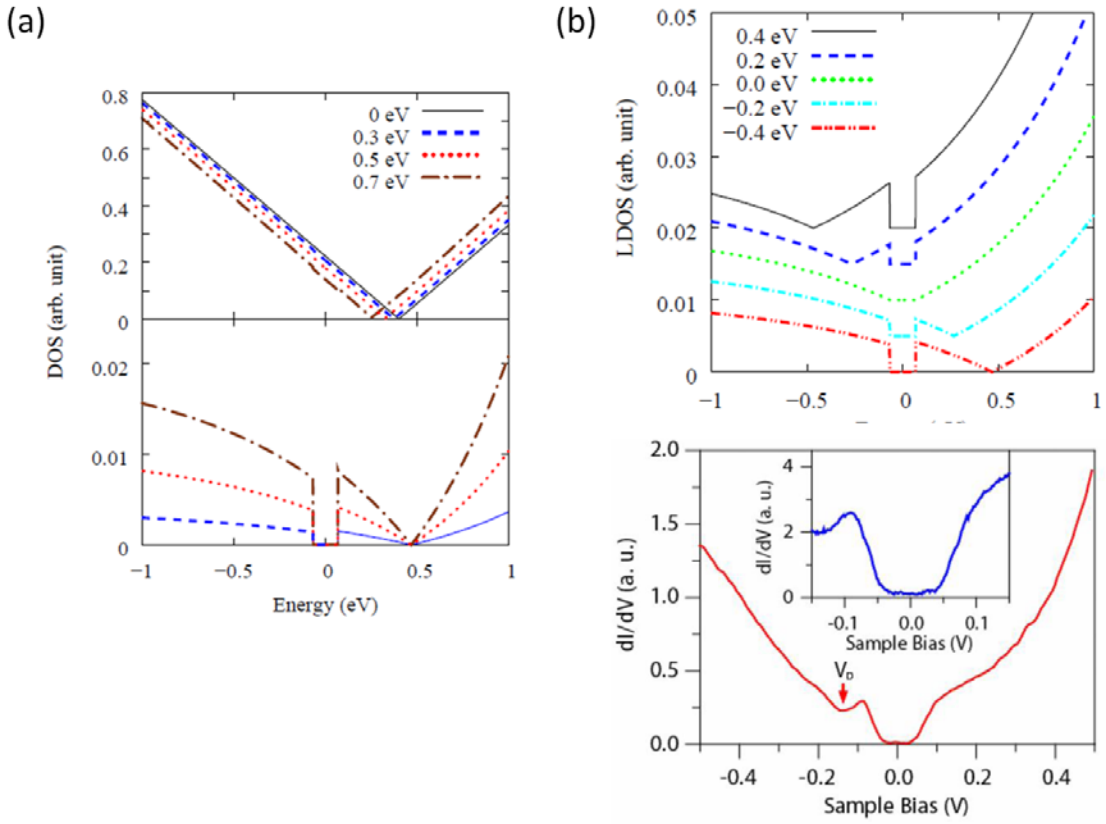

Figure 5.5: Deviation from pure Dirac spectra due to phonon-mediated tunneling. (a) Top panel: Density of states for different coupling states. Bottom panel: Total density of states for the nearly free electron band. (b) Density of states for different chemical potentials. Lower panel: STS spectra demonstrating the band gap due to phonon mediated tunneling. Images from [147] and [146]

$$G^0(q, i\omega_n) = \begin{pmatrix} \frac{1}{i\omega_n - E_\sigma} & 0 & 0 \\ 0 & \frac{1}{i\omega_n - E(k)} & 0 \\ 0 & 0 & \frac{1}{i\omega_n + E(k)} \end{pmatrix} \quad 5.36$$

where ω_n are the fermionic Matsubara frequencies. The noninteracting phonon Green's function is described by $D^0(i\Omega_m) = \frac{2\omega_a}{\Omega_m^2 + \omega_a^2}$ (ω_a is the phonon mode energy) where the electron-phonon interaction from Equation 5.35 transformed to the matrix form of Equation 5.36

$$M_{-} = \begin{pmatrix} 0 & \lambda & 0 \\ \lambda & 0 & 0 \\ 0 & 0 & 0 \end{pmatrix}, M_{+} = \begin{pmatrix} 0 & 0 & \lambda \\ 0 & 0 & 0 \\ \lambda & 0 & 0 \end{pmatrix} \quad 5.37$$

so that the electronic selfenergy can be written as

$$\Sigma(i\omega_n) = \frac{-1}{\beta}\sum_{v,\Omega_m} D^0(i\Omega_m) M_v G^0(r = 0, i\,\omega_n - i\Omega_m) M_v. \quad 5.38$$

The selfenergy is diagonal and for ω small compared to the Dirac energy bandwidth the components are

$$\Sigma_{1,1}(\omega + \mathrm{i}\delta) = \Sigma'_{1,1}(\mathrm{c}) + \mathrm{i}\Sigma''_{1,1}(\omega + \mathrm{i}\delta) \quad 5.39$$

$$\Sigma_{1,1}{}'(\omega + \mathrm{i}\delta) \propto (\omega + \omega_\mathrm{a})\ln\left|\frac{\omega + \omega_\mathrm{a}}{\mathrm{W}}\right| + (\omega - \omega_\mathrm{a})\ln\left|\frac{\omega - \omega_\mathrm{a}}{\mathrm{W}}\right|$$

$$\Sigma_{1,1}{}''(\omega + \mathrm{i}\delta) \propto -\Theta(\omega + \omega_\mathrm{a})|\omega - \mathrm{sgn}(\omega)\omega_\mathrm{a}|$$

Integrating the interacting Green's function $G^{-1} = G^{(0)^{-1}} - \Sigma(\omega)$ over the momentum space gives the total DOS

$$N(\omega) = \frac{-1}{\pi} Tr\left[Im\left(G(r = 0, \omega + \mathrm{i}\delta\,)\right)\right] \quad 5.40$$

At these low energies, the density of states in nearly free electron bands are described by

$$N(\omega) = \frac{-1}{\pi}\frac{\Sigma_{1,1}{}''(\omega+\mathrm{i}\delta)}{\left|\omega - E_\sigma - \Sigma_{1,1}(\omega+\mathrm{i}\delta)\right|^2} \quad 5.41$$

This density of states will vanish for energies less than E_σ if there is no electron-phonon interaction. With the phonon-electron interaction present, for electron energy $\omega > \omega_\mathrm{a}$, where ω_a is the phonon frequency, the nearly free electron bands will mix with the π bands, resulting in a band gap of width ω_a. Outside of this band gap, the density of states of the nearly free electron band will resume to the Dirac behavior of the density of states of the π bands. This theoretical scenario is demonstrated in Figure 5.4. Lattice strain affecting

the out of plane phonons will therefore induce changes in the resulting band gap and consequently the tunneling spectrum of graphene.

5.3 Discusion

In this chapter, we have reviewed the tight binding model and used it to demonstrate that graphene possesses a linear dispersion relationship for energy vs. momentum at the K points and that the charge carriers in graphene are massless Dirac fermions. The effects of strain and disorder have been shown to be able to induce vector and scalar potentials therefore pseudomagnetic fields and charging effects. Evidence of strain-induced vector and scalar potentials will be manifested by charging effects and tunneling conductance peaks at quantized energies, $E_n = sgn(n)\sqrt{2ev_F^2\hbar B_S|n|}$. We have also observed that the scenario of phonon-mediated tunneling will directly affect tunneling conductance studies of graphene by opening up a gap ω_a in the tunneling spectra. These out of plane phonon modes will be susceptible to the effects of lattice strain. In the next chapter, we present STS studies of the effects of strain on the lattice and on the electronic properties of graphene.

Chapter 6

Scanning Tunneling Spectroscopic Studies of Graphene

The electronic properties of graphene are known to be susceptible to disorder and the underlying substrates [139]. In this chapter, we report our findings from spatially resolved scanning tunneling spectroscopic studies of tunneling spectra on graphene that was prepared by different means and on different substrates. Several important results are inferred from these studies. First, we found the presence of low-energy conductance modulations in the density of states that were directly correlated with the strain induced on graphene by the surface roughness of the underlying SiO_2 substrate. Secondly, enormous strain found in chemical vapor deposition (CVD) grown graphene on copper gave rise to an additional vector and scalar potentials in the effective Hamiltonian of graphene, especially near topological defects. Under the strain-induced pseudomagnetic fields the local density of states (LDOS) demonstrated clear evidence of charging effects and tunneling conductance peaks at quantized energies that are consistent with both integer and fractional quantum Hall states. Strain-induced pseudomagnetic fields up to 50 Tesla were observed in these samples. The results presented in this chapter suggest the possibility of using strain engineering for nano-electronic applications.

6.1 Experimental Preparation and Material Consideration in Graphene Studies

Graphene has one of the simplest crystalline structures in nature but was extremely difficult to isolate. Originally predicted to not exist independently [132], it was realized by

the simple method of peeling graphite [45]. Since 2004, other methods of graphene manufacture have arisen such as chemical vapor deposition and thermal decomposition of silicon carbide [153] . The graphene samples studied in this thesis were made by either mechanical exfoliation by collaborators in the C. N. Lau group at the University of California at Riverside or made by CVD growth on Cu foils by Brian Standley or David Boyd at Caltech [154].

The samples that are made by mechanically exfoliation used a SiO_2 substrate. The silicon substrate is prepared by first thermally growing a 300-nm-thick SiO_2 layer on a silicon wafer, followed by gentle sonication of the substrate in acetone and then pure alcohol for about two minutes. The substrate is then baked at 115°C on a hotplate, nitrogen blown dry while cooling down [154]. Finally, a mechanically exfoliated graphene sheet from highly oriented pyrolytic graphite (HOPG) is applied to the prepared substrate. A graphene flake is isolated by repeatedly pealing graphite till several single-layer or multi-layer graphene flakes are finally left over. After mechanical exfoliation, an optical microscope is used to identify the location of single-layer graphene (due to an optical phase shift, single-layer graphene will appear as slightly different color when on 300-nm-thick SiO_2), and photolithographic processes are employed to attach gold electrical contacts to the graphene [154]. Prior to STM measurements, the sample is annealed in a pure oxygen environment at temperatures of 400°C for 15 minutes to remove the photoresist that remained from earlier photolithography processes by using a Hevi-Duty high-temperature oven with an Omega CN2011 temperature controller.

Graphene samples made by mechanical exfoliation are typically smaller than 100 x 100 microns in size. Most are less than 10 x 10 microns in size, which is barely resolvable

to the naked eye. Due to their small size, aligning the STM tip with the graphene flakes is exceeding difficult. In order to provide the needed magnification, an optical microscope is configured and used to align tip and sample with the aid of the X-Y course movement sample stage described in Chapter 2. It was discovered that it was often easier to align the STM tip with the gold leads connecting to the graphene flake than to the graphene flake itself. Extreme care must be taken with this process, otherwise the STM tip will not land on a conductive surface and no tunnel junction can be formed. In the absence of a tunneling junction, the STM tip will crash and possibly damaging the sample itself.

Some of the samples studied in this thesis were made by means of CVD growth, as described in detail in [155]. Specifically, graphene films were primarily grown on 25-μm-thick Cu foils in a furnace consisting of a fused silica tube heated in a split tube furnace. The fused silica tube loaded with Cu foils was first evacuated and then back filled with hydrogen, heated to ~ 1000°C, and maintained under partial hydrogen pressure [155]. A methane gas mixture was then introduced into the tube furnace with a total pressure of 500 mTorr for a set amount of time. Finally, the furnace was cooled to room temperature, and the Cu foils coated with graphene appeared shiner when compared to Cu foils prior to deposition, consistent with previous reports [155]. The graphene sheets prepared by this method if examined with Raman spectroscopic studies are found to be largely single- or double-layered samples [154]. However, STM studies did demonstrate that certain regions are not graphene but amorphous carbon. Samples grown by this method are very large in comparison, up to sizes of 1×1 cm^2, to the samples made by mechanical exfoliation. At this point the sample is cleaned by gentle sonication in ethanol for approximately two minutes and then loaded into the sample holder of the STM. Unfortunately, the Cu foil

under the graphene layer will begin to oxidize immediately, which limits the lifetime of the sample for experimental investigation.

For later experiments, it was desired to transfer the CVD grown graphene from the copper substrate to different substrates. The method for transferring the graphene sample is detailed in [154]. To briefly describe the transfer process, first SiO_2 substrates

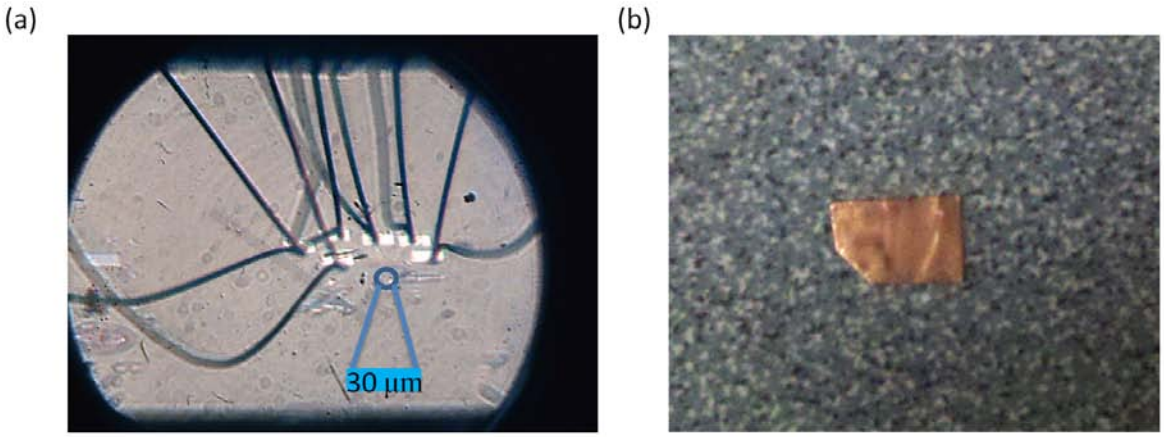

Figure 6.1: Optical images of different graphene samples. (a) Optical microscope image with magnification × 64 of a 10 × 30 micron^2 mechanically exfoliated graphene flake. The graphene flake resides on a 300-nm-thick SiO_2 substrate on a Si wafer. The bright squares are gold pads used to make electrical contact to the graphene flake. In order to perform STS studies of the flake the tip must be perfected aligned over the sample or over the gold electrical contacts and the X-Y course stage used to slowly realign the tip over the sample with repeated scans till the sample is located. (b) CVD grown graphene on Cu foil. The graphene sample is approximately 1 cm × 0.5 cm. The STM tip may be aligned anywhere above the sample.

were prepared by first thermally growing a 290 nm thick SiO_2 layer on a silicon wafer (p-type [100]), followed by gentle sonication of the substrate in acetone and then pure alcohol for about two minutes [154]. The substrate was then baked at 115°C on a hotplate and nitrogen blown dry while it was cooled down. Next, a layer of PMMA was deposited on top of the CVD grown graphene on the copper foil as scaffolding, and then the copper

substrate was removed with nitric acid [154]. The PMMA/graphene sample was subsequently placed on a SiO2 substrate with the graphene side down. Finally, the PMMA was removed with acetone [154]. The transferred graphene was cleaned and annealed in an argon atmosphere at 400°C for 30 minutes. Electrodes were created by thermally evaporating 2.5 nm chromium and 37.5nm gold through an aluminum foil shadow mask [155]. The sample then was rinsed again gently with acetone followed by ethanol. The sample is then loaded into the STM. Figure 6.1 shows two graphene samples prepared by two different methods. The sample shown in Figure 6.1(a) was made by mechanical exfoliation and then placed on SiO2. Electrical contacts were made to the graphene flake for electrical transport measurements and STM studies. The sample shown in Figure 6.1(b) was a mono-layer graphene grown on a copper foil by means of CVD.

. After loading the sample to the STM probe, the STM assembly was pumped down to pressures $<10^{-6}$ Torr and the graphene samples were investigated both topologically and spectroscopically. Initially each sample was studied at 300 K and then at 77 K while at zero magnetic fields. As described in Chapter 2, measurements were conducted in a 128 ×128 pixel grid where both topography and I(V) vs. V spectroscopy were recorded with a tunnel junction of 1.5 GΩ. From the I(V) vs. V curves the differential conductance and the corresponding LDOS was measured.

6.2 Studies of Mechanically Exfoliated Graphene on SiO_2 Substrate

In this section we present data obtained from STS studies of mechanically exfoliated graphene on SiO_2 substrates. Numerous topographic measurements were performed across multiple regions of a sample and measurements found numerous surface corrugations across the sample. The graphene sample was not perfectly flat but possessed a distinctly three-dimensional component. These corrugations were up to 0.5 nm in height over lateral distances of 10 nm over scan areas of 2.2 nm × 5.0 nm. Scans over larger regions resulted in similar height variations. These corrugations were verified with measurements taken with atomic force microscopy over the same area, showing height corrugations of ±1.0 nm over the same lateral distance. These findings were in good agreement with results reported previously in [58, 156, 157]. Demonstrations of these corrugations are shown in Figure 6.2. The graphene sample was found to be free of crystalline defects. The origin of these topographic corrugations was investigated and found to be the result of the graphene sample overlaying the uneven surface of a SiO_2 substrate. Atomic force microscopy studies of the silicon substrate demonstrated an average surface roughness of ± 2.0 nm over a region of 8.6 nm × 8.6 nm region. The possibility of the surface corrugations resulting from the proximity of the gold electrical leads (see Figure 6.1(a)) was also investigated. The average height variations of the surface corrugations were found to be independent of the distance from the gold electrical leads.

Spatial spectroscopic studies were also carried out across the graphene sample. Numerous modulations were found in the tunneling conductance. The tunneling spectra

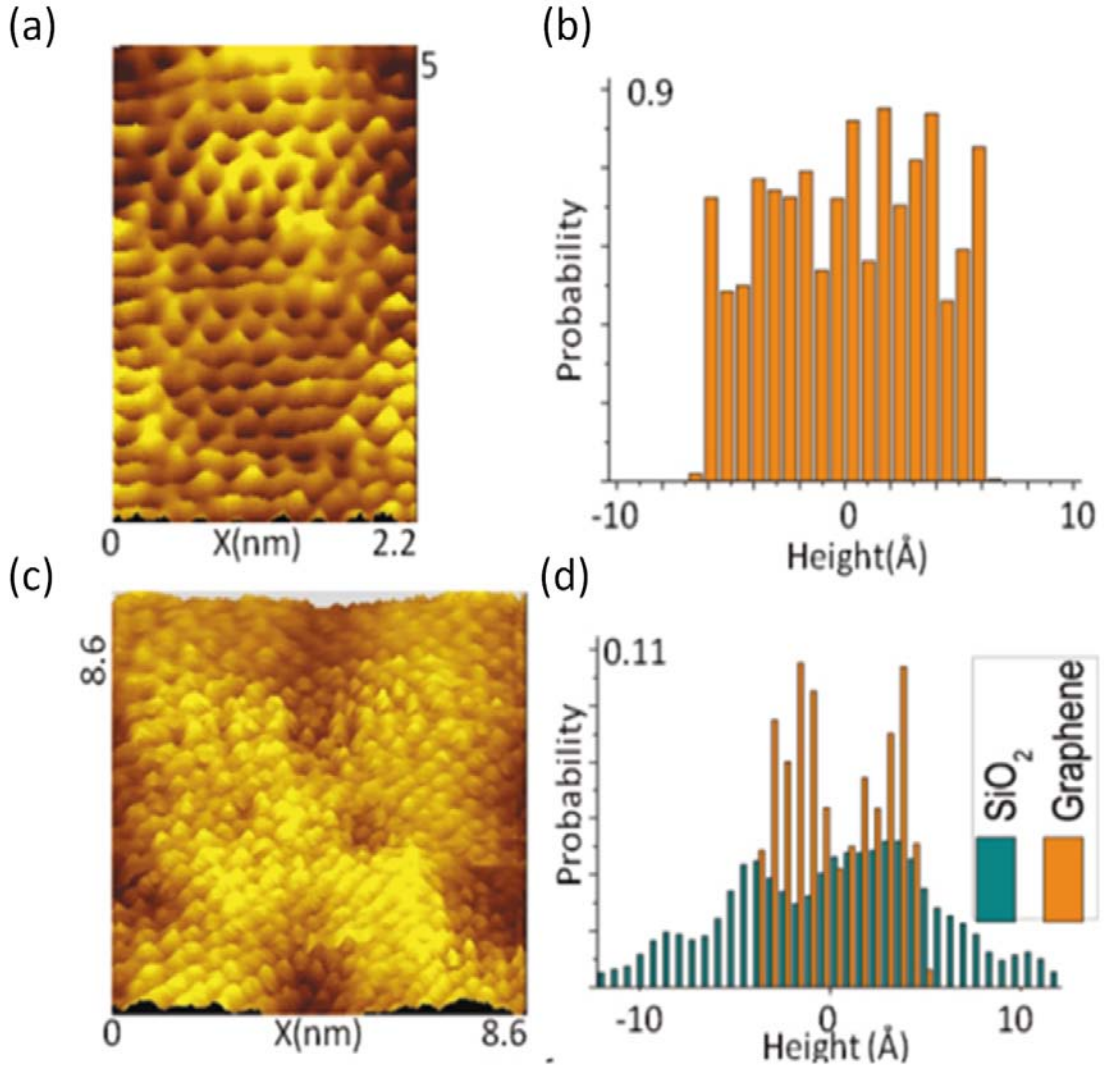

Figure 6.2: Surface corrugations of graphene crystal. (a) Topographic STM image of a 2.2 nm × 5.0 nm showing distinct ripples (height variations) in the graphene. (b) Histogram of the height variations of the image in (a) showing ±0.5 average surface roughness. (c) Larger topographic STM image over a 8.6 nm × 8.6 nm region. (d) Histogram of the height variations of the scan in (c) and compared with AFM surface roughness measurements of the bare SiO_2 substrate. The two histograms indicate a strong correlation between corrugations in graphene sample and the underlying surface roughness of the substrate.

(determined at each pixel) varies spatially from V-shaped spectra to parabolic U-shaped spectra across the conductance maps. These variations in the tunneling spectra were found to weaken at higher energies with the tunneling conductance becoming more uniform. Conductance modulations typically were limited in effect to lower energies and appeared to be correlated with topography corrugations. Figure 6.3 shows several conductance maps taken at various constant energies, demonstrating strong spatial variations in conductance. In contrast, the Dirac voltage, V_D, determined at each pixel, appears relatively homogenous spatially and not correlated to topography. This is in contrast to the conductance modulations where the spatial map of tunneling conductance at $V_{Bias} = (V - V_D) = 0$, reveals strong correlation with the topography. As V_{Bias} increases, the spatial variations in conductance across the sample decrease steadily, as exemplified by Figure 6.3 for $V_{Bias} = 80$ meV and for $V_{Bias} = 240$ meV. The changes in the Dirac voltage are most likely due to charge impurities on the underlying SiO_2 substrate, which suggests that the spatial conductance modulations at constant bias voltages are not due to charge impurities.

To compare the correlation between spatial corrugations and conductance modulations, the lattice distortions must be quantified. A fast Fourier transformation (FFT) algorithm was performed over the topography previously discussed and shown in Figure 6.2 and exhibited in Figure 6.4. The FFT scan revealed a distorted hexagon, signifying a major distortion in the lattice structure. With a distorted lattice one can calculate the resulting local

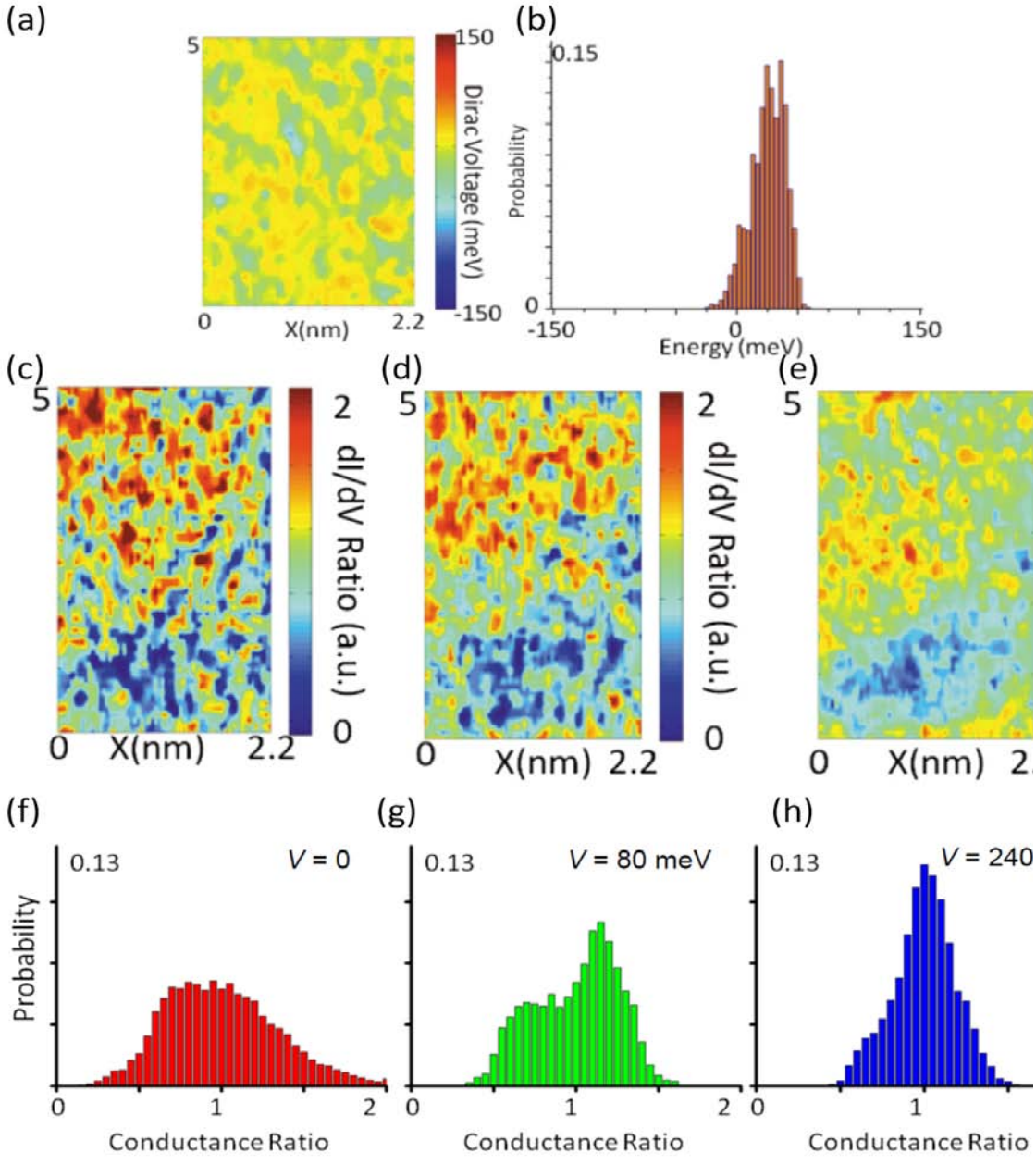

Figure 6.3: Conductance modulations in graphene. (a) A Dirac energy map compiled by determining the Dirac point, which was obtained by locating the minimum conductance of each spectra at each pixel of the same region as Figure 6.2a. The Dirac energy is fairly uniform across the scan. (b) Histogram of all values of the Dirac energy in (a). (c)–(e) Tunneling conductance maps at bias voltages 0, 80, and 240 meV. Tunneling conductance The tunneling conductance ratio becomes more uniform as bias energy increases. (f)–(h) Histograms of the tunneling conductance in (c)–(e). As bias voltage increases each histogram narrows in width.

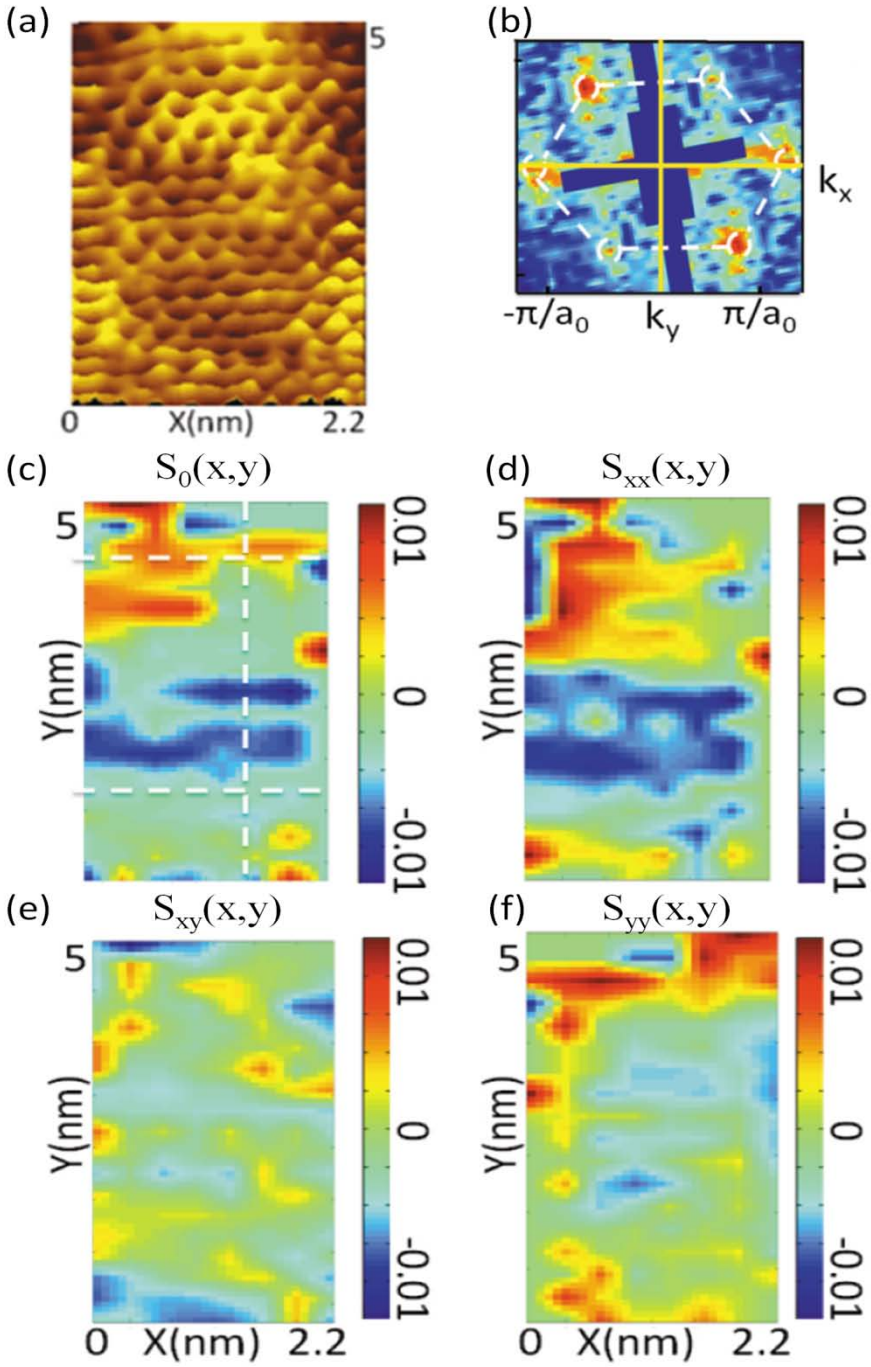

Figure 6.4: Strain tensor images: (a) Topographic image of a mechanically exfoliated graphene sample. (b) FFT image of the topography in (a) showing a distorted hexagonal reciprocal lattice. (c) Scalar strain field S_0 showing strong correlation with topography and tunneling conductance. (d) Map of the strain tensor component S_{xx} (e) Map of the strain tensor component S_{xy} (f) Map of the strain tensor component S_{yy}

displacement field, $\vec{\mathbf{u}}$, and therefore the resulting strain tensor. We define $\vec{\mathbf{u}} = < u_x, u_y >$ as the difference of the local lattice vectors from the equilibrium lattice vectors. Following the equation 5.29 we can define the strain tensor components as $S_{xx} = \frac{\partial \mathrm{u}_x}{\partial \mathrm{x}}$, $S_{yy} = \frac{\partial \mathrm{u}_y}{\partial \mathrm{y}}$, $S_{xy} = S_{yx} = (\frac{1}{2})(\frac{\partial \mathrm{u}_x}{\partial \mathrm{y}} + \frac{\partial \mathrm{u}_y}{\partial \mathrm{x}})^2$ as well as a scalar strain field $S_0 = \left|\frac{\vec{u}(x,y)}{a_0}\right|$. The resulting strain tensor maps are plotted in Figure 6.4. It is easily noticed that there is a strong correlation between the strain tensors and the spatial conductance modulations at a constant voltages. The upper regions of the graphene sample are relaxed while the lower regions of the sample are highly strained. It should be noted that regions of low strain result in V-shaped spectra while highly strained regions exhibit U-shaped spectra.

We quantify possible correlations between the spatial modulations of tunneling conductance and the local strain by considering the correlation function $C(\vec{\mathbf{r}})$:

$$C(\vec{\mathbf{R}}) = \frac{\int d^2r\,[f(r) - \langle f \rangle][g(r-R) - \langle g \rangle]}{\sqrt{A_{ff}(0)A_{gg}(0)}} \qquad 6.1$$

where f(r) and g(r) represent the conductance and strain at position $\vec{\mathbf{r}}$, $\langle f \rangle$ and $\langle g \rangle$, are the mean values over the sample area, and A_{ff} and A_{gg} denotes the auto correlation function of the conductance and strain, respectively. A_{ff} and A_{gg} are given by

$$A_{ff}(\vec{\mathbf{R}}) = \int d^2r\,[f(\vec{\boldsymbol{r}}) - < f >][g(\vec{\boldsymbol{r}} + \vec{\boldsymbol{R}}) - < g >]. \qquad 6.2$$

If we calculate $C(\vec{\mathbf{R}})$ for the conductance map at V_{Bias} = 0 meV and the scalar strain map we find a correlation function value of ~0.44, and at higher energies V_{Bias} = 240 meV we find a correlation function value of ~ 0.12. This demonstrates that the strain effects are stronger at

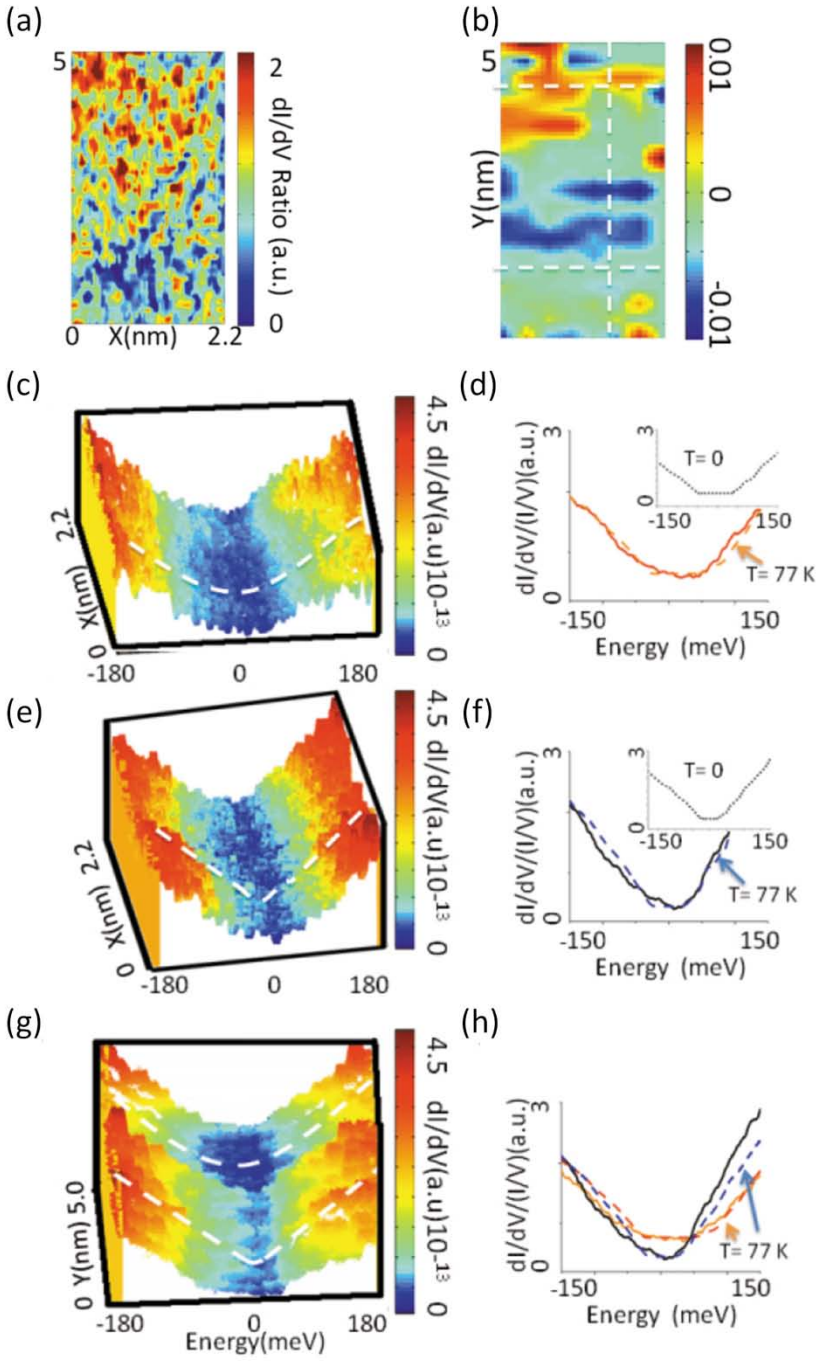

Figure 6.5: Correlation of tunneling spectral characteristics with strain tensor. (a)–(b) Conductance image and scalar strain S_0 showing good agreement. (c) Lower horizontal linecut of tunneling spectra showing mostly U-shaped features in strained graphene. (d)

Theoretical fit of phonon-mediated tunneling to a representative spectra in (c) with an out of plane phonon frequency $\omega_a = 44$ meV. (e)–(f) Upper horizontal linecut of tunneling spectra showing mostly V-shaped features and it resulting theoretical fit $\omega_a = 26$ meV in relaxed graphene. (g)–(h) Vertical linecut of tunneling spectra showing evolution of the tunneling spectra from relaxed to strained regions and the two resulting theoretical fits using phonon frequencies $\omega_a = 24,\ 41$ meV.

lower energies and are much reduced at higher energies where the conductance spatial modulations are reduced.

When we further compared tunneling spectra to strain tensor components along three different linecuts as demonstrated in Figure 6.5. The horizontal linecuts along the upper and lower sections and the vertical linecut which are indicated by dashed lines in Figure 6.5. The spatial evolution of the spectra from the upper line are mostly parabolic

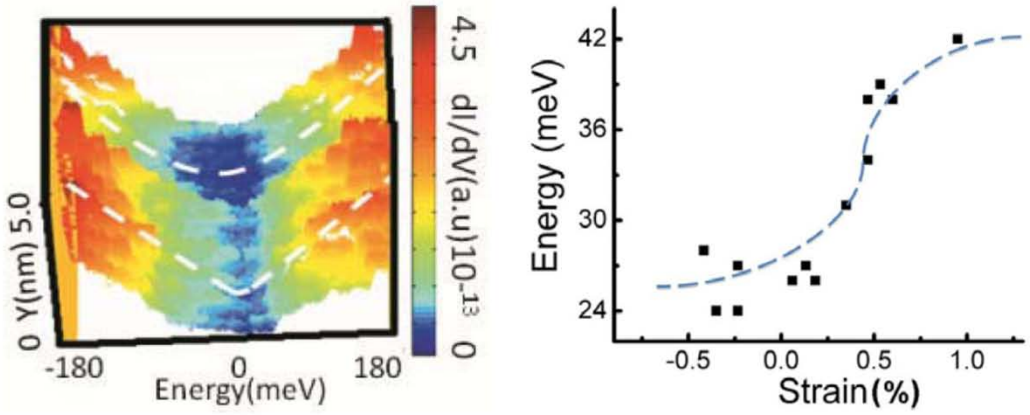

Figure 6.6: Strain vs. phonon frequency: Left panel: Spatially varying tunneling conductance (*dI*/*dV*) *vs.* energy spectra along a line across the graphene sample. The "U"-like spectra correspond to regions of more strained graphene, whereas the "V"-like spectra more generic to the ideal graphene behavior are seen in regions of more relaxed graphene. Right Panel: Energy gap vs. strain magnitude. Energy gap increases as the strain magnitude increases. The tunneling energy gap calculated by fitting each spectra using the model of phonon assisted tunneling. The energy gap corresponds to the effective out-of-plane phonon energy involved in the electron tunneling process.

(U-shaped) around $V_B = 0$, while the lower line cut exhibits mostly Dirac-like (V-shaped) around $V_B=0$. The spatial distribution of the upper line U-shaped spectra correlates well with the region of the graphene sample that is highly strained.

If we follow the argument suggested in Chapter 5 for the scenario of phonon-mediated inelastic tunneling we can fit the different tunneling spectra for each region. In this analysis, which was detailed in Chapter 5, we assume the out of plane phonon frequency ω_a as a fitting parameter, and also allow a small constant zero-bias offset in equation 5.42, which may be attributed to enhanced LDOS due to impurities according to [78, 149]. For T = 77 K, we replace ω by $i\omega_n$ and sum over the fermion Matsubara frequencies ω_n with a prefactor $(1/\beta)$ where $\beta^{-1} = 77$ K. Given that the thermal energy at 77 K is much smaller than $\hbar\omega_a$, however, the thermal smearing effect is insignificant. These fittings are detailed in Figure 6.5 and we observe that the fittings agree reasonably well. Regions of the sample that are highly strained are fit best with a phonon frequency of $\omega_a = 44\ \text{meV}$ while lower, relaxed regions of the graphene sample are best fit with phonon frequencies of $\omega_a = 26\ \text{meV}$. The correlation of spectral characteristics with the strain maps suggests that strain and phonon-mediated inelastic tunneling are a primary cause for the spatial spectral deviations from Dirac behavior in graphene. If we plot the fitted phonon frequency ω_a vs. strain as in Figure 6.6 we find that as strain increases across the sample the resulting phonon frequency increases monotonically. We also note that the ω_a values derived from phonon-mediated tunneling scenario vary significantly across the sample as well as across substrates. In the case of graphene grown on SiC [158],

gap values in the tunneling spectra are much larger (~ 100 meV) than the values derived here.

6.3 Studies on CVD Grown Graphene on Cu and SiO_2 Substrates

In this section we present data obtained from STS studies on CVD grown graphene on Cu foils and from CVD grown graphene that has been transferred to SiO_2 substrates. We find that the lattice distortions and strain effects are much larger on CVD grown graphene than on mechanically exfoliated graphene. The structures of these samples are highly distorted. Consequently the strain from such lattice distortions is large enough to induce pseudomagnetic fields. Samples in both cases were prepared as described in Section 6.1.

6.3.1 Topographic Studies

Initial topographic STM studies on CVD grown graphene on Cu foils revealed two distinct types surfaces: an atomically resolved but highly distorted surface and completely disordered regions without atomic resolution that are mainly amorphous carbon. Large-scale topographic scan reveal a highly rippled sample surface. The height variations of the sample relative to the previous mechanically exfoliated graphene sample are much larger. Height corrugations on an area of 3 nm × 3 nm are ± 5.0 nm and in comparison to the mechanically exfoliated sample where height variations are ±0.5 nm on an equivalently sized sample. Figure 6.7 shows histograms of the height variations on one CVD sample over varying areas. Close inspections of the height variations reveal two types of distortions. The long-wavelength, ripple-like height variations over most of the sample are

correlated with the surface corrugations of the underlying Cu foils, with details to be elaborated later. In contrast, the short wavelength (~ nanoscale) height variations are resultant from the large difference in the thermal expansion coefficients of graphene and Cu. That is, upon cooling the sample from ~ 1000°C to room temperature after the CVD growth of graphene, the graphene expands due to its negative coefficient of thermal expansion and the copper substrate contracts. Consequently the graphene can no longer remain flat and must ripple and buckle, thereby introducing massive lattice distortion and disorder. In Figure 6.7 we observe these ripples over different size topography scans of the sample and plot the according height roughness histograms. These histograms reinforce that the CVD grown graphene is far more corrugated than mechanically exfoliated graphene.

In Figure 6.8 we plot a 3 nm × 3 nm region of the graphene sample and we notice a strong ridgeline along the top of the topography scan. Above this ridgeline in a region we dub the "α" region of the sample, we have a relaxed and very graphene-like lattice structure with a clearly defined honey-comb, hexagonal lattice. Below the ridgeline we have the "β" region of the sample showing an almost "square lattice" or nearly disordered atomic structure. An FFT scan of the topography (as shown in Figure 6.8) clearly shows a highly distorted reciprocal hexagon lattice as well as a distorted square lattice. If we plot the a line

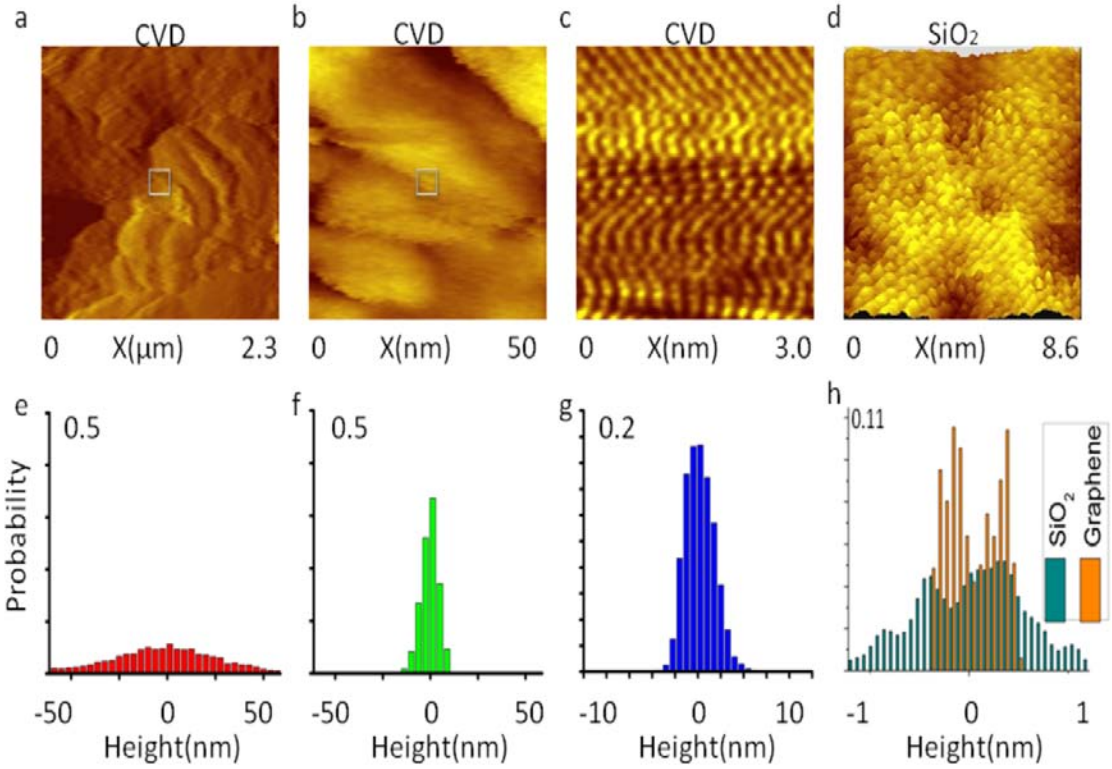

Figure 6.7: Topographic images of CVD grown graphene on Cu: (a) 2.3 μm2.3 ^{2} topography image. (b) 50 × 50 nm^2 topography image. (c) 50 × 50 nm^2 topography image. (d) 2.2 × 5.0 nm^2 topography image but of graphene on SiO_2. (e)–(f) The corresponding histograms of the height variations for each topography scan. The CVD grown graphene on Cu contains numerous ripples and buckling when compared to the "relatively flat" graphene on SiO_2. The surface roughness is factor of ten greater for comparably sized scans.

-cut of the topography across the sample from top to bottom as shown in Figure 6.9, we observe strong height variations (short wavelength changes) along the ridgeline and smaller height variations on a longer distance scale (longer wavelengths). We can estimate the averaged variation in height (Δz) over a length scale L for both wavelengths. For the significant short wavelengths, the height variations $\Delta z \sim 1.0$ nm, this results in a $\Delta z/L \sim 0.3$ which suggests significant strain. The longer-length height variations were investigated and believed to be due to the original

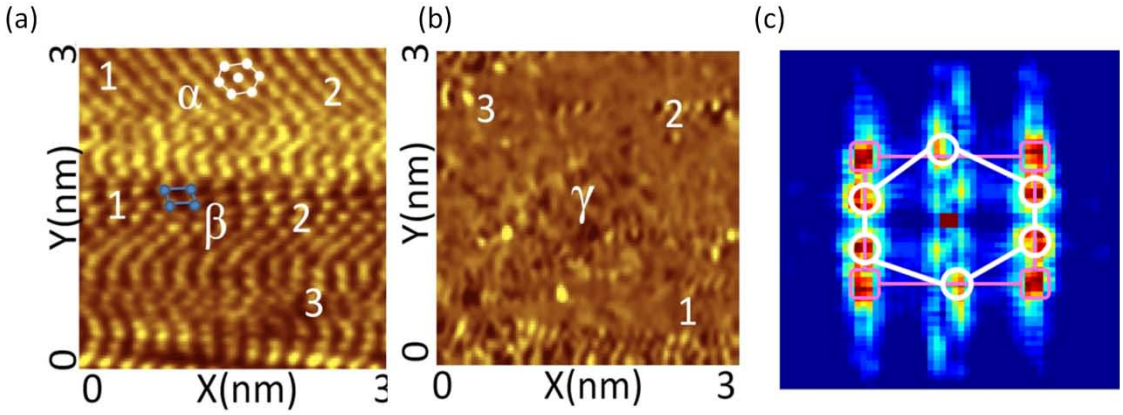

Figure 6.8 Distorted lattice of CVD grown graphene: (a) Topographic map of CVD grown graphene with different "α" and "β" regions identified. (b) Topographic map of a typical amorphous region of CVD grown graphene. There is no discernible atomic structure and may be due to deposition on top of defects on the Cu foil. (c) FFT image of (a) showing both a distorted hexagonal reciprocal lattice and a square reciprocal lattice

surface roughness of the copper foils, as shown in Figure 6.9. Atomic force microscopy performed by David Boyd on an Cu foil with no graphene (taken through all the same procedures but with no graphene actually grown on the Cu foil) suggest long wavelength height variations of $\Delta z/L \sim 0.01$. This confirms that the long wavelength variations (Δz) are due to the underlying morphology of the Cu foil.

The amorphous regions (as exemplified by a 3 nm × 3 nm scan in Figure 6.8) of the CVD grown graphene, plotted in Figure 6.8, show no distinct atomic structure and are defined as "γ" region. This disordered region, we believe to be amorphous carbon that did not grown into a hexagon lattice and may be the deposition of carbon on the defect features on the Cu foils (the bright features shown in the AFM images in Figure 6.9).

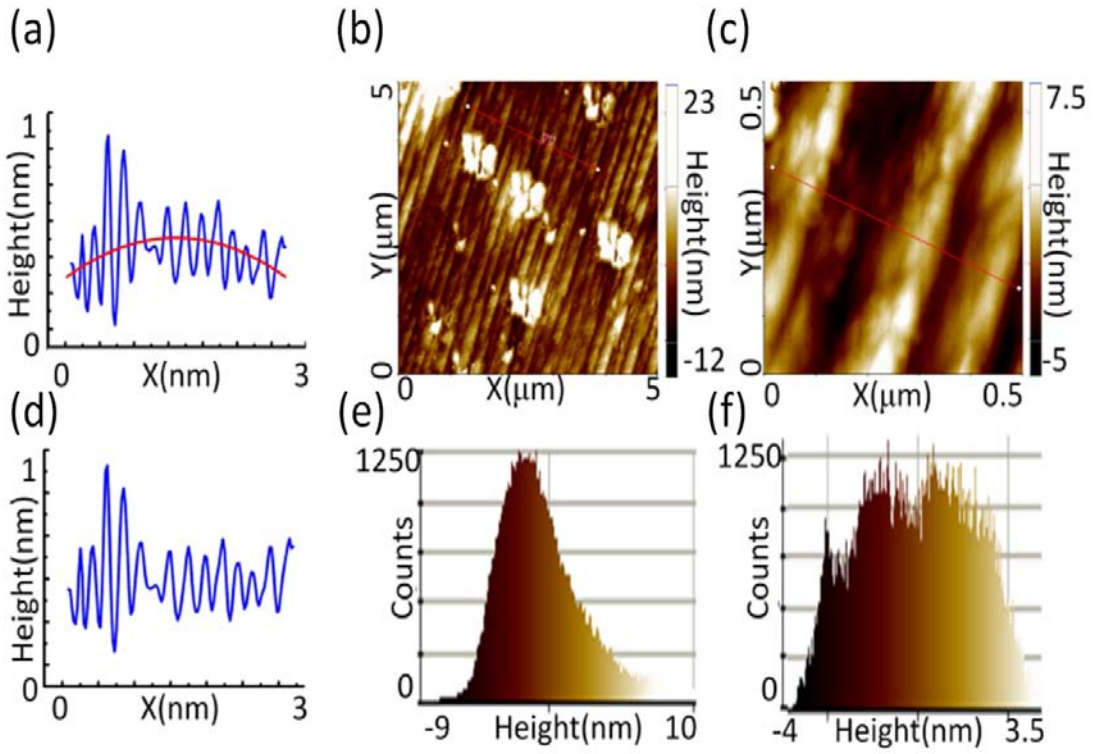

Figure 6.9 Surface roughness of the Cu substrate in CVD grown graphene: (a) vertical linecut of the topography in Figure 6.8(a), showing strong height variations along the horizontal ridgeline as well as a longer wavelength height variations that is due to the surface roughness of the underlying Cu foil. (b)–(c) AFM images of the Cu foil on 5.0 x 5.0 μm^2 area and a 0.5 x 0.5 μm^2 area. (d) The linecut in (a) with the long wavelength height variation subtracted out to give accurate height variations of the ridgeline alone of 0.3–0.6 nm. (e)-(f) Histograms of the surface roughness of the Cu foil for regions in (b), (c). Images (b), (c), (e), (f) courtesy of David Boyd.

6.3.2 Spectroscopic Studies and Pseudomagnetic Fields

To investigate how electronic properties and local density of states were affected by such large lattice distortions, multiple spectroscopy scans were completed over several samples. In particular we compared the normalized tunneling conductance spectra as

detailed in Chapter 2, $\left({}^{dI}/_{dV}\right)/\left({}^{I}/_{V}\right)$ vs. V, from different region with differing lattice arrangements. The spectra for the more honeycombed (relaxed) "α" region of the graphene sample resembled the spectra found in mechanically exfoliated graphene and are Dirac-like (V-shaped) except a substantially larger zero bias conductance and an addition of several weak conductance peaks. In contrast, the typical spectra associated with the square lattice (strongly strained) "β" region appeared to be asymmetric relative to those in the "α" region, with sharp conductance peaks more closely spaced. For "α" and "β" regions and the representative spectra found in each region, the energy interval between consecutive conductance peaks appears to decrease with increasing energy. For disordered, amorphous "γ" regions without atomic resolution, almost completely parabolic spectra that deviates fundamentally from the linear energy dependence of the Dirac fermions was found. While the "γ" region spectra does also demonstrate conductance peaks, the conductance peaks seem randomly spaced. Figure 6.10 shows topography images of each region type and the representative spectra for each region. Figure 6.11 shows similar results achieved and verified on a second graphene sample prepared exactly as the first. The spatial variations in the spectra (tunneling conductance) depends very sensitively on the local strain of the lattice.

If we follow the argument suggested in Chapter 5 for graphene with nontrivial strain, we expect to observe the effects of strain-induced vector and scalar potentials in the tunneling spectra for these highly distorted graphene samples. From Equations 5.26 and 5.28, we expect to see pseudomagnetic fields and a significant charging effect. Particularly we should observe the appearance of LDOS peaks at quantized energies according to

Equation 5.30, $E_n = sgn(n)\sqrt{2ev_F^2\hbar B_S|n|}$, in addition to the linear local density of states at low energies from Equation 5.23. Previous studies [141] on graphene nanobubbles on Pt, observed strong Landau levels from giant strain-induced pseudomagnetic fields of up to B = 300 Tesla. Following a similar method, we subtract off a parabolic conductance background associated with the copper contribution to the tunneling conductance (indicated by the dashed lines in Figure 6.10) and plot the resulting conductance against ($E - E_{Dirac}$). The resulting plots are shown in Figure 6.10. Similar results are shown for a second graphene sample in Figure 6.11.

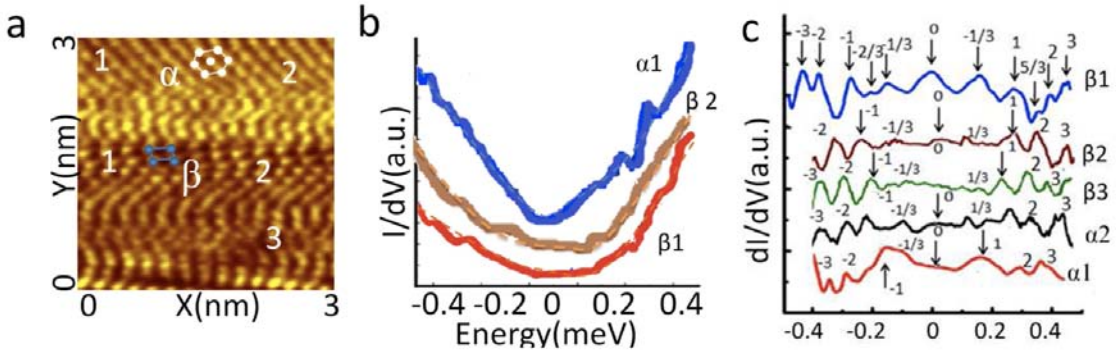

Figure 6.10: Tunneling spectra for CVD grown graphene: (a) Topographic image of CVD grown graphene with "α" and "β" spectra locations identified. (b) Representative tunneling spectra for various regions in (a). "α" spectra exhibit more Dirac-like spectra are in relaxed regions of the sample and "β" spectra exhibit more U-shaped features and are in more strain areas of the sample. Also plotted are the parabolic backgrounds subtracted from the spectra to reveal the quantized Landau levels. (c) Tunneling conductance for various regions of the sample. Each spectra was fit with a parabolic background which was then subtracted. The resulting tunneling conductance displays very distinct quantized conductance peaks associated with Landau levels n = 0, ± 1/3, ± 2/3, ± 5/3, ± 1, ± 2 and ± 3. Notice not all spectra contain the n = 0 peak and is explained by local spontaneous time-reversal symmetry breaking.

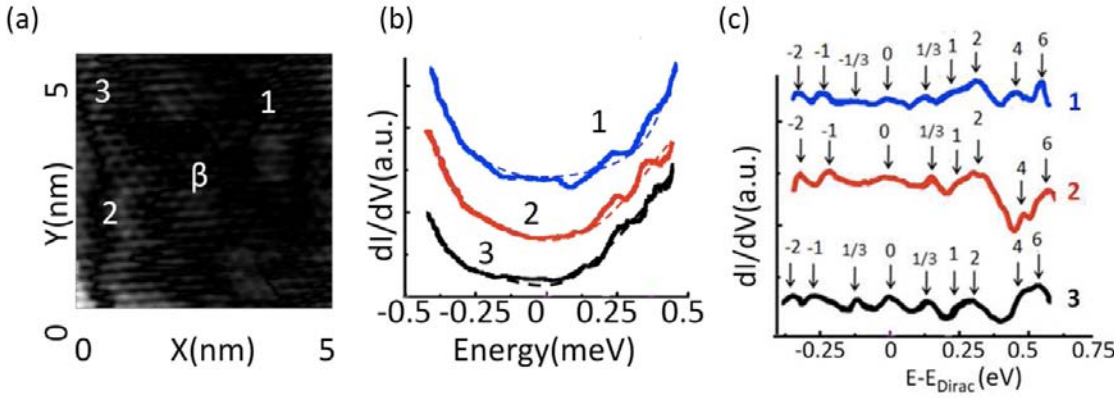

Figure 6.11: Tunneling spectra for a different CVD grown graphene from Figure 6.10: (a) Topographic image of CVD grown graphene with "β" spectra locations identified. (b) Representative tunneling spectra for various regions in (a). Also plotted are the parabolic backgrounds subtracted from the spectra to reveal the quantized conductance peaks. (c) Tunneling conductance for various regions of the sample. Each spectra displays very distinct quantized conductance peaks associated with Landau levels n = 0, ± 1/3, ± 1, ± 2, 4 and 6.

After background subtraction, we find distinct peaks in the LDOS as expected occurring at energies proportional to $\sqrt{|n|}$ for n = 0, ± 1, ± 2, and ± 3 as can be seen in Figure 6.10. If we plot E − E_{Dirac} (eV) vs. $\sqrt{|n|}$ as shown in Figure 6.12, we can determine the strength of the resulting pseudo-magnetic fields for Equation 5.30 and taking $v_F = 10^6$ m/s and find that B_S= 29 ± 8 Tesla for "α" regions and B_S = 50 ± 5 Tesla for "β" regions. The second graphene sample in highly rippled regions exhibited pseudomagnetic fields of B=35 ± 5 Tesla. Furthermore, according to Equation 5.31, $l_B = \sqrt{\frac{\Phi_0}{2\pi B_S}}$, we can specify a magnetic length associated with the pseudomagnetic fields and find it to range from 3.5 nm to 5.5 nm. In stark contrast the amorphous "γ" regions exhibit spectra that is largely smooth and parabolic differing fundamentally from the expected Dirac-like spectra. After subtraction of a parabolic background, the resulting conductance shows no significant

peaks corresponding to Landau levels. This is to be expected for regions with no discernible lattice and is demonstrated in Figure 6.14.

One notable feature observed in the tunneling conductance with the parabolic background subtracted (Figure 6.10 and Figure 6.11) is the appearance of peaks that seem to correspond with fractional Landau levels of n = ± 1/3, ± 2/3, and ± 5/3. These peaks seem to occur in the stronger strained "β" regions. The occurrence of fractionally filled Landau levels is not expected if we follow the arguments presented in Chapter 5 for strain-induced pseudofields, a noninteracting 2-D gas of Dirac fermions. The presence of fractional quantum Hall states due to a pseudomagnetic field may be understood by the following consideration [159]. For CVD grown graphene on Cu, the 2-D electron gas associated with the surface state of Cu substrates provides an additional channel for short-range charge interaction through the electrostatic coupling between the Dirac fermions in graphene and the 2-D electron gas in Cu [159]. Although long-range Coulomb interactions of Dirac fermions are screened by the underlying 2-D electron gas, whether short-range Coulomb interactions may be neglected depends on the strength of the on-site Coulomb potential *U* relative to the nearest neighbor hopping constant "t" [159]. That is, if we consider a modified Hamiltonian from Equation 5.16:

$$H = -t\sum_{\langle i,j\rangle,\sigma}\left(a^{\dagger}_{\sigma,i}b_{\sigma,j} + a_{\sigma,i}b^{\dagger}_{\sigma,j}\right) + U\sum_i n_{i,\uparrow}, n_{i,\downarrow} \qquad 6.3$$

where $a^{\dagger}_{\sigma,i}(a_{\sigma,i})$ and $b^{\dagger}_{\sigma,j}(b_{\sigma,j})$ are the creation (annihilation) operators for an electron with spin σ on sites "i" and "j" of sublattices A and B respectfully. Here "t" denotes the nearest neighbor hopping energy for hopping between different sublattices and $n_{i,\uparrow}, n_{i,\downarrow}$ represent

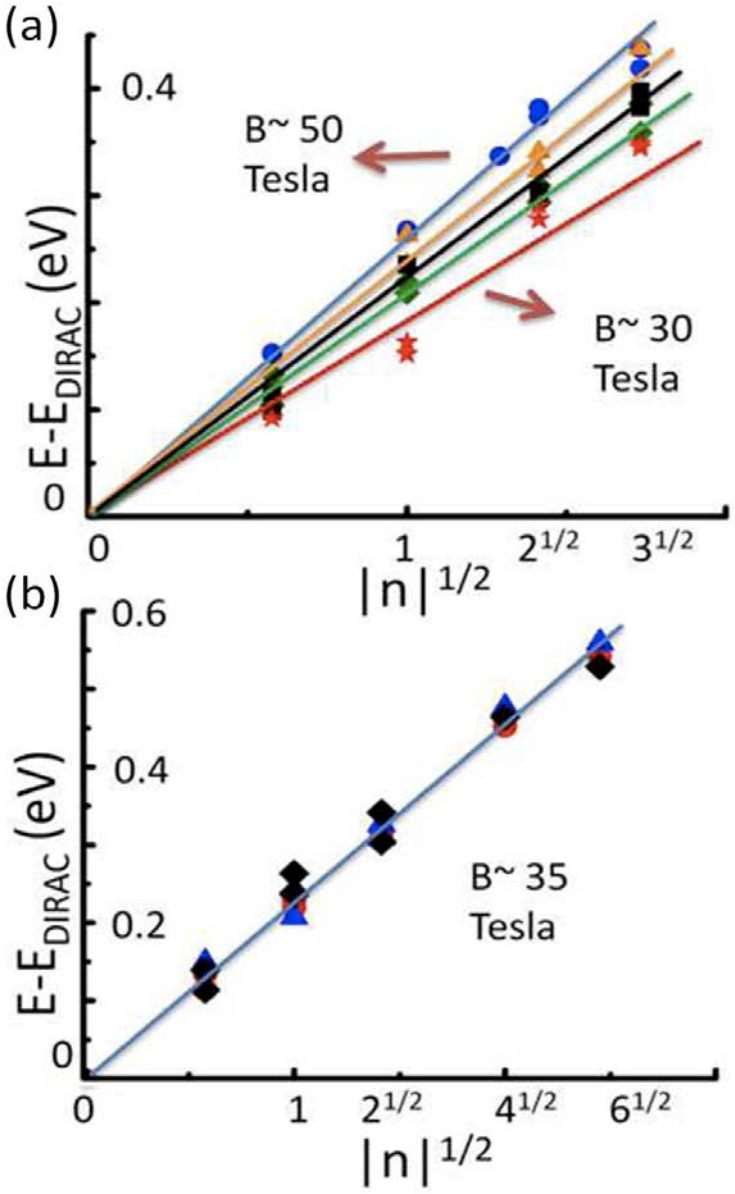

Figure 6.12: (a) Determination of the pseudomagnetic field strength (from data in Figure 6.10): ($E - E_{Dirac}$)(eV) vs. $\sqrt{|n|}$ for a number of spectra taken in the "α" and "β" regions. Most data points lie on a straight line whose slope is proportional to the pseudomagnetic field B_S. The values range from B_S ~ 30 Tesla for most point spectra in the "α" region to B_S ~ 50 Tesla for the strongest strained areas in the "β" region. (b) Determination of the the pseudomagnetic field strength for a second sample (shown in Figure 6.11) with B_S ~ 35 Tesla

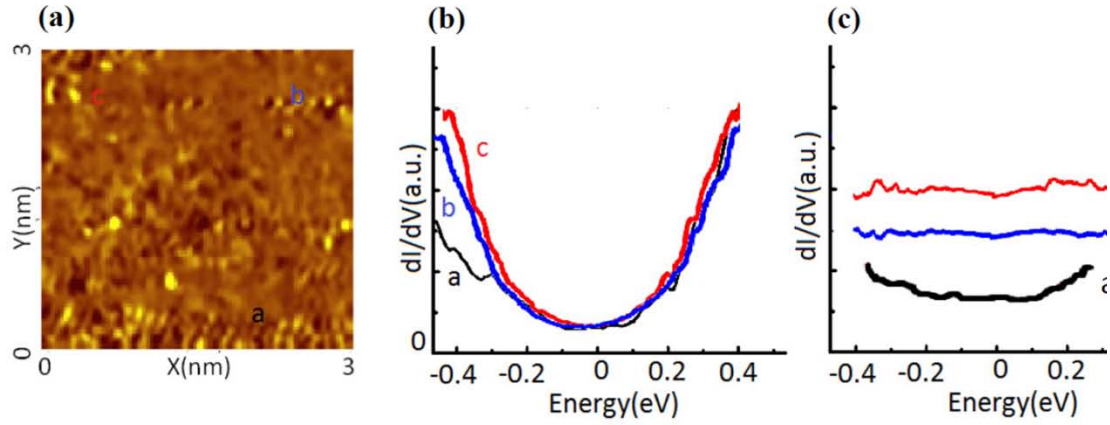

Figure 6.13: Amorphous region of CVD grown graphene. (a) Highly disordered region of graphene sample showing no atomic structure. (b) Representative spectra from regions across the sample. The spectra is completely parabolic. (c) Tunneling spectra with parabolic fit to the spectra subtracted. The spectra are offset in dI/dV for clarity. Conductance peaks do not follow a $\sqrt{|n|}$ dependence and so are not due to pseudo-magnetic fields.

the density of electrons with spin up and spin down at site "i". Assuming the onsite Coulomb repulsion U_{Cu} ~ 3 eV for the surface state of Cu [160], the on-site Coulomb potential U for graphene can be approximated by the relation $U = U_{Cu}\,(d_{Cu}/d)^2$, where d_{Cu} ~ 0.255 nm and d = 0.246 nm are the lattice constants of copper and graphene [159]. Hence, we find U ~ 3.2 eV, which is larger than the magnitude of the hopping constant ~ 3 eV. This simple analysis implies that the Coulomb interaction among Dirac fermions cannot be neglected. Thus, fractional quantum Hall states are feasible, with the Laughlin state of a filling factor $v = \pm 1/3$ and the related states of $v = \pm \frac{2}{3}, \pm \frac{4}{3}, \text{and } \pm \frac{5}{3}$ being the primary contributors [159]. We further note that our finding is the first observation of pseudomagnetic field-induced fractionally filled Landau levels in graphene. Moreover, the significantly more complicated strain found in our CVD-grown graphene on Cu differs

from the controlled strain observed in the case of graphene nanobubbles where the effective gauge potential leads to a relatively uniform magnetic field over each nanobubble.

6.3.3 Strain Induced Charging Effects

As discussed in Chapter 5, we should not only expect an induced vector potential and therefore a pseudomagnetic field, but also a scalar potential, Φ, from typical nontrivial strain. The presence of a scalar potential is the result of dilation and compression strain and is given by

$$V(x,y) = V_0\left(\frac{\partial \mathrm{u}_x}{\partial \mathrm{x}} + \frac{\partial \mathrm{u}_y}{\partial \mathrm{y}}\right) \qquad 6.4$$

where V_0 ~ 3 eV and $\frac{\partial \mathrm{u}_x}{\partial \mathrm{x}}\left(\frac{\partial \mathrm{u}_y}{\partial \mathrm{y}}\right)$ represent derivatives of the displacement field $\vec{\mathbf{u}}$. This scalar potential should give rise to a static charging effect if it is a spatially varying function, although this charging effect may be largely screened if the height variation *l* is much less than the magnetic length l_B described earlier. Considering the height variation *l* observed in our samples are on the order of 1.0 nm and are comparable to the magnetic length of 3.5 to 5.5 nm for magnetic fields of 50 Tesla, we expect significant charging effect to appear in CVD grown graphene on Cu.

The charging effect may be manifested by plotting the Dirac energy calculated from the tunneling spectra at every pixel as well as plotting the tunneling conductance at different constant bias voltages over our original graphene scan in Figure 6.11. These plots are show in Figure 6.14. The bias voltages are chosen to represent the pseudo-Landau levels of the "β" region spectra for *n* = 0, 1/3, 1, 2, 3. We notice immediately in the Dirac energy plot, that there is a nearly one-dimensional region close to the most strained area

immediately below the ridge that shows clear differences in the Dirac point. We notice this linear region is the same as the area where there is enhanced conduction in the constant bias conductance maps associated with smaller *n* values, confirming the notion of strain-induced charging effects. For higher energies (larger *n* values), the high-conductance region becomes less confined, which is reasonable because of the higher confinement energies $E \propto \sqrt{|n|}$) required for the Dirac electrons. We can attempt to quantify the compression/dilation strain by plotting changes in spatial variations $z(x,y)$of the height with respect to changes in the lateral directions for the topography scans given in Figure 6.11. In Figure 6.15 we plot

$$\left[\partial z(x,y)/\partial x\right]^2, \quad \left[\partial z(x,y)/\partial y\right]^2 \text{ and } \left[\left(\partial z(x,y)/\partial x\right)^2 + \left(\partial z(x,y)/\partial y\right)^2\right]$$

demonstrating the dilation and compression. We again observe a nearly one-dimensional region corresponding to an area immediately under the ridgeline in the topography that exhibits strongest dilation/compression. These maps are directly correlated with the conductance maps showing enhanced conduction along the ridgeline and provides direct evidence for strain-induced charging effects.

.

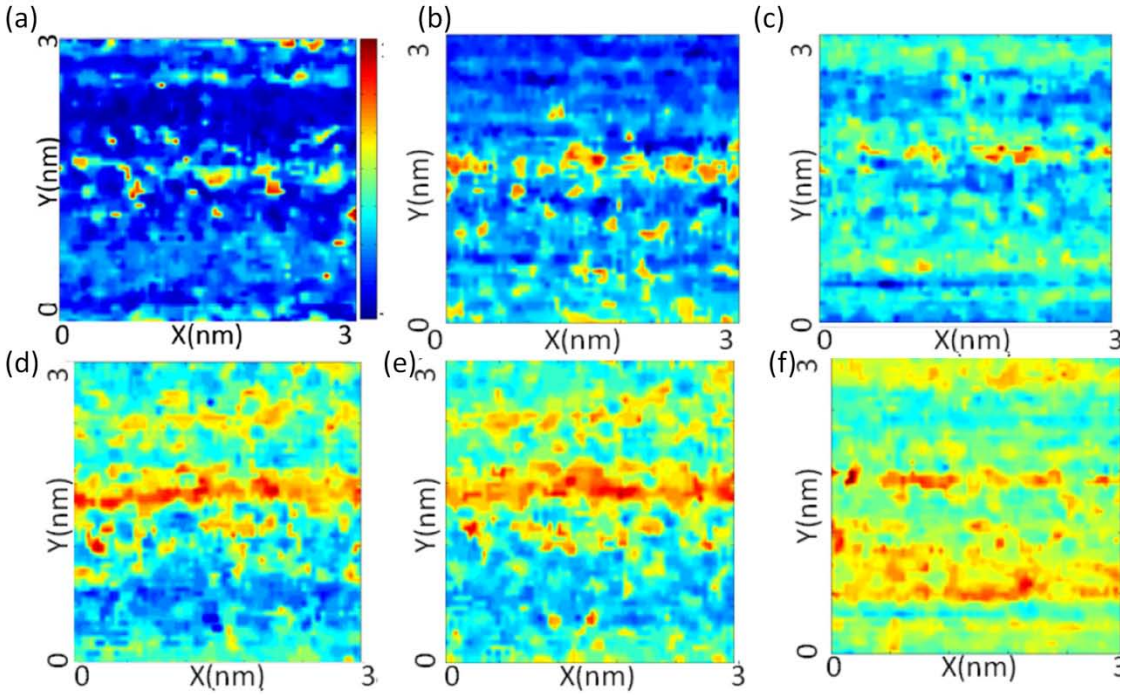

Figure 6.14: (a) Dirac energy map of the region specified in Figure 6.10. (b)-(f) : Constant-voltage tunneling conductance maps at quantized energies of the pseudo-Landau levels (b) $n = 0$, (c) $n = 1/3$, (d) $n = 1$, (e) $n = 2$, (f) $n = 3$, For smaller n values, an approximately one-dimensional high-conductance "line" appears near the topographical ridge where the most abrupt changes in height occur, suggesting significant charging effects. The confinement of the high-conductance region is reduced with increasing n.

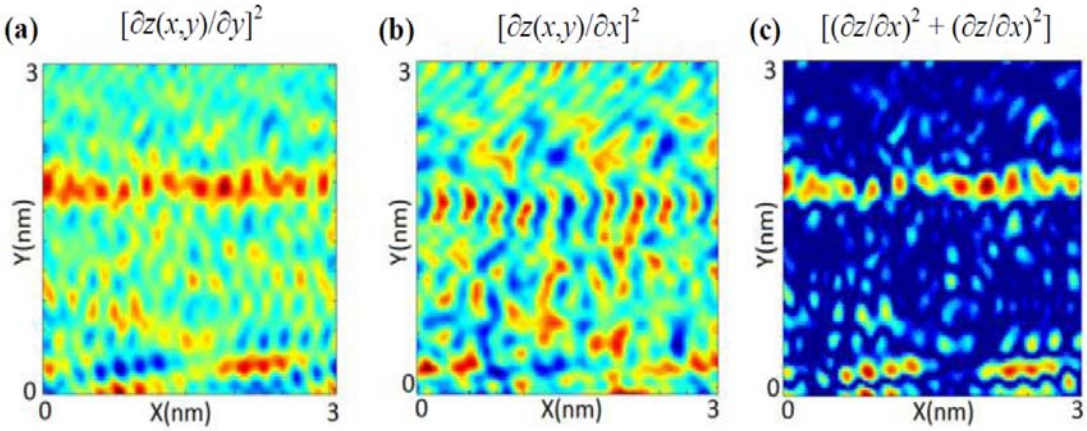

Figure 6.15 : Estimate of the spatial variations of the typical strain over the same region shown in Figure 6.10: (a) $\left[{}^{\partial z(x,y)}/_{\partial y}\right]^2$ map, (b) $\left[{}^{\partial z(x,y)}/_{\partial x}\right]^2$ map, and (c) $\left[\left({}^{\partial z(x,y)}/_{\partial x}\right)^2 +\right.$ *∂z(x,y)∂y2* map, showing maximum strain immediately below the ridgeline in the upper half of the image. This directly correlates with constant bias voltage conductance maps.

6.4 Studies on CVD Grown Graphene on SiO_2 Substrates

To test the assumption that the difference in the thermal expansion coefficients is responsible for the buckling of CVD grown graphene on Cu and therefore inducing strong strain and lattice distortions, a comparative study of CVD grown graphene transferred from Cu to SiO_2 was conducted. The assumption was that transferring graphene from the Cu foil according to methods described earlier in the chapter would allow the graphene to relax and when transferred to SiO_2 would be free of large-scale corrugations. It would no longer be forced to buckle or ripple by a large lattice mismatch to underlying Cu. Therefore, we expect that the transferred CVD-grown graphene to more closely resemble mechanically exfoliated graphene in its structural and electronic properties.

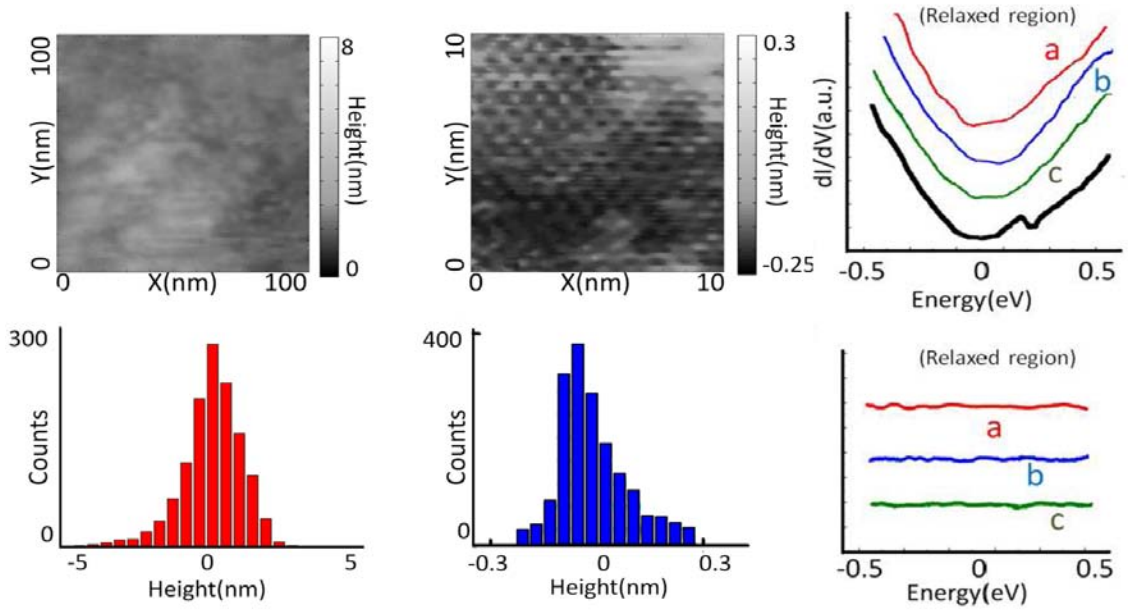

Figure 6.16: Comparative study of unstrained regions of CVD grown graphene transferred to a SiO_2 substrate: (a) Large-scale 100 nm × 100 nm topography image detailing small height variations in comparison with the strong height variations prior to being transferred to a new substrate. (b) Atomic resolution image (10 nm × 10 nm) showing a nearly flat surface. (c) Representative tunneling spectra from various regions of the sample. (d) Histogram of the height variations in (a), showing a surface roughness of ± 2.5 nm. (e) Histogram of the height variations in (b) showing a surface roughness of ± 0.25 nm. (f) Tunneling spectra with a parabolic background fit subtracted. Curves are offset for ease of viewing. No noticeable pseudo-Landau levels are resolved, indicating that the transferred graphene has for most regions recovered to a semipristine state.

Figures 6.16 and 6.17 shows the results of the comparative study. In general it was found that the height variations and the corresponding strain in the transferred graphene samples were much reduced, as shown in Figure 6.16. Hence, the conductance spectra for most areas of the sample are quite smooth without quantized conductance peaks and therefore resemble mechanically exfoliated graphene. There did exist rare regions were the graphene did not relax as was predicted. These regions retain strong rippling or buckling near grain boundaries of the large CVD-grown graphene sheet, which cannot be relaxed even after

removal of the underlying Cu substrate. Occasional quantized LDOS spectra are still present in these topographic regions that appear to contain remnant ridges or buckling of the CVD-grown graphene [159]. These quantized peaks still obey the general relation $E - E_D \propto \sqrt{|n|}$ except that the slopes are much smaller, implying much reduced pseudo-

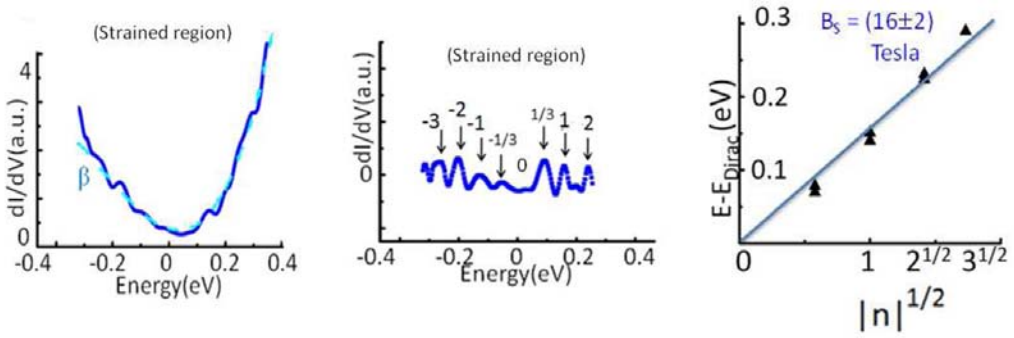

Figure 6.17: Comparative study of CVD grown graphene transferred to a SiO_2 substrate for strained regions. While majority of the transferred graphene becomes unstrained, certain rare regions retain their buckling and ridges. Spectra measured in these regions demonstrate clear influence of pseudomagnetic fields. (a) Representative spectra from a strained region. (b) Tunneling conductance of (a) with a parabolic background subtracted. Clear Landau levels can be resolved for n = ± 1/3, ± 1, ± 2, -3. (c) ($E - E_{Dirac}$)(eV) vs. $\sqrt{|n|}$ plot showing a pseudomagnetic field of ~ 8 Tesla. The pseudofields when present are substantiall reduced for the sample transferred to SiO_2.

magnetic fields. The calculated pseudo-fields are 8 ±1 Tesla. This is consistent with the significant reduction in strain upon transferring the graphene sample from Cu to SiO_2.

6.5 Local Spontaneous Time Reversal Symmetry Breaking

Following the arguments presented Chapter 5; the strain-induced pseudomagnetic fields, $\vec{\boldsymbol{B}}_S = \left(\frac{c}{ev_F}\right)\boldsymbol{\nabla} \times \vec{\boldsymbol{A}}$, do not break global time-reversal symmetry. However, the opposite gauge fields associated with the two pseudospin (opposing sublattices), K and K',

in reciprocal space can give rise to a zero mode [159]. This zero mode is a condensate where Dirac electrons become completely delocalized over the sample and yet remain alternately localized and antilocalized in the pseudospin projection in the real space [160]. More specifically, the presence of a pseudomagnetic field due to a repulsive second-nearest-neighbor interaction, such as that provided by a triaxial strain in a graphene nanobubble [161], can provide a net flux of a non-Abelian gauge field that preserves the time reversal symmetry and breaks the chiral symmetry of the free Dirac Hamiltonian [159]. This non-Abelian gauge field is shown theoretically [161] to serve as a catalyst for local spontaneous breaking of the time-reversal symmetry in graphene while preserving the chiral symmetry [159].

The experimental signature for this local spontaneous time reversal symmetry breaking is the presence (absence) of the n = 0 tunneling conductance peak for the two different sublattice atom sites in graphene. As shown in Figure 6.9 and 6.10, we do observe tunneling spectra with this alternating presence and absence of the n = 0 mode. This finding is the first direct evidence of spontaneous time-reversal symmetry breaking due to strain-induced gauge fields in graphene.

6.6 Discussion

In summary, topographic and spectroscopic studies of mechanically exfoliated graphene, CVD grown graphene on copper, and CVD-grown graphene transferred to SiO_2 reveal the important effect that strain and substrate can have on the electronic properties of

graphene. In particular, topographical defects such as ridges along grain boundaries can give rise to induced pseudomagnetic fields and charging effects. The large and non-uniform strain induces pseudomagnetic fields up to B~ 50 Tesla, and results in quantized conductance peaks associated with the integer and fractional quantum Hall states. These findings suggest the possibility of strain engineering of graphene into novel nanodevices.

Chapter 7

Scanning Tunneling Spectroscopic Studies of a Topological Insulator Bi_2Se_3

The Dirac materials are a new class of matter that exploits the mapping of electronic band structures and an embedded spin or pseudospin degree of freedom onto the relativistic Dirac equation. One of these new materials are the surface states (SS) of three dimensional (3D), strong topological insulators (STI) [162–165]. A crucial feature of these TIs is the suppression of backscattering of Dirac fermions due to topological protection that preserves the Dirac dispersion relation for any time-reversal invariant perturbation. However, while direct backscattering is prohibited in the SS of 3D-STI, sharp resonances are not excluded because Dirac fermions with a finite parallel momentum may be confined by potential barriers [139]. In fact, theoretical calculations for Dirac fermions in the presence of noninteracting impurities have predicted the occurrence of strong impurity resonances [166, 167]. In this chapter, we report on STS studies of massless Dirac fermions in the surface state of a three-dimensional strong topological insulator, Bi_2Se_3. Specifically we report direct observation of unitary impurity resonances in epitaxial thin film Bi_2Se_3 samples in the 3D limit. Additionally, for samples in the 2D limit, we find opening of energy gaps in the SS and the appearance of spin-preserving quasiparticle scattering interferences.

.

7.1 Basic Properties of Three-Dimensional Topological Insulators

Topological insulators in two or three dimensions have a bulk electronic excitation gap generated by a large spin-orbit interaction, and gapless edge or surface states on the sample boundary [168]. The surface states of a 3D-STI consist of an odd number of massless Dirac cones, with a single Dirac cone being the simplest case. The existence of an odd number of massless Dirac cones on the surface is ensured by the $Z2$ topological invariant [165] of the bulk.

These gapless surface states resemble chiral edge modes in quantum Hall systems, but with unconventional spin textures [172]. The spins of the surface states lie in the surface plane and are perpendicular to the momentum as shown in Figure 7.2(d). The dispersion relation of the SS of 3D-STI is a gapless Dirac cone. A key feature of such spin-textured boundary states is their insensitivity to spin-independent scattering, which is thought to protect them from backscattering and localization. Recent experiments with both ARPES and STS have probed the insensitivity of these chiral states to backscattering in Bi_xSb_{1-x} [172]. Despite strong atomic-scale disorder, backscattering between states of opposite momentum and opposite spin is absent, demonstrating that the chiral nature of these states protects the spin of the carriers [172].

As the topological nature is determined by the physics near the Γ point, it is possible to write down a simple effective Hamiltonian to characterize the low-energy properties of the system. Following the method outlined in [165] we can define a bulk Hamiltonian that describes Bi_2Se_3 as

$$\boldsymbol{H} = \epsilon_0(\boldsymbol{k})\boldsymbol{I}_{4\times4} + \begin{pmatrix} \mathcal{M}(\boldsymbol{k}) & A_1k_z & 0 & A_2k_- \\ A_1k_z & -\mathcal{M}(\boldsymbol{k}) & A_2k_- & 0 \\ 0 & A_2k_+ & \mathcal{M}(\boldsymbol{k}) & -A_1k_z \\ A_2k_+ & 0 & -A_1k_z & -\mathcal{M}(\boldsymbol{k}) \end{pmatrix} + \boldsymbol{o}(k^2) \qquad 7.1$$

using the basis of the Bi and Se bonding and antibonding p_z orbitals with both spins. We can define $k_\pm = k_x \pm ik_y$, $\epsilon_0(\boldsymbol{k}) = C + D_1k_z^2 + D_2k_\perp^2$, $\mathcal{M}(\boldsymbol{k}) = M - B_1k_z^2 + B_2k_\perp^2$ with A_1, A_2, B_1, B_2, C, D_1, D_2 and M being the model parameters as outlined in [165]. We note that if $M/B_1 > 0$ then the conduction and valence bands are inverted and the Hamiltonian describes a topological insulator instead of a trivial insulator. We can use the bulk Hamiltonian to solve for the Hamiltonian of the surface states by taking $k_z = 0$ [165]:

$$H_{SURF}(k_x, k_y) = \begin{pmatrix} 0 & A_2k_- \\ A_2k_+ & 0 \end{pmatrix} \qquad 7.2$$

using the basis of $|\psi_{0\uparrow}>, |\psi_{0\downarrow}>$. Here the surface states, $|\psi_{0\uparrow}>, |\psi_{0\downarrow}>$, are a superposition of the p_z orbital state and the spin states. We notice that Wquation 7.2 is the Hamiltonian that describes the Dirac equation for fermions with zero mass and spin ½ , similar to what we have seen in the case of graphene. The corresponding bandstructure of Bi_2Se_3 is shown in Figure 7.1, where the bulk energy gap ~ 300 meV is the largest among all known 3D TIs to date. As can be seen in Figure 7.1, the surface states can be clearly seen at the Γ point as red lines dispersing into the bulk.

7.2 MBE-Grown Bi_2Se_3 Epitaxial Films and Experimental Methods

The samples investigated in this thesis were provided by Liang He at UCLA and were epitaxial films grown on Si(111) by molecular beam epitaxy (MBE) [168]. Initial characterization of the Bi_2Se_3 samples by transmission electron microscopy revealed that

the films exhibited perfect triangular lattice structures, and ARPES studies revealed a single Dirac cone [168].

Atomic force microscopy (AFM) measurements of the topography revealed large-scale triangular terraced structures where the average height of each terrace is 0.95 nm, which corresponds to a single quintuple layer (QL), where the quintuple layer is defined in Figure 7.2(a). The typical lateral dimension of the top terrace structure ranges from 150 to 350 nm, and the width of each subsequent terrace is 70 ~ 90 nm. Initial characterizations were performed by Liang He at UCLA [168]. Figure 7.2 shows the basic crystalline structure of Bi_2Se_3. The average thicknesses of the samples studied in this thesis were 3-, 5-, 7-, and 60 QLs.

Once characterized, the Bi_2Se_3 samples were transported to Caltech in sealed argon environment. The samples were then gently cleaned in an ethanol bath and transferred to the STM system. The sealed STM was pumped down by a turbomolecular vacuum pump to a pressure of 10^{-7} torr at room temperature and then cooled to either 6 K or 77 K. Detailed surface topography and spatially resolved spectroscopy studies were carried out over typically 8 nm × 8 nm regions over a 128 pixel × 128 pixel grid. Normalized tunneling conductance $(dI/dV)/(I/V)$ vs. energy $(E = eV)$ spectroscopy was acquired at every pixel with a typical junction resistance of ~1 GΩ.

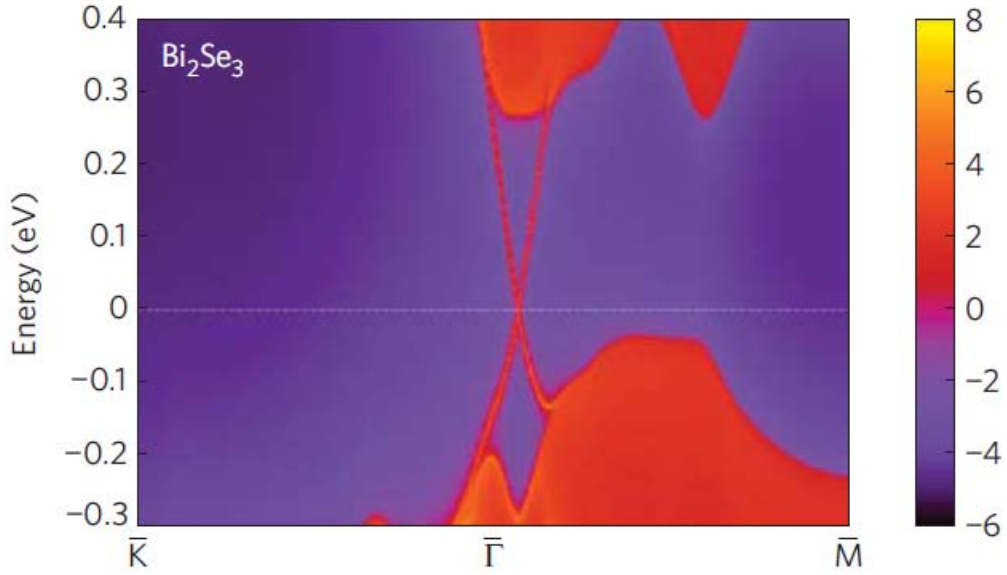

Figure 7.1: Energy and momentum dependence of the LDOS. Here, the warmer colors represent higher LDOS. The red regions indicate bulk energy bands and the blue regions indicate bulk energy gaps. The surface states can be clearly seen around the Γ point as red lines dispersing in the bulk gap. Image taken from [165].

7.3 Experimental Results for 3D Films

Tunneling conductance spectra revealed a Dirac-like LDOS which were generally consistent throughout flat regions of the sample surfaces for the 7-QL and 60-QL samples. Figure 7.3 (a) shows typical tunneling spectra for 3-QL, 7-QL, and 60-QL samples. The Dirac point was calculated by performing linear fits to each spectra and are approximately E_D = -73 ± 38 meV for 60-QL and E_D = -100 ± 25 meV for 7-QL samples. Histograms of the Dirac energy across each scan are shown in Figure 7.3(b–c). The thinnest sample, 3-QL, reveals a ~ 400 meV energy gap opening up around E_F , which is expected for the 3D-TIs in the 2D limit [170] and will be elaborated further in Section 7.4. We notice generally that the Dirac point shifts away from the Fermi energy (E = 0) with decreasing sample

thickness, which we attribute to the excess doing effects from the interface between the Bi2Se3 film and the substrate [168].

In Figure 7.4(a–b), spatial maps of the tunneling conductance for, respectively, 60- and 7-QL are atomically resolved and show relatively consistent tunneling spectra with the exception of a few atomic impurities. These atomic impurities are manifested by the localized high conductance in Figure 7.4(a–b). The sharp conductance peaks associated with the presence of impurities generally occur in the tunneling spectra at energies near the Dirac point E_D. To investigate the spatial evolution of tunneling spectra associated with the presence of these quantum impurities, we plotted different spectral linecuts across different regions of the constant bias conductance maps shown in Figure 7.3 for the 60-QL sample. For a linecut of tunneling spectra (dI/dV vs. E) along areas without impurities the tunneling spectra are generally consistent showing a Dirac energy slightly below the Fermi level. This is shown in Figure 7.5(a) In comparison, the tunneling spectra plotted directly across quantum impurities reveal strong resonant conductance peaks at energies near $E \sim E_D$ as shown in Figures 7.5(b–d). These resonant peaks are spatially confined to a radius (r) ~0.2 nm of the impurity center. The surface states of the TI rapidly recover from the impurities with distance traveled from the impurity. If we plot linecuts of the tunneling spectra between two impurities separated by only one lattice constant, the spectra for the inter-impurity region exhibit strong interference for energies deep into the bulk valence band while the surface state spectra has been restored to that of the host. This is demonstrated in Figures 7.5(e–f). This evidence suggests strong topological protection of the surface state against impurities even in the limit of significant effects on the bulk state.

For comparison, we can plot tunneling spectra linecuts through impurities observed on the surface of the 7-QL sample (Figure 7.6(a–c)). Similar to the 60-QL sample, a linecut passing through no impurity reveals Dirac-like spectra with a Dirac energy below the Fermi energy (Figure 7.6 (c)). A linecut passing through two impurities (Figure 7.6(b)) reveals two resonances which are much reduced in comparison to the 60-QL sample. The surface states of the host still rapidly recover from the impurities. As will be discussed later, the weakened impurity resonance may be attributed to the larger energy separation of E_D from $E_{F.}$

To better understand the spatial confinement and energy dependence of the impurity resonances, we can plot the spatial dependence of the tunneling conductance near one of the isolated impurities for various energies. In Figure 7.7 (a) we plot the tunneling conductance as a function of *r*, distance from impurity center for energies E= -40, -150, and -275 meV for the 60-QL sample. We observe at energies near the Dirac point (E = -40 meV) a strong resonance in the tunneling conductance over a very narrow spatial range ($r \sim \pm$ 0.2 nm). For $E < E_D$ but still within the SS (E= -150 meV), the spectral resonance diminishes rapidly with no impurity resonance visible for energies inside the bulk valence band (E= -275 meV). In the case of two closely located impurities, we find that the impurity resonances at energies near the Dirac point (E = -40 meV) remains strongly localized spatially ($r \sim \pm$ 0.2 nm). Moreover, the SS spectrum of the small intermediate region between two impurities appears to fully recover to that of the host (E = -150 meV), whereas the bulk spectrum (E = -400 meV) for the same intermediate region exhibits

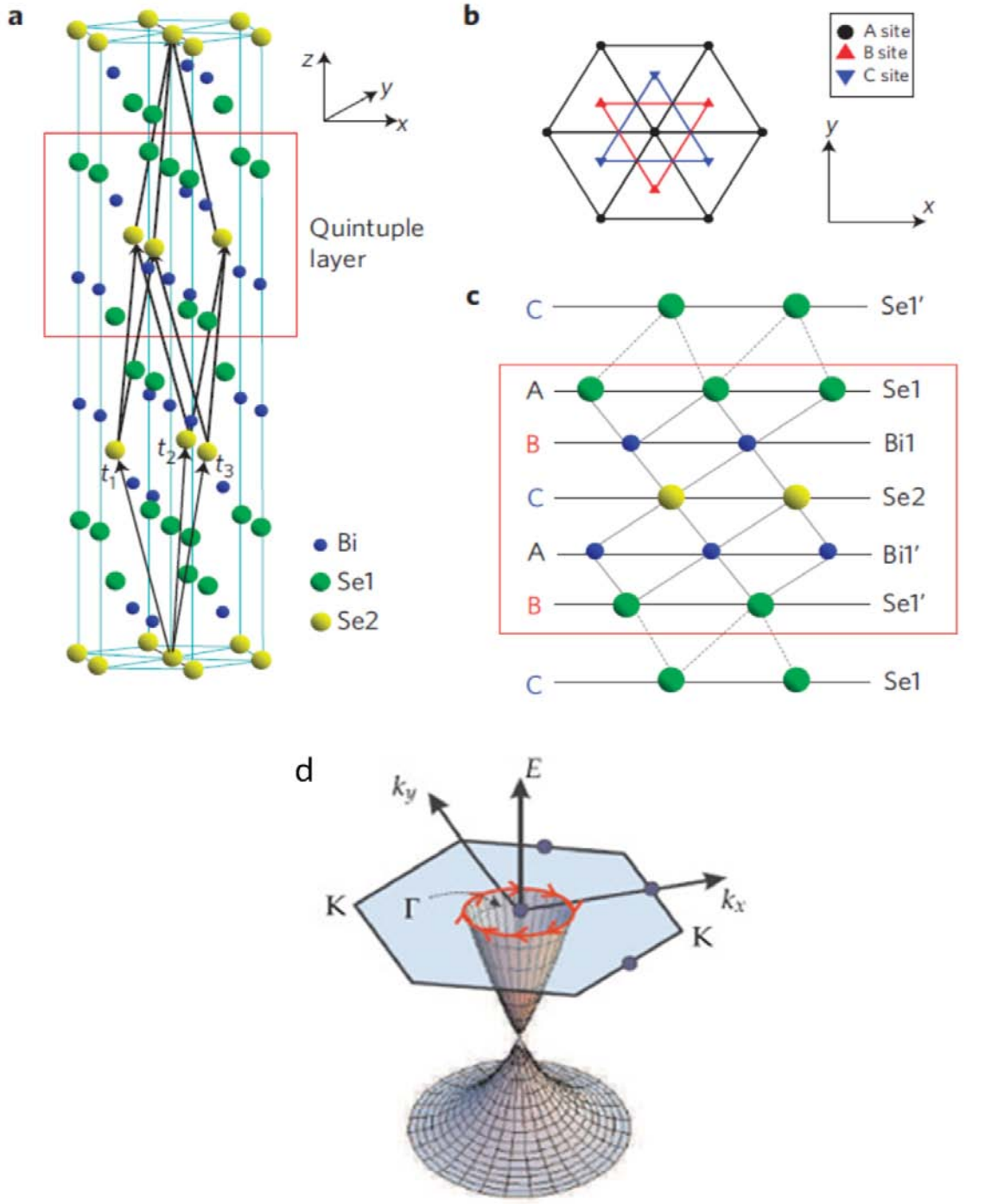

Figure 7.2: (a) A 3D representation of the alternating triangular lattice structure of Bi_2Se_3. A quintuple layer with Se_1–Bi_1–Se_2–Bi_1–Se_1 is indicated by the red square. (b) The top view of Bi_2Se_3. (c) A side view of the typical quintuple layer. (d) Energy vs. momentum dispersion for the surface state of Bi_2Se_3, showing spins of the surfaces are perpendicular to the momentum. Image taken from [165].

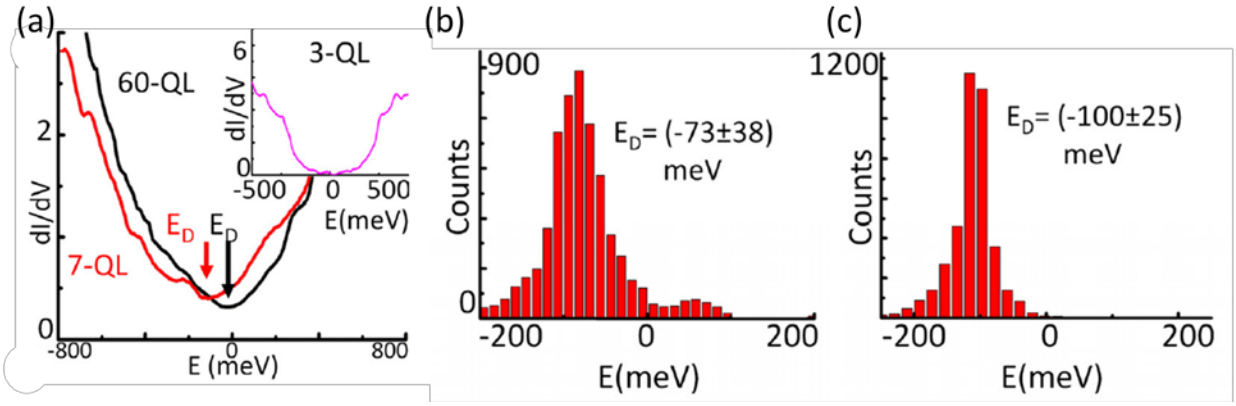

Figure 7.3: Dirac energy of Bi_2Se_3.[169] (a) Representative tunneling spectra of both 60-QL and 7-QL samples with arrows pointing to the Dirac energy. (Inset) Representative spectra of 3-QL sample showing opening of an energy gap. (b–c) Histograms of the Dirac energy for the 60- and 7-QL samples

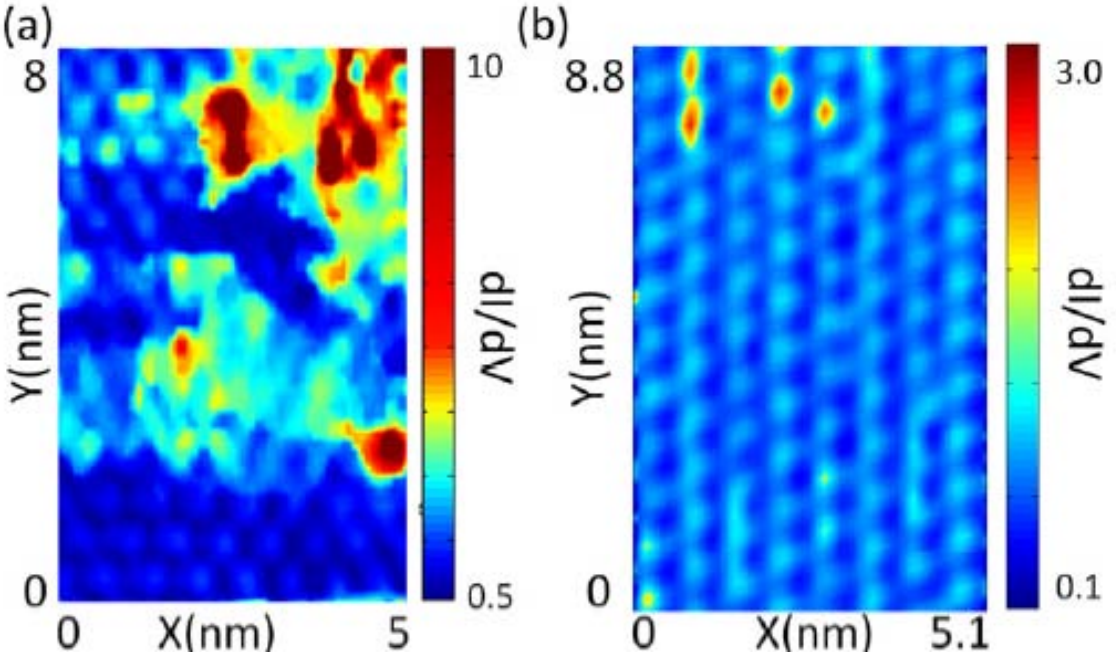

Figure 7.4: (a) Tunneling conductance map of the 60-QL sample over a 8 nm × 5 nm region [169]. Atomic impurities are realized as localized areas of high conductance. (b) Tunneling conductance map of the 7-QL sample of a 8.8 nm × 5.1 nm region [169]

strong interferences. This is demonstrated in Figure 7.7 (b). Similarly, for the 7-QL sample with a larger Dirac energy, the impurity resonance at $E \sim E_D$ for either an isolated impurity or two closely spaced impurities is also highly localized, as exemplified in Figure 7.7 (c–d). The surface state spectrum recovers rapidly and the effect of adjacent impurities on the bulk valence band diminishes significantly relative to that of the 60-QL sample. The quick recovery of the surface state spectrum from impurities may be understood as the result of topological protection of the SS in Bi_2Se_3.

As mention earlier the weakened spectral intensity of the impurity resonances with increasing $E = E_F - E_D$. That is, the spectral weight of impurity resonances diverges as the Fermi energy approaches the Dirac point. This is consistent with the theory for non-interacting point impurities embedded in a system of massless Dirac fermions [167]. Following the theoretical analysis in [167] based on the Keldysh Green function formalism, Hao Chu showed the theoretical dependence of the intensity of the impurity resonances on $\tilde{E} = E_F - E_D$ is in reasonable agreement with our empirical findings [169]. This finding is illustrated in Figure 7.8. This finding suggests that the impurity resonances for both samples are in the unitary limit, where the impurity strength U_{imp} for $\Omega_{imp} \rightarrow E_D$ diverges via the relation $(\Omega_{imp} - E_D) \sim 5\ \mathrm{sgn}(U_{imp})/(|U_{imp}|\ \ln|U_{imp}|)$ with Ω_{imp} being the impurity energy. Specifically, we find that for $\tilde{E} \rightarrow 0$, the impurity resonance diverges logarithmically at $T \rightarrow 0$. However, the intensity of impurity resonances diminishes rapidly with increasing $\tilde{E}$, as shown in Figure 7.8(a) [169].

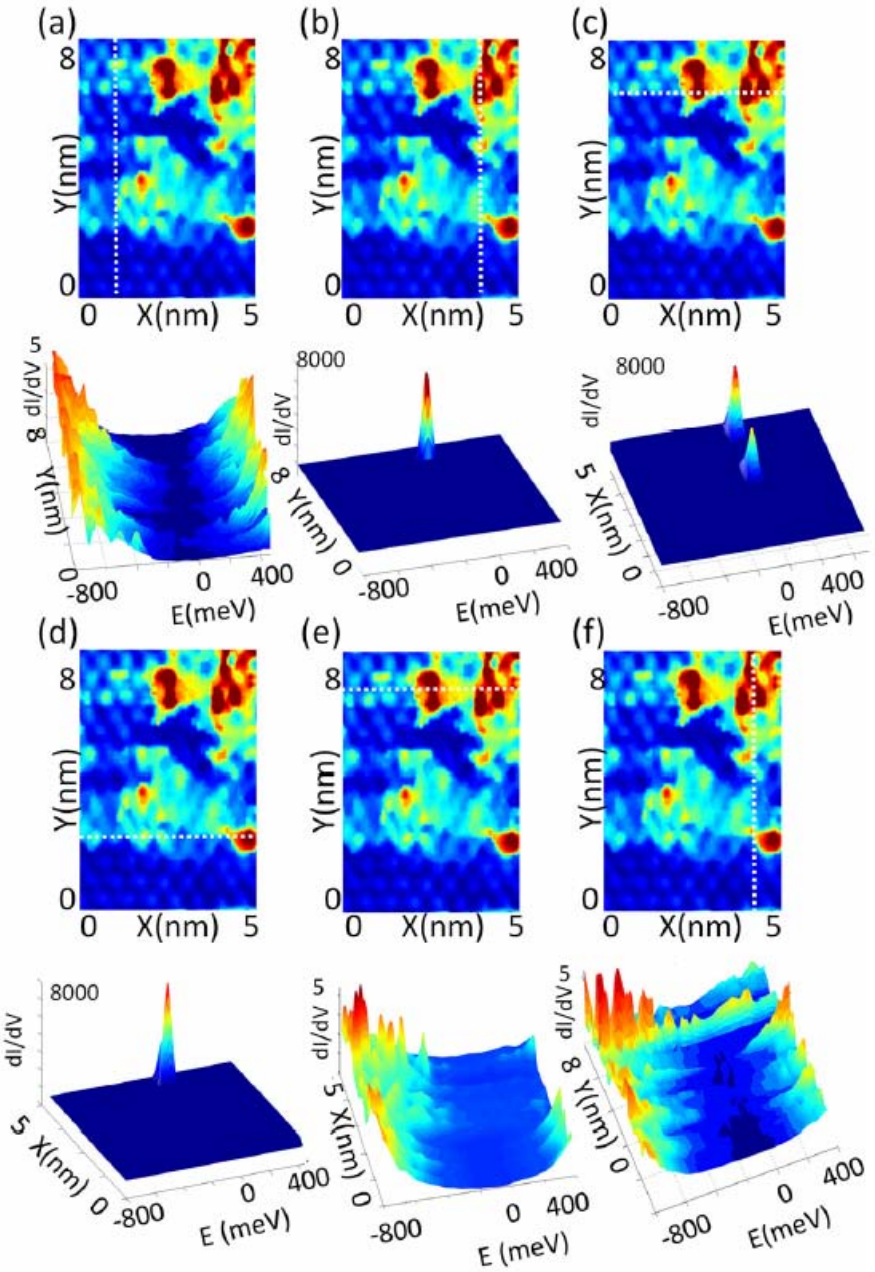

Figure 7.5: Evolution of tunneling spectra along various linecuts of the 60-QL sample at *T* = 77 K [169], where the white dotted line in each upper panel represents a linecut across the constant-energy conductance map, with the corresponding tunneling spectra along the linecut given in the lower panel: (a) Across an impurity-free region; (b) Across a single impurity; (c) Across two impurities; (d) Across an isolated impurity; (e) Between two closely spaced impurities along the horizontal direction; (f) Between two closely spaced impurities along the vertical direction

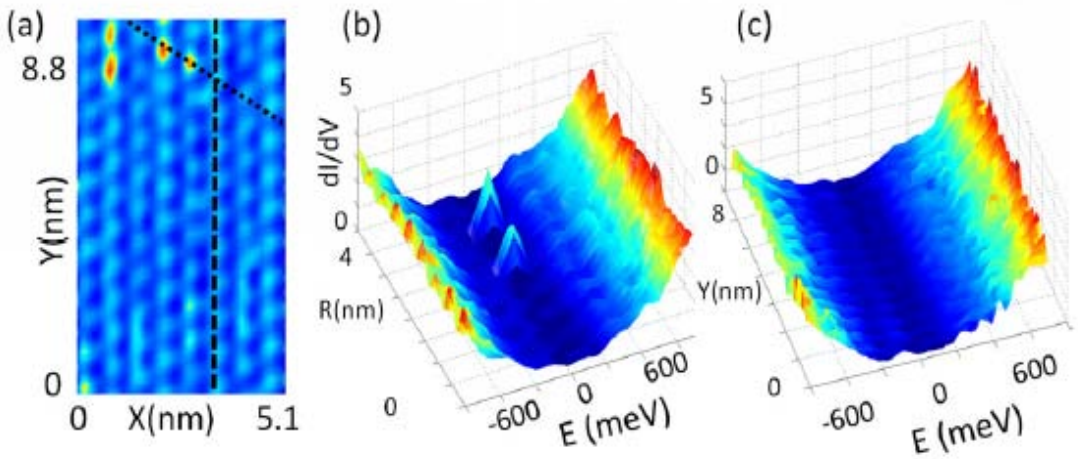

Figure 7.6: Evolution of tunneling spectra along various linecuts of the 7-QL sample at T = 77 K [169]. (a) Atomically resolved constant-energy conductance map where the black dotted lines represent linecuts across the conductance map, with the corresponding tunneling spectra along the linecut given in (b) Across two impurities; (c) Across no impurity

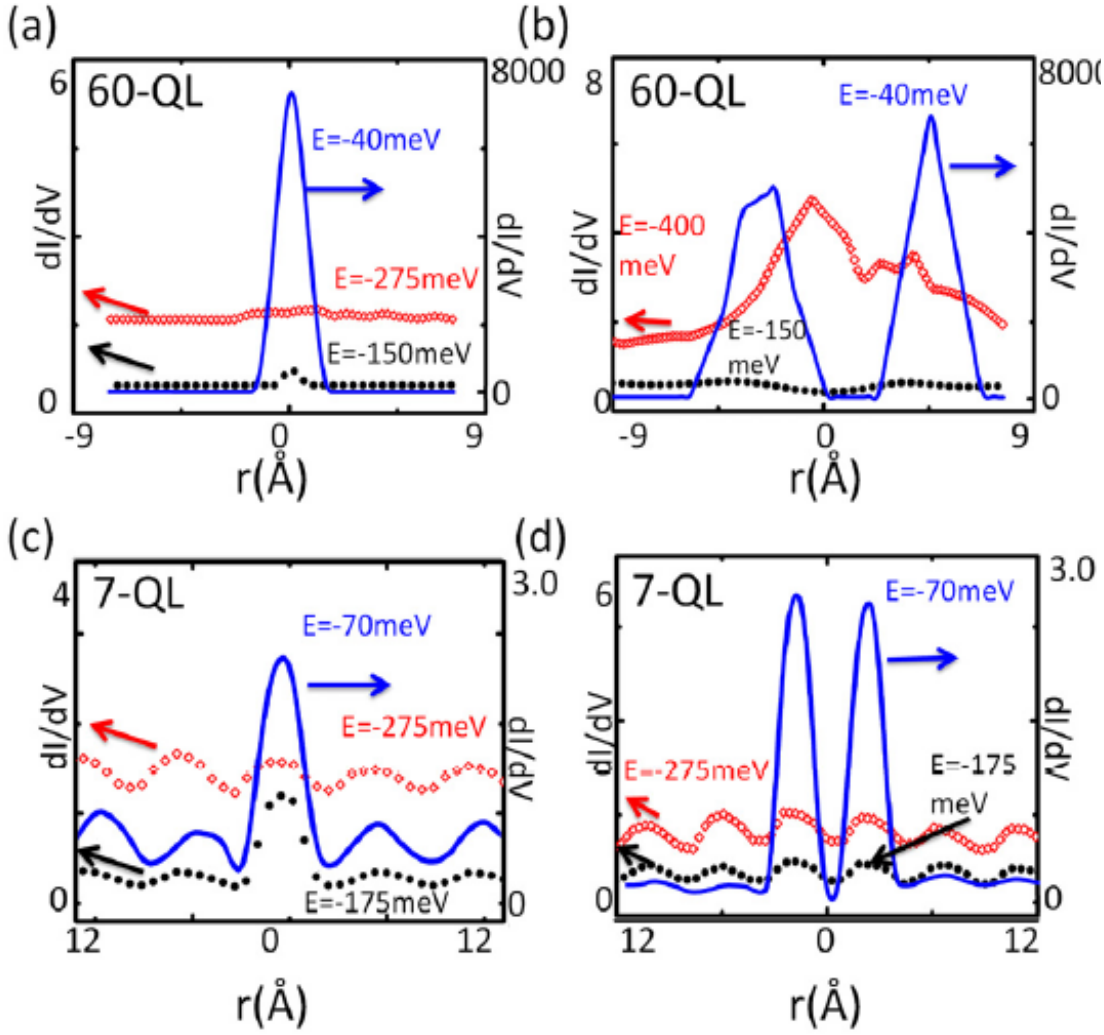

Figure 7.7: Spatial distribution and energy dependence of the impurity resonances for 60-QL and 7-QL samples [169]: (a) Tunneling conductance vs. spatial distance for the 60-QL sample from the center of an isolated impurity for E= -40, -150, and -400 meV. (b) Tunneling conductance vs. spatial distance for the 60-QL sample from the center of two adjacent impurities for E = -40, -150, and -275 meV. (c) Tunneling conductance vs. spatial distance for the 7-QL sample from the center of an isolated impurity for E = -70, -175, and -275 meV. (d) Tunneling conductance vs. spatial distance for the 7-QL sample from the of two adjacent impurities for E = -70, -175, and -275 meV

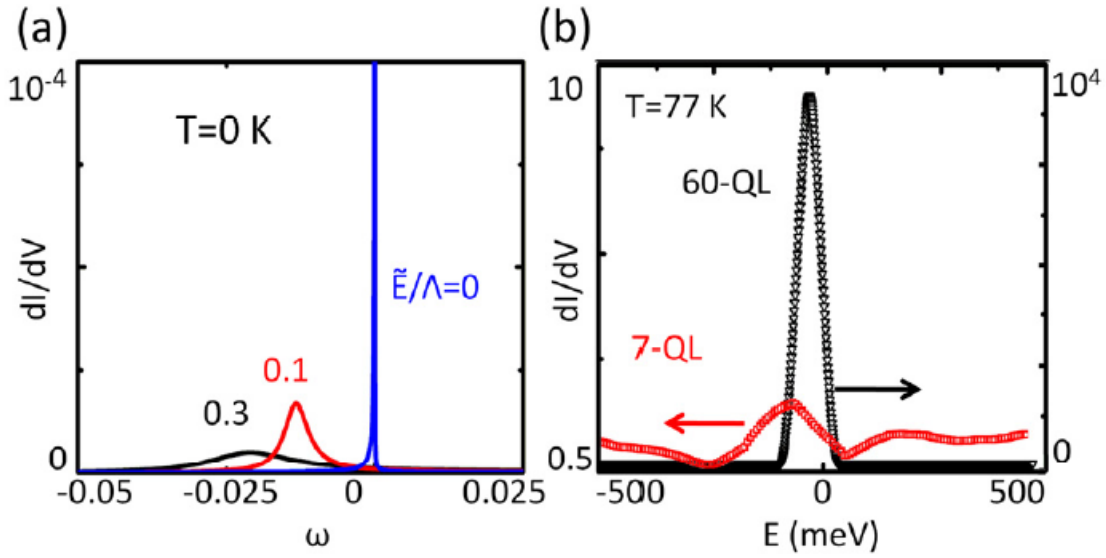

Figure 7.8: (a) Theoretical predictions for the dependence of the strength of the impurity resonance on $\tilde{E}/\Lambda$ where Λ denotes a cutoff energy and $\tilde{E} = |E_D - E_F|$ [169]. (b) Representative point spectra above the quantum impurities in the 7- and 60-QL samples showing strong resonances at energies very close to the Dirac energy. The experimental curves show qualitative agreement with the theoretical predictions for the dependence of the intensity of the impurity resonances on $E = E_F - E_D$.

7.4 Experimental Results for Bi2Se3 Films in the 2D Limit

While the dispersion relation of the SS of 3D-STI has been confirmed to be a gapless Dirac cone, for 3D-STI in the thin-film limit the coupling between opposite surface states in space is theoretically expected to open up a hyperbola shaped energy gap [170]. The thin film may further break the top–bottom symmetry due to the asymmetric chemical potentials between the surface (in vacuum) and the interface of the thin film with a substrate. (Also referred to as Structural Inversion Asymmetry (SIA)). This will lead to a Rashba-like coupling and further energy splitting in the momentum space [170]. Mathematically, we understand the occurrence of the energy splitting if we take this asymmetry into account, by adding a V(z) potential term to the Hamiltonian. Combining

the consideration of wavefunction overlaps between the surface and interface and the asymmetric chemical potentials, we find that the resulting gapped surface states lead to the following dispersion relations [170]

$$E_{1\pm} = E_0 - Dk^2 \pm \sqrt{\left(\frac{\Delta}{2} - Bk^2\right)^2 + \left(\left|\tilde{V}\right| + \hbar v_F k\right)^2}$$

$$E_{2\pm} = E_0 - Dk^2 \pm \sqrt{\left(\frac{\Delta}{2} - Bk^2\right)^2 + \left(\left|\tilde{V}\right| - \hbar v_F k\right)^2} \qquad 7.3$$

where $\hbar$ is the Planck's constant, v_F the Fermi velocity, and Δ the energy gap in the thin film limit. This is in contrast to the dispersion relation in the film limit without substrate asymmetry effect

$$E_{\pm} = E_0 - Dk^2 \pm \sqrt{\left(\frac{\Delta}{2} - Bk^2\right)^2 + (\hbar v_F k)^2} \ . \qquad 7.4$$

We can see as a consequence of the Rashba-like coupling and the gapped Dirac hyperbola in the thin-film limit of a 3D-STI is that the energy dispersion relation would involve four split Fermi surfaces with chiral spin textures for surface-state spin-up, interface-state spin-up, surface-state spin-down, and interface-state spin-down [170]. Consequently, quasiparticle interferences due to elastic impurity scattering are expected only between Fermi surfaces with the same spin texture [173], similar to the findings from STS studies of the QPI in Bi_xSb_{1-x} [171]. However, 3D Bi_xSb_{1-x} is a 3D-STI with much more complicated Fermi surfaces and therefore multiple spin-preserved QPI wave-vectors are allowed [172], which is in contrast to the single Dirac cone in 3D Bi_2Se_3 where no QPI occurs near the Dirac energy E_D.

Comparatively, for the four split Fermi surfaces in 2D Bi_2Se_3 thin films, only one value for the QPI wave-vector **q** is expected for a given quasiparticle energy due to the preservation of spin textures from spin-up interface to spin-up surface states and from

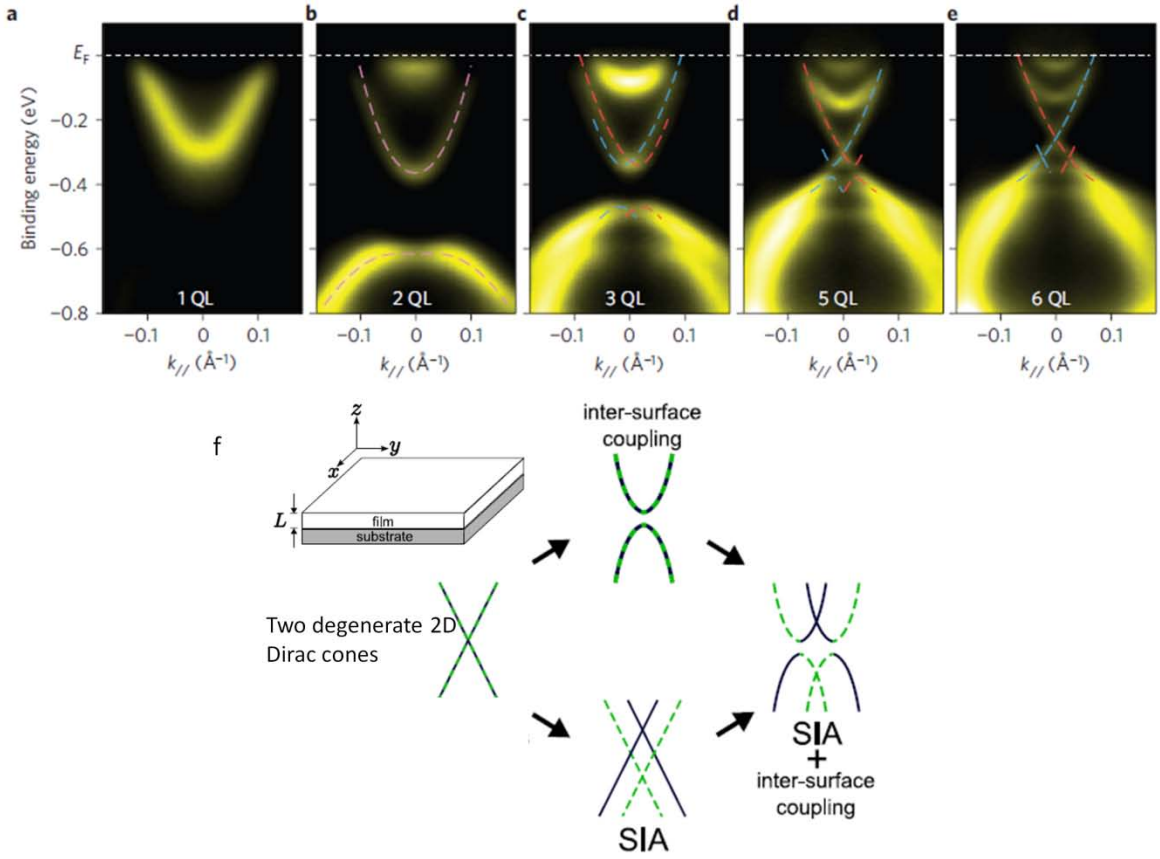

Figure 7.9 (a–e), ARPES spectra of 1, 2, 3, 5 and 6 QL along the Γ- K direction measured at room temperature. The energy gap opening is clearly seen when the thickness is below six quintuple layers. The gapped surface states also exhibit sizeable Rashba-type spin–orbit splitting because of the substrate-induced potential difference between the two surfaces. (f) Schematic effect SIA and inter-surface coupling. The blue solid and green dashed lines correspond to the states residing near the top and bottom surfaces, respectively. Images modified from [170, 171].

spin-down interface to spin-down surface states. Further, the |**q**|-values should be smaller than the reciprocal lattice constants, and will decrease as the energy E approaches the Dirac energy [173]. The theoretical predictions for Rashba-like splitting in the SS of 3D-TIs in the thin-film limit have been verified by ARPES studies of Bi_2Se_3 films on SiC [171]. As shown in Figure 7.9, an energy gap Δ opens up for thickness < 6-QL, and the gap increases with decreasing sample thickness. Four pieces of split SS Fermi surfaces can also be resolved from the ARPES studies.

Initial STS studies of a 5-QL Bi_2Se_3 thin film on Si (111) revealed that the Fourier-transformed (FT) conductance maps at various constant energies indeed exhibited a single QPI |**q**|-value for a given energy, as exemplified in Figures 7.10 (a–c). As expected the magnitude of QPI wave vectors decreases when energy E approaching the Dirac point E_D. These results are qualitatively consistent with preservation of spin textures in QPI for 3D-STI in the thin-film limit. However, detailed analysis of our STS data is not in quantitative agreement with the fitting parameters derived from ARPES studies of Bi_2Se_3 films on SiC [171]. Given that different interfaces are known to vary significantly in their contributions to doping [174], it is not surprising that the quantitative parameters derived from our sample on Si(111) differ from the fitting parameters in [171]. Further STS studies of Bi_2Se_3 films with different thicknesses and substrates together with ARPES studies of Bi_2Se_3 films on the same substrate will be necessary to resolve the quantitative differences.

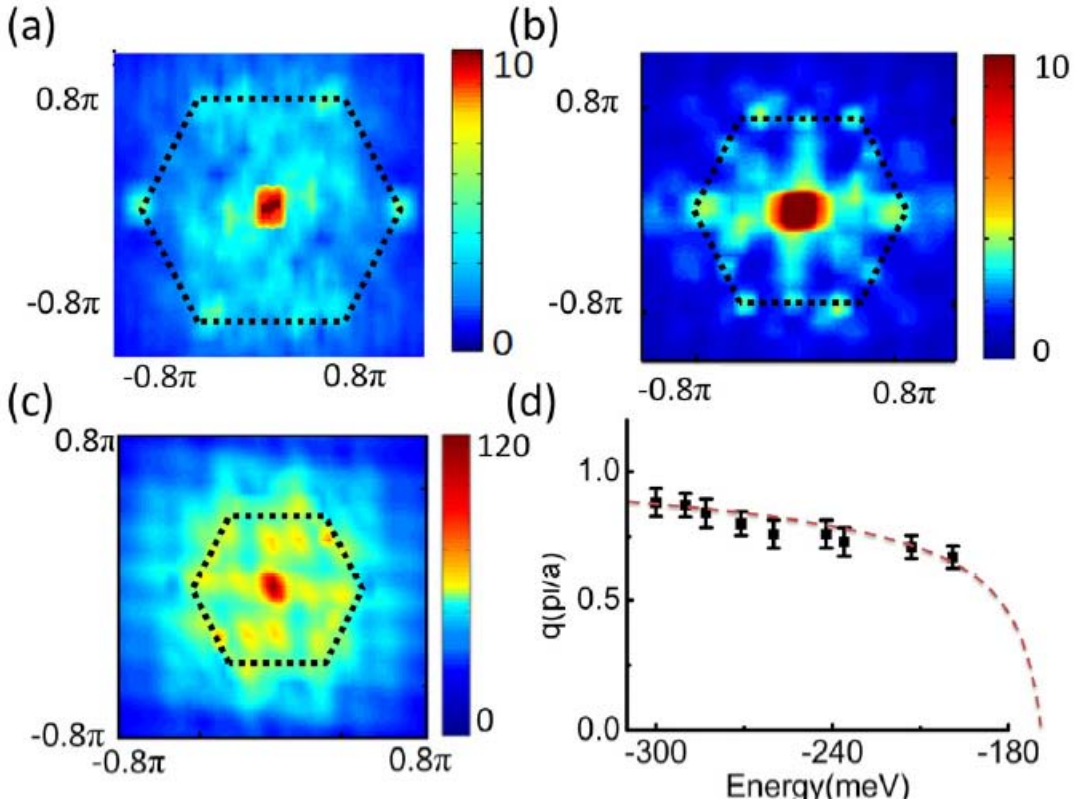

Figure 7.10 : (a–c) Fourier transformed (FT) tunneling conductance maps that reveal energy-dependent QPI wave vectors that preserve spin texture. (d) The energy dependence of the QPI wave vectors determined from all FT conductance maps shows decreasing |**q**| values as energy approaches E_D [173].

7.5 Discussion

In summary, we have presented STS studies of the 3D-STI, Bi_2Se_3 and found spectroscopic evidence of impurity resonances in the surface state of Bi_2Se_3. The impurities are in the unitary limit and the spectral resonances are localized spatially within a radius, r~ 0.2 nm. The spectral weight of impurity resonances diverges as the Fermi energy approaches the Dirac point, and the rapid recovery of the surface state from nonmagnetic impurities suggests robust topological protection against perturbations that preserve time

reversal symmetry. Additionally, we found evidences for Rashba-like splitting of the SS in the 2D limit, with QPI wave-vectors preserving the spin textures, which is another manifestation of the topological protection of the surface states

Chapter 8

Conclusion

We have used scanning tunneling microscopy(STM) to study electronic properties of both high-temperature unconventional superconductors, particularly the electron-type cuprate $La_xSr_{1-x}CuO_2$ and the iron-based $Ba_1(Fe_{1-x}Co_x)_2As_2$, and Dirac materials, specifically single-layer graphene and the three-dimensional strong topological insulator Bi_2Se_3.

We have presented magnetic-field-dependent STS studies of the electron-type superconductor La-112. Spatially resolved quasiparticle tunneling spectroscopy revealed a hidden pseudogap inside vortices and unconventional spectral evolution with temperature and magnetic field dependence. In comparison with the STS data of hole-type cuprates and other experimental data such as angle-resolved photoemission spectroscopy (ARPES) and inelastic neutron scattering, we find that the scenario of coexisting competing orders (CO) with superconductivity (SC) provides the best and most consistent explanation for all experimental findings in both hole- and electron type superconductors. In contrast, we have observed two-gap superconductivity for multiple doping levels in the $Ba(Fe_{1-x}Cox)_2As_2$ single crystals. Both superconducting gaps decrease monotonically in size with increasing temperature and disappear for temperatures above the superconducting transition temperature, T_C. Magnetic resonant modes that follow the temperature dependence of the superconducting gaps have been identified in the tunneling quasiparticle spectra. Together with the quasiparticle interference (QPI) analysis and magnetic field

studies, our STS studies provide strong evidence for two-gap sign-changing s-wave superconductivity. The common features found in both cuprate and ferrous high-temperature superconductors suggest that the paring potential for superconductivity is repulsive and predominantly electronic in nature.

In comparison, our studies of Dirac fermions in graphene revealed the important effect of strain and substrate on the electronic properties of mechanically exfoliated graphene, CVD grown graphene on copper, and CVD-grown graphene transferred to SiO_2. Topographical ridges and defects occurred during the CVD growth process and gave rise to giant pseudomagnetic fields and charging effects. The resultant large and nonuniform strain induced pseudomagnetic fields up to B~ 50 Tesla, which manifested as quantized conductance peaks related to the quantum Hall states. While in the bulk limit of the 3D-STI Bi_2Se_3, we found spectroscopic evidence of impurity resonances in the surface state. The impurities were in the unitary limit and the spectral resonances were localized spatially within a radius, r~ 0.2 nm. The spectral weight of impurity resonances diverged logarithmically as the Fermi energy approaches the Dirac point. The rapid recovery of the surface state from nonmagnetic impurities suggests robust topological protection against perturbations that preserve time reversal symmetry. In the thin-film limit of the 3D-STI, we observed Rashba-like splitting of the surface states and evidences for spin-preserved quasiparticle scattering interferences, which was again a manifestation of the topological protection of the surface states by time-reversal symmetry.

Future considerations include the attempt to fully investigate the vortex state of ferrous superconductors for multiple doping levels. We wish to fully investigate the

overlap of competing orders with superconductivity in the phase diagram of temperature vs. doping for the electron type “122” systems.

The possibility of using strain engineering for nanodevices in graphene combined with the near completion of a cryogenic STM/SEM opens the door to large-scale studies of arrays of strain-engineered nano devices. Also, recent developments and major improvements in the growth methods of CVD grown graphene open the possibility of studying large-scale, single-layer CVD graphene without strong strain effects.

Appendix A

STM Design Drawings

A.1 STM Body Design

In order to improve mechanical and temperature stability in the current STM, the previous macor STM body was remachined out of the metal molybdenum. Molybdenum was chosen for its excellent thermal properties and that its thermal expansion, is very close to macor's and coppers thermal expansion coefficients. Improvements in the design allowing quick disconnect macor pieces for wiring to the piezo-electric stacks of the course z-stage and tube scanner was also added.

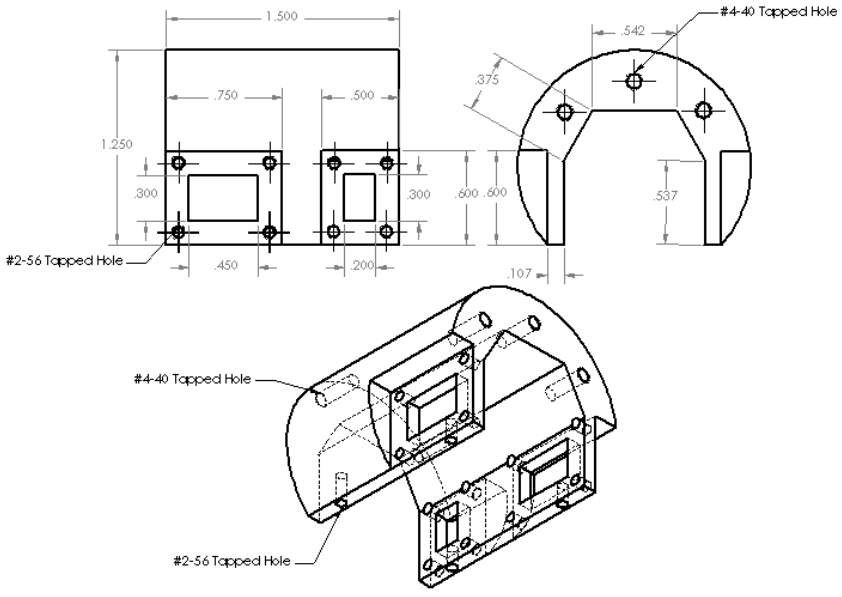

Figure A1

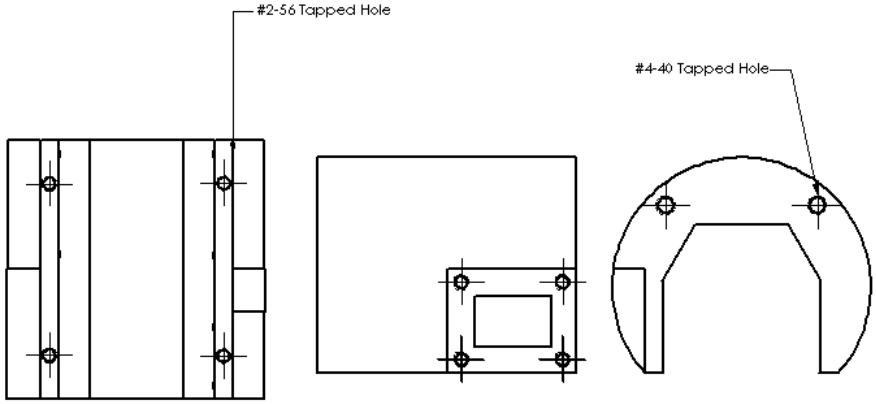

Figure A2

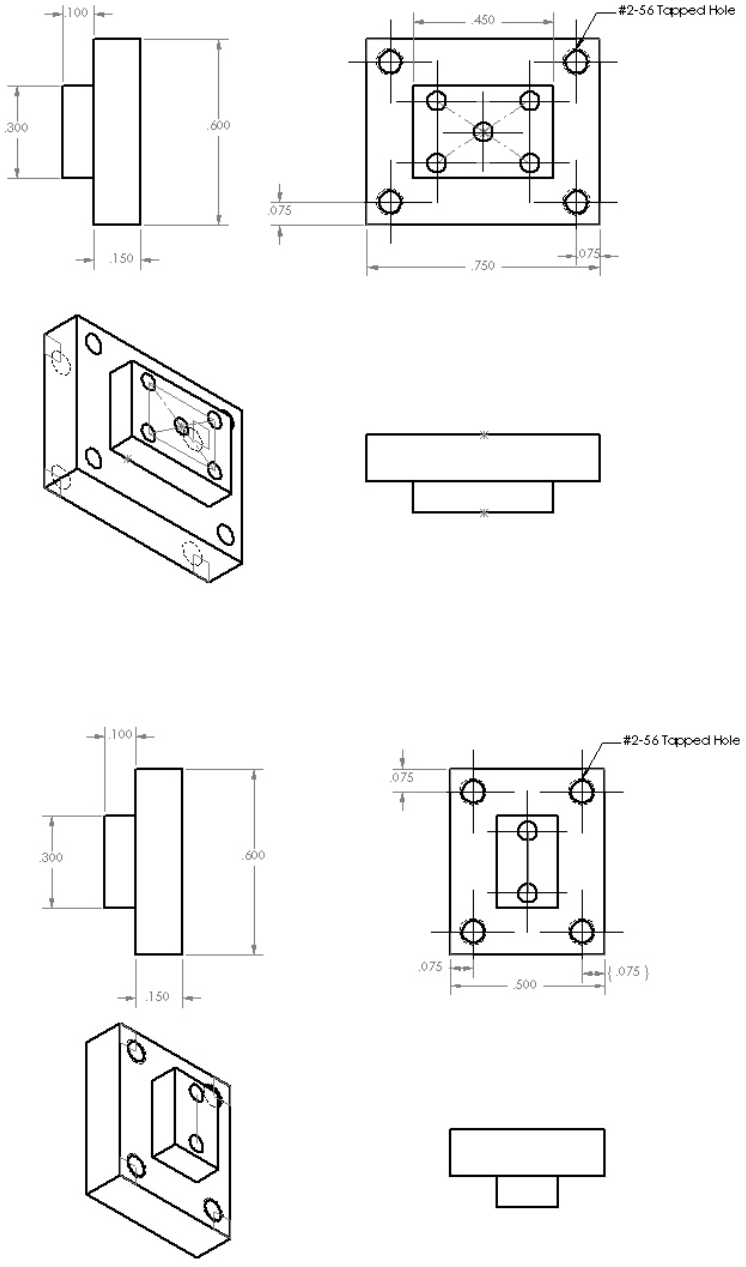
.100
.300
.600
.150
.450
#2-56 Tapped Hole
.075
.750
.075
.100
.300
.600
.150
#2-56 Tapped Hole
.075
.075
.500
.075

Figure A3

Appendix B

Mathematical Data Processing for STS Data: Matlab Programs

To investigate correlated electron systems, large STS data files must be analyzed quickly and efficiently. STS data files consist of I vs. V information of sizes exceeding several Gigabytes. From the current vs. voltage files we must calculate the differential conductance vs. voltage. These programs must vary according to the needs of the data if it is graphene or a superconductor or a topological insulator. If the STS data is unfortunately noisy then the noise reduction methods must be performed on the data. To accomplish this the mathematical analysis program Matlab was utilized. Contained in this appendix are the following programs that calculate the differential conductance, dI/dV, the noise reduction programs, and data analysis programs.

Matlab programs

The first program, loadv, loads the data from the data files

Loadv:

```
% This program loads the STS .dat files which are in the format of I vs V.
% First column is the Voltage, subsequent columns are each individual
% current,I, sweep. The number of rows is the number of data points in each
% sweep. Each data file, Data10000i.dat, represents the data taken at the
% ith point in an x by y conductance map. The data is loaded into a matrix,
```

```
% Islice, which is then used in the program, dIdVfind
% iline: the number of total data files to load, represents the ith data
% point
% in an x vs y data set
% xline: the number of x data points in an x vs y data set
% yline: the number of y data points in an x vs y data set
% Islice: the final data matrix that is x vs y vs V
% k : the number of data points in an individual I vs V scan



clear all
xline=64
yline=64
iline=4096
for i=1:iline
   i
   clear i2 test slicename ab ac A %this variables are temporary counters in
   %the program
   ab=mod(i,xline);
   if ab==0
      ab=xline;
   end
   ac=(i-ab)/yline+1;
```

```
    i2=100000+i;
    test=int2str(i2);
    slicename = sprintf('Data%s.txt', test);
    A=dlmread(slicename);
    Islice(ab,ac,1:1401-55)=A(1:1401-55)';
end
```

The second program, dIdVfind, takes the I vs. V data and calculates the differential conductance, dI/dV:

dIdVfind:

```
%{ This program calculates dI/dV vs. V or the differential conductance.
% dI/dV is calculated from the matrix Islice(x vs. y vs. voltage sweep) via a
% running average.  The order of the derivative is the number of points
% used in the fit for the derivate.  This program fits a 1st or 3rd
% order polynomial to each I vs. V sweep at each x and y point.  This
% fit is "order" in length, is a running average along the sweep, and the
%derivative is found from the polynomial
% fit
% order: number of points used in the fit
% voltagedivide : the voltage unit of the I vs. V sweep ( in millivolts)
% startvoltage: the start voltage of the I vs. V sweep
% P, PP are the 1st and 3rd order fits according of the I vs. V ft
% meanIdidv1, meanIdidv3 are the differential conductance sweeps of 1st and
```

```
% 3rd order fit accordingly
% voltnum is the number of points in the I vs. V sweep
% I v i j sizb dIdV are temporary variables and counters

clear I v PP P V dIdV* meanIdidv* i j sizb voltagedivide startvoltage voltnum
voltagedivide=1;
startvoltage=-672;
sizb=size(Islice)
order=75;
voltnum=sizb(3)
for i=1:sizb(1)
    i
    for j=1:sizb(2)
        j
        for voltnum=(order+1)/2:sizb(3)-(order+1)/2
            for m=1:order
                I(m)=Islice(i,j,voltnum-(order+1)/2+m);
                v(m)=voltagedivide*(-(order+1)/2+m);
            end
            P=polyfit(v,I,1);
            PP=polyfit(v,I,3);
            V(voltnum-(order-1)/2)=startvoltage+(voltnum)*voltagedivide;
            dIdV1(voltnum-(order-1)/2)=2*P(1);
```

```
            dIdV1(voltnum-(order-1)/2)=2*P(3);
        end
        meanIdidv1(i,j,:)=dIdV1(:);
        meanIdidv3(i,j,:)=dIdV3(:);
    end
end
```

The third program, bgfind, takes the dIdV vs. V data and calculates the normalized differential conductance. It insures that the area under the curve is normalized to a value of 1, while dividing out the high energy background. This is important for superconducting samples where the dI/dV must be normalized to one at high energies:

bgfind:

```
% This program calculates the background of each dI/dV vs V sweep and then
% calculates the high energy background by fitting a 5th order polynomial
% to the higher energies.  The background is then divided out and the curve
% then normalized so that the area under ther curve is one.
% background1,3 are the high energy backgrounds
% PP : the 5th order polynomial fit of the background
% meanIdidvbgnorm1,3 are the dIdV once it has been normalized
% temp k i j si su are temporary counters and variabes
% The data is then saved in individual files.  Each file contains exactly
% one curve, meanIdidvbgnorm3slice1000xxxx.
```

```
clear background1, clear background3, clear meanIdIdV1, clear meanIdIdV3

clear temp* k  i j  PP meanIdIdVbg* si su meanIdidvbgnorm* meanIbg*

siz=size(meanIdidv1);

for i=1:siz(1)


      for j=1:siz(2)

        i,j

         meanIdIdV1(1:siz(3))=meanIdidv1(i,j,1:siz(3));

         for k=1:100

            tempx(k)=V(k);

            tempx(k+100)=V(siz(3)-100+k);

            tempy(k)=meanIdIdV1(k);

            tempy(k+100)=meanIdIdV1(siz(3)-100+k);

            tempy(201)=0;

            tempx(201)=V(434);

         end

         PP=polyfit(tempx,tempy,5);


background1=PP(1)*V.^5+PP(2)*V.^4+PP(3)*V.^3+PP(4)*V.^2+PP(5)*V.^1+PP(6);

         meanIdIdVbg1=meanIdIdV1./background1;

         si=size(meanIdIdVbg1);

         su=sum(meanIdIdVbg1,2);

         meanIdIdVbgnorm1=si(2)/su*meanIdIdVbg1; % this command insures
```

```
        %that the area under the curve is normalized to one
        meanIdidvbgnorm1(i,j,:)=meanIdIdVbgnorm1(:);
        meanIbg1(i,j,1)=PP(1);
        meanIbg1(i,j,2)=PP(2);
        meanIbg1(i,j,3)=PP(3);
        meanIbg1(i,j,4)=PP(4);
        meanIbg1(i,j,5)=PP(5);
        meanIbg1(i,j,6)=PP(6);
    end

end
clear P* k temp* si su
for i=1:siz(1)
    for j=1:siz(2)
      i,j
      meanIdIdV3(1:siz(3))=meanIdidv3(i,j,1:siz(3));
      for k=1:100
         tempx(k)=V(k);
         tempx(k+100)=V(siz(3)-100+k);
         tempy(k)=meanIdIdV3(k);
         tempy(k+100)=meanIdIdV3(siz(3)-100+k);
         tempy(201)=meanIdIdV3(1);
         tempx(201)=V(400);
```

```
        end

        PP=polyfit(tempx,tempy,3);


background3=PP(1)*V.^5+PP(2)*V.^4+PP(3)*V.^3+PP(4)*V.^2+PP(5)*V.^1+PP(6);
        meanIdIdVbg3=meanIdIdV3./background3;
        si=size(meanIdIdVbg3);
        su=sum(meanIdIdVbg3,2);
        meanIdIdVbgnorm3=si(2)/su*meanIdIdVbg3;
        meanIdidvbgnorm3(i,j,:)=meanIdIdVbgnorm3(:);
        meanIbg3(i,j,1)=PP(1);
        meanIbg3(i,j,2)=PP(2);
        meanIbg3(i,j,3)=PP(3);
        meanIbg3(i,j,4)=PP(4);
        meanIbg3(i,j,5)=PP(5);
        meanIbg3(i,j,6)=PP(6);
    end


end


clear ta tb tc i j slicename* k ksize test*
% This code saves the each individual slice
ksize=size(meanIdidvbgnorm3);
for k=1:ksize(3)
```

```
    ta=meanIdidvbgnorm1(1:sizb(1),1:sizb(2),k);
    tb=meanIdidvbgnorm3(1:sizb(1),1:sizb(2),k);
    i=10000+k;
    test=num2str(i);
    i2=30000+k;
    test2=num2str(i2);
    slicename= sprintf('meanIdidvbgnormslice%s.txt', test);
    slicename2= sprintf('meanIdidvbgnormslice%s.txt', test2);
    dlmwrite(slicename,ta,'\t');
    dlmwrite(slicename2,tb,'\t');
end
```

The fourth program normalizes dIdV data for graphene or topological insulators. At every point it finds I(V)/V and then divides dI/dV by I(V)/V.

didvnormfind:

```
% This program normalizes the differential conductance by dividing each
% point by I(V)/V
% I  i k j are temporary variables
% meanIdidv1,3 V are defined in previous programs

clear I i j k temp* siz
siz=size(meanIdidv1);
```

```
sizb=size(Islice);
for i=1:siz(1)
   for j=1:siz(2)
        i,j
        meanIdIdV1(1:siz(3))=meanIdidv1(i,j,1:siz(3));
        I(1:siz(3))=Islice(i,j,(1+order/2):(sizb(3)-order/2));
        meanIdidvbgnorm1(i,j,1:siz(3))=meanIdidv1(i,j,1:siz(3))./(I(1:siz(3))./V(1:siz(3)));
        meanIdidvbgnorm3(i,j,1:siz(3))=meanIdidv3(i,j,1:siz(3))./(I(1:siz(3))./V(1:siz(3)));
   end

end
clear ta tb tc i j slicename* k ksize test*
% This code saves the each individual slice
ksize=size(meanIdidvbgnorm3);
for k=1:ksize(3)
   ta=meanIdidvbgnorm1(1:sizb(1),1:sizb(2),k);
   tb=meanIdidvbgnorm3(1:sizb(1),1:sizb(2),k);
   i=10000+k;
   test=num2str(i);
   i2=30000+k;
   test2=num2str(i2);
   slicename= sprintf('meanIdidvbgnormslice%s.txt', test);
   slicename2= sprintf('meanIdidvbgnormslice%s.txt', test2);
```

```
    dlmwrite(slicename,ta,'\t');
    dlmwrite(slicename2,tb,'\t');
end
```

The fifth program is a median filter. It filters an m x n matrix by taking the median of nearest neighbors

```
%This program does a nearest neighbor median filter.  The final product is
%med and its input is an m x n matrix, r:
clear local, clear r_med, clear x_med, ,clear med1;


r_med=r;
for i=2:63
    for j=2:63
        local=[r(i-1,j-1),r(i-1,j),r(i-1,j+1),r(i,j-1),r(i,j),r(i,j+1),r(i+1,j-1),r(i+1,j),r(i+1,j+1)];
        r_med(i,j)=median(local);
    end
end
med=r;
med(2:63,2:63)=r_med(2:63,2:63);
figure, imagesc(med,[0,3])
```

The sixth program, rmed2, is a mean filter program. It filters an m x n matrix by taking the mean of nearest neighbors

```
%This program does a nearest neighbor mean filter.  The final product is
%med and its input is an m x n matrix, r:
clear local, clear r_med, clear x_med, ,clear med1;



r_med=r;
for i=2:63
   for j=2:63
      local=[r(i-1,j-1),r(i-1,j),r(i-1,j+1),r(i,j-1),r(i,j),r(i,j+1),r(i+1,j-1),r(i+1,j),r(i+1,j+1)];
      r_med(i,j)=mean(local);
   end
end
med=r;
med(2:63,2:63)=r_med(2:63,2:63);
figure, imagesc(med,[0,3])
```

BIBLIOGRAPHY

[1] J. G. Bednorz and K. A. Muller, Zeitschrift, Physik B Condensed Matter **64**, 189 (1986)

[2] P. A. Lee, N. Nagaosa and X.-G. Wen, Rev. Mod. Phys. **78**, 17 (2006).

[3] S. A. Kivelson, I. P. Bindloss, E. Fradkin, V. Oganesyan, J. M. Tranquada, A. Kapitulnik, and C. Howald, Rev. Mod. Phys. **75**, 1201 (2003).

[4] S. Sachdev, Rev. Mod. Phys. **75**, 913 (2003).

[5] E. Demler, W. Hanke, and S.-C. Zhang, Rev. Mod. Phys. **76**, 909 (2004).

[6] N.-C. Yeh and A. D. Beyer, Int. J. Mod. Phys. B **23**, 4543 (2009).

[7] O. Fischer, M. Kugler, I. Maggio-Aprile, C. Berthod, and C. Renner, Reviews of ModernPhysics **79**, 353 (2007)

[8] C. C. Tsuei and J. R. Kirtley, Rev. Mod. Phys. **72**, 969 (2000).

[9] N.-C. Yeh, C.-T. Chen, G. Hammerl, J. Mannhart, A. Schmehl, C. W. Schneider, R. R. Schulz, S. Tajima, K. Yoshida, D. Garrigus, et al., Phys. Rev. Lett. **87**, 087003 (2001).

[10] C. Renner, B. Revaz, J.-Y. Genoud, K. Kadowaki, and O. Fischer, Phys. Rev. Lett. **80**, 149 (1998).

[11] N.-C. Yeh, A. D. Beyer, M. L. Teague, S.-P. Lee, S. Tajima and S. I. Lee, J. Supercond. Nov. Magn. **23**,757 (2010).

[12] T. Timusk and B. Statt, Rep. Prog. Phys. **62**, 61 (1999).

[13] A. D. Beyer, M. S. Grinolds, M. L. Teague, S. Tajima, and N.-C. Yeh, Europhys. Lett. **87**, 37005 (2009).

[14] C.-T. Chen, A. D. Beyer, and N.-C. Yeh, Solid State Commun. **143**, 447 (2007).

[15] A. D. Beyer, C.-T. Chen, and N.-C. Yeh, Physica C **468**, 471 (2008).

[16] N.-C. Yeh, A. D. Beyer, M. L. Teague, S.-P. Lee, S. Tajima, and S. I. Lee, Int. J. Mod. Phys. B **19**, 285 (2005).

[17] N.-C. Yeh, C. T. Chen, A. D. Beyer, and S. I. Lee, Chinese J. Phys. **45**, 263 (2007).

[18] M. Vershinin, S. Misra, S. Ono, Y. Abe, Y. Ando, and A. Yazdani, Science **303**, 1995 (2004).

[19] M. C. Boyer, W. D. Wise, K. Chatterjee, M. Yi, T. Kondo, T. Takeuchi, H. Ikuta, Y. Wang, and E. W. Hudson, Nature Phys. **3**, 802 (2007).

[20] K. K. Gomes, A. N. Pasupathy, A. Pushp, S. Ono, Y. Ando, and A. Yazdani, Nature **447**, 569 (2007).

[21] Y. Krockenberger, B. Welter, M. Schonecke, R. Gross, D. Manske, M. Naito, and L. Al, Nature **422**, 698 (2003).

[22]B.-L. Yu, J. Wang, A. D. Beyer, M. L. Teague, J. S. A. Horng, S.-P. Lee, and N.-C. Yeh, Solid State Commun. **149**, 261 (2009).

[23]Damascelli, Z. Hussain, and Z.-X. Shen, Rev. Mod. Phys. **75**, 473 (2003).

[24] W. S. Lee, I. M. Vishik, K. Tanaka, D. H. Lu, T. Sasagawa, N. Nagaosa, T. P. Devereaux, Z. Hussain, and Z.-X. Shen, Nature **450**, 81 (2007).

[25] K. Yamada, S. Wakimoto, G. Shirane, C.-H. Lee, M. A. Kastner, S. Hosoya, M. Greven, Y. Endoh, and R. J. Birgeneau, Phys. Rev. Lett. **75**, 1626 (1995).

[26] B. Lake, H. M. Ronnow, N. B. Christensen, G. Aeppli, K. Lefmann, D. F. McMorrow, P. Vorderwisch, P.Smeibidl, N. Mangkorntong, T. Sasagawa, M. Nohara, H. Takagi, and T. E. Mason, Nature **415**, 299 (2002).

[27] C.-H. Lee, K. Yamada, Y. Endoh, G. Shirane, R. J. Birgeneau, M. A. Kastner, M. Greven, and Y. J. Kim, J. Phys. Soc. Japan **69**, 1170 (2000).

[28] K. Yamada, K. Kurahashi, T. Uefuji, M. Fujita, S. Park, S.-H. Lee, and Y. Endoh, Phys. Rev. Lett. **90**,137004 (2003).

[29] M. Fujita, M. Matsuda, S. Katano, and K. Yamada, Phys. Rev. Lett. **93**, 147003 (2004).

[30] H. J. Kang, P. Dai, H. A. Mook, D. N. Argyriou, V. Sikolenko, J. W. Lynn, Y. Kurita, S. Komiya, and Y. Ando, Phys. Rev. B **71**, 214512 (2005).

[31] S.-C. Zhang, Science **275**, 1089 (1997).

[32] M. Vojta, Y. Zhang, and S. Sachdev, Phys. Rev. B **62**, 6721 (2000).

[33] C. M. Varma, Phys. Rev. B **55**, 14554 (1997).

[34] E. Demler, S. Sachdev, and Y. Zhang, Phys. Rev. Lett. **87**, 067202 (2001).

[35] A. Polkovnikov, M. Vojta, and S. Sachdev, Phys. Rev. B **65**, 220509(R) (2002).

[36] Y. Chen, H. Y. Chen, and C. S. Ting, Phys. Rev. B **66**, 104501 (2002).

[37] H. D. Chen, J.-P. Hu, S. Capponi, E. Arrigoni, and S.-C. Zhang, Phys. Rev. Lett. **89**, 137004 (2002).

[38] H.-D. Chen, O. Vafek, A. Yazdani, and S.-C Zhang, Phys. Rev. Lett. **93**, 187002 (2004).

[39] S. Chakravarty, R. B. Laughlin, D. K. Morr, and C. Nayak, Phys. Rev. B **63**, 094503 (2001).

[40] U. Schollwöck, S. Chakravarty, J. O. Fjærestad, J. B. Marston, and M. Troyer, Phys. Rev. Lett. **90**, 186401(2003).

[41] J. X. Li, C. Q.Wu, and D.-H. Lee, Phys. Rev. B **74**, 184515 (2006).

[42] S. Chakravarty, H.-Y. Kee, and K. Volker, Nature (London) **428**, 53 (2004).

[43] Y. Kamihara, T. Watanabe, M. Hirano, and H. Hosono, J. Am. Chem. Soc. **130**, 3296 (2008).

[44] N.-C. Yeh, "Spectroscopic Studies of Quasiparticle Low-Energy Excitations in Cuprate and Iron-Based High-Temperature Superconductors" "Endless Quests" Peking University Press (2012).

[45] K.S. Novoselov, Two-dimensional gas of massless Dirac fermions in graphene. Nature **438**, 197 (2005).

[46] X. Du, I. Skachko, A. Barker, and E. Y. Andrei, Nature Nanotechnology, **3**, 491 (2008).

[47] K. I. Bolotin, K. J. Sikes, Z. Jiang, M. Klima, G. Fudenberg, J. Hone, P. Kim, and H. L. Stormer, Solid State Commun. **146**, 351 (2008).

[48] Y. B. Zhang, Y. W. Tan, H. L. Stormer, and P. Kim, Nature **438**, 201(2005).

[49] K. S. Novoselov, Z. Jiang, Y. Zhang, S. V. Morozov, H. L. Stormer, U. Zeitler, J. C. Maan, G. S. Boebinger, P. Kim, and A. K. Geim, Science, **315**, 1379 (2007).

[50] T. Matsui, H. Kambara, Y. Niimi, K. Tagami, M. Tsukada, and H. Fukuyama, Phy. Rev. Lett. **94**, 226403 (2005).

[51] V. P. Gusynin, and S. G. Sharapov, Phys Rev. Lett. **95**, 146801 (2005).

[52] F. Miao, S. Wijeratne, Y. Zhang, U. C. Coskun, W. Bao, and C. N. Lau, Science **317**, 1530-1533 (2007).

[53] C. Berger, Z. Song, X. Li, X. Wu, N. Brown, C. Naud, D. Mayou, T. Li, J. Hass, A. Marchenkov, E. Conrad, and W. de Heer, Science **312**, 1991 (2006).

[54] K. Emtsev, A. Bostwick, K. Horn, J. Jobst, G. Kellogg, L. Lothar, J. McChesney, and T. Ohta, Nat. Mater. **8**, 203 (2009).

[55] S. Stankovich, D. Dikin, R. Piner, K. Kohlhass, A. Kleinhammes, Y. Jia, Y. Wu, S. Nguyen, and R. Ruoff, Carbon **45**, 1558 (2008).

[56] G. Eda; Fanchini, G; and Chhowalla, M;., Nat. Nanotechnol. **3**, 270 (2008).

[57] P. W. Sutter, J.-I. Flege, and E. A. Sutter, Nat. Mater. **7**, 406 (2008).

[58] A. L. de Parga, F. Calleja, B. Borca, M.C. Passeggi, J. J. Hinarejos, F. Guinea, and R. Miranda, Phys. Rev. Lett. **100**, 056807 (2008).

[59] A. Reina, X. Jia, J. Ho, D. Nezich, H. Son, V. Bulovic, M. S. Dresselhaus and J. Kong, Nano Lett. **9**, 30 (2009).

[60] K. Kim, Y. Zhao, H. Jang, S. Lee, J. Kim, K. Kim, J. Ahn, and P. Kim, Nature, **457**, 706 (2009).

[61] H. Ueta, S. Morihiko, C. Nakai, Y. Yamada, M. Sasaki, and S. Yamamoto, Surf. Sci. **560**, 183 (2004).

[62] D. E. Starr, E. M. Pazhetnov, A. I. Stadnichenko, A. I. Boronin, and S. K. Shaikhutdinov, Surf. Sci., **600**, 2688 (2006).

[63] J. Vaari, J. Lahtinen, and P. Hautojarvi, P, Catal. Lett., **44**, 43 (1997).

[64] L. He, F.-X. Xiu, Y. Wang, A. V. Fedorov, G. Huang, X. Kou, M. Lang, W. P. Beyermann, J. Zou, and K. L. Wang, J. Appl. Phys. **109** 103702 (2007).

[65] A. H. Castro Neto, F. Guinea, N. M. R. Peres, K. S. Novoselov, and A. K. Geim, Rev. Mod. Phys. **81** 109 (2009).

[66] R. R. Biswas and A. V. Balatsky, Phys. Rev. B **81** 233405 (2010).

[67] K. Saha, I. Paul, and K. Sengupta, Phys. Rev. B **81** 165446 (2010).

[68] G. Binnig, H. Rohrer, C. Gerber, and E. Weibel, Applied Physics Letters **40**,178 (1982).

[69] R. Wiesendanger, Scanning Probe Microscopy and Spectroscopy: Methods and Applications Scanning Probe Microscopy and Spectroscopy: Methods and Applications Cambridge, Massachusetts, Cambridge University Press (1994).

[70] C. Julian Chen, Introduction to Scanning Tunneling Microscopy Oxford, New York, Osford University Press (1993).

[71] L. D. Landau and E. M. Lifshitz, Quantum Mechanics 3rd edition, Pergamon Press Oxford. (1977).

[72] R. M. Feenstra, In: Scanning Tunneling Microscopy and related Methods (ed. Behm, Garcia, and Roher), NATO ASI Series E: Appl. Sci.Vol **184**, 211 (1990).

[73] E. Stoll, Resolution of the scanning tunneling microscope. Surf. Sci. **143,** L411-L416 (1984).

[74] R. M. Feenstra and J. A. Stroscio, Physica Scripta **T19A, 55** (1987).

[75] C. T. Chen, Scanning Tunneling Spectroscopy Studies of High-Temperature Cuprate Superconductors, Ph. D. Dissertation, California Institute of Technology (2006).

[76] B. L. Rogers, J. G. Shapter, W. M. Skinner, and K. Gascoigne, Review of Scientific Instruments
71, 1702 (2000).

[77] J. P. Ibe, Journal of Vacuum Science and Technology Vol.**8** Iss. 4 p. 3570 (1990)

[78] Y. B. Zhang, V. W. Brar, F. Wang, C. Girit, Y. Yayon, M. Panlasigui, A. Zettl, and M. F. Crommie, Nature Physics **4**, 627 (2008).

[79] A. D. Beyer, Studies of the low-energy quasiparticle excitations in high temperature superconducting cuprates using scanning tunneling microscopy and magnetization measurements, Ph.D. Dissertation, California Institute of Technology (2009).

[80] F. P. Milliken, J. R Rozen, G. A. Keefe, R. H. Koch, Review of Scientific Instruments **78**, 024701 (2007).

[81] S. J. Hagen, A. W. Smith, M. Rajeswari, J. L. Peng, Z. Y. Li, R. L. Greene, S. N. Mao, X. X. Xi, S. Bhattacharya, Q. Li, and C. J. Lobb, Phys. Rev. B **47**, 1064 (1993).

[82] M. L. Teague, A. D. Beyer, M. S. Grinolds, S. I. Lee and N.-C. Yeh, Europhys. Lett. **85**, 17004 (2009).

[83] M. S. Kim, T. Lemberger, and S.-I. Lee, Phys. Rev. B **66,** 214509 (2002).

[84] V. S. Zapf, N.-C. Yeh, A. D. Beyer, C. R. Hughes, C. H. Mielke, N. Harrison, M. S. Park, K. H. Kim, and S.-I. Lee, Phys. Rev. B **71**, 134526 (2005).

[85] C. U. Jung, J. Y. Kim, M.-S. Park, M.-S. Kim, H.-J. Kim, S. Y. Lee, and S.-I. Lee, Phys. Rev.B **65**, 172501 (2002).

[86] R. P. Vasquez, C. U. Jung, J. Y. Kim, M.-S. Park, H.-J. Kim, and S.-I. Lee, Journal of Physics: Condensed Matter **13**, 7977 (2001).

[87] G. V. M. Williams, R. Dupree, A. Howes, S. Kramer, H. J. Trodahl, C. U. Jung, M.-S. Park,and S.-I. Lee, Phys. Rev. B **65**, 224520 (2002).

[88] K. McElroy, D.-H. Lee, J. E. Hoffman, K. M. Lang, J. Lee, E. W. Hudson, H. Eisaki, S. Uchida, and J. C. Davis, Phys. Rev. Lett., **94,** 197005 (2005).

[89] C.-T. Chen, P. Seneor, N.-C. Yeh, R. P. Vasquez, L. D. Bell, C. U. Jung, J. Y. Kim, M.-S. Park, H.-J. Kim, and S.-I. Lee, Phys. Rev. Lett. **88**, 227002 (2002).

[90] Q. Huang, Y. Qiu, W. Bao, M. A. Green, J. W. Lynn, Y. C. Gasparovic, T. Wu, G. Wu and X. H. Chen,Phys. Rev. Lett. **101**, 257003 (2008).

[91] Ø. Fischer, M. Kugler, I. Maggio-Aprile, and C. Bethord, Rev. Mod. Phys., **79** 353 (2007).

[92] S. H. Pan, E. W. Hudson, A. K. Gupta, K.-W. Ng, H. Eisaki, S. Uchida, and J. C. Davis, Phys. Rev. Lett. **85**, 1536 (2000).

[93] E. M. Motoyama, P. K. Mang, D. Petitgrand, G. Yu, O. P. Vajk, I. M. Vishik, and M. Greven, Phys. Rev. Lett. **96**, 137002 (2006).

[94] J. R. Schrieffer, X. Wen, and S. Zhang, Phys. Rev. B **39**,11663 (1989).

[95] H. F. Hess, R. B. Robinson, R. C. Dynes, J. M. Valles, and J. V. Waszczak, Phys. Rev. Lett. **62**, 214 (1989).

[97] H. Matsui, K. Terashima, T. Sato, T. Takahashi, M. Fujita, K. Yamada, Phys. Rev.Lett. **95** 017003 (2005).

[98] Y. Kamihara, T. Watanabe, M. Hirano and H. Hosono, J. Am. Chem. Soc. **130**, 3296 (2008) .

[99] V. Cvetkovic and Z. Tesanovic, Europhys. Lett. **85**, 37002 (2008).

[100] M. R. Norman, Physics **1**, 21 (2008).

[101] Z. Tesanovic, Physics **2**, 60 (2009).

[102] K. Sasmal, K. Sasmal, B. Lv, B. Lorenz, A. M. Guloy, F. Chen, Y. Y. Xue and C. W. Chu, Phys. Rev. Lett., **101**, 107007 (2008).

[103] M. Rotter, M. Tegel and D. Johrendt, Phys. Rev. Lett., **101**, 107006 (2008).

[104] A. S. Sefat, R. Jin, M. A. McGuire, B. C. Sales, D. J. Singh, and D. Mandrus, Phys. Rev. Lett. **101**, 117004 (2008).

[105] I. Mazin, Nature **464**, 183 (2010).

[106] F. Wang, H. Zhai and D.-H. Lee, Europhys. Lett., **85**, 37005 (2009).

[107] F. Wang, H. Zhai, Y. Ran, A. Vishwanath and D.-H. Lee, Phys. Rev. Lett. **102**, 047005 (2009).

[108]] I. I. Mazin, D. J. Singh, M. D. Johannes, and M. H. Du, Phys. Rev. Lett., **101**,057003 (2008).

[109] K. Kuroki, S. Onari, R. Arita, H. Usui, Y. Tanaka, H. Kontani, and H. Aoki, Phys. Rev. Lett., **101**, 087004 (2008).

[110] T. Das and A. V. Balatsky, Phys. Rev. Lett. **106**, 157004 (2011).

[111] M. M. Korshunov and I. Eremin, Phys. Rev. B, **78**, 140509(2008).

[112] T. A. Maier and D. J. Scalapino, Phys. Rev. B, **78**, 020514(2008).

[113] M. D. Lumsden, A. D. Christianson, D. Parshall, M. B. Stone, S. E. Nagler, G. J. MacDougall, H. A. Mook, K. Lokshin, T. Egami, D. L. Abernathy, E. A. Goremychkin, R. Osborn, M. A. McGuire, A. S. Sefat, R. Jin, B. C. Sales, and D. Mandrus, Phys. Rev. Lett., 2009 **102**, 107005 (2009).

[114] A. D. Christianson, E. A. Goremychkin, R. Osborn, S. Rosenkranz, M. D. Lumsden, C. D. Malliakas, I. S.Todorov, H. Claus, D. Y. Chung, M. G. Kanatzidis, R. I. Bewley and T. Guidi, Nature, **456**, 930 (2008).

[115] I. Eremin, D.K. Morr, A.V. Chubukov, K.H. Bennemann, and M.R. Norman,,Phys. Rev. Lett., **94**, 147001 (2005).

[116] Yu, Y. Li, E. M. Motoyama and M. Greven, Nature Phys., **5**, 873 (2009).

[117] M. C. Boyer, K. Chatterjee, W. D. Wise, G. F. Chen, J. L. Luo, N. L. Wang, and E. W. Hudson, arXiv:0806.4400, (2008).

[118] Yi Yin, M. Zech, T. L. Williams, X. F. Wang, G. Wu, X. H. Chen, and J. E. Hoffman, Phys. Rev. Lett. **102**, 097002 (2009).

[119] T.-M. Chuang, M.P. Allan, J. Lee, Y. Xie, N. Ni, S. L. Bud'ko, G. S. Boebinger, P. C. Confield, and J. C. Davis, Science **327**, 181 (2010).

[120] L. Fang, H. Luo, P. Cheng, Z. Wang, Y. Jia, G. Mu, B. Shen, I. Mazin, L. Shan, C. Ren, and H. -H. Wen, Phys. Rev. B **80**, 140508 (2009).

[121] C. Bernhard, A. J. Drew, L. Schulz, V.K. Malik, M. Roessle, Ch. Niedermayer, Th. Wolf, G.D. Varma, G. Mu, H.-H. Wen, H. Liu, G. Wu, and X.H. Chen, New J. Phys. **11**, 055050 (2009).

[123] B. Shen, P. Cheng, Z. Wang, L. Fang, C. Ren, L. Shan, and H.-H. Wen, Phys. Rev. B **81**, 014503(2010).

[124] D. H. Lu, M. Yi, S.-K. Mo, A. S. Erickson, J. Analytis, J.-H. Chu, D. J. Singh, Z. Hussain, T. H. Geballe, I. R. Fisher, and Z.-X. Shen, Nature **455**, 81 (2008).

[125] H. Ding, P. Richard, K. Nakayama, K. Sugawara, T. Arakane, Y. Sekiba, A. Takayama, S. Souma, T. Sato, T. Takahash, Z. Wang, X. Dai, Z. Fang, G. F. Chen, J. L. Luo and N. L. Wang, Europhys. Lett. **83**, 47001(2008).

[126] K. Terashima, Y. Sekiba, J. H. Brown, K. Nakayama, T. Kawahara, T. Sato, P. Richard, Y.-M. Xu, L. J. Li, G. H. Cao, Z.-A. Xu, H. Ding, and T. Takahashi, Proc. Natl. Acad. Sci. **106**, 7330 (2009).

[127] R. C. Dynes, V. Narayanamurti and J. P. Garno, Phys. Rev. Lett. **41**, 1509 (1978).

[128] L. Shan, Y.-L.Wang, B. Shen, B. Zeng, Y. Huang, A. Li, D. Wang, H. Yang, C. Ren, Q.-H. Wang, S. H. Pan and H.-H. Wen, Nat. Phys. **7**, 325 (2011).

[129] Y. Yin, M. Zech, T. L. Williams, X. F. Wang, G. Wu, X. H. Chen, and J. E. Hoffman, Phys. Rev. Lett., **102**, 097002 (2009).

[130]] R. Saito, M. S. Dresselhaus, Physical Properties of Carbon Nanotubes, Imperial College Press, London UK (1999).

[131] M. Dresselhaus, Adv. Phy. **51**, 186 (2002).

[132] A. K. Geim, Nature Materials **6**,183 (2007).

[133] G. Li and E. Andrei, Nature Physics **3**, 623 (2007).

[134] G. W. Semenoff, Phy. Rev. Lett. **53**, 2452 (1984).

[135] F. D. Halane, Phy. Rev. Lett. **61**, 2015 (1988).

[136] Y. Zheng, and T. Ando, Phys. Rev. B **65**, 245420 (2002).

[137] N. M. R. Peres, F. Guinea, and A. H. Castro Neto, Phys.Rev. B **73**, 125411 (2006).

[138] K. I. Bolotin, F. Ghahari, M. D. Shulman, H. L. Stormer, P. Kim, Nature **462,** 196 (2009).

[139] A. H. Castro Neto, F. Guinea, N. M. R. Peres, K. S. Novoselov, and A. K. Geim, Rev. Mod. Phys. **81**, 109 (2009).

[140] F. Guinea, M. I. Katsnelson, and A. K. Geim, Nat. Phys. **6**, 30 (2010).

[141] N. Levy, S. Burke, A. Zettl, F. Guinea, A. H. Castro Neto, M. Crommie, Science **329**, 544 (2010).

[142] C. Lee, X. Wei, J. Kysar, and J. Hone, Science **321**, 385 (2008).

[143] H. Suzuura, and T. Ando, Phys. Rev. B **65**, 235412 (2002).

[144] J. Mañes, Phys. Rev. B **76**, 045430 (2007).

[145] N.-C. Yeh, M. L. Teague, R. T.-P. Wu, H. Chu, D. A. Boyd, M. W. Bockrath, L. He, F.-X. Xiu and K.-L. Wang Europhysics Journal: Web of Conferences (2011).

[146] S. Choi, S. Jhi, and Y. Son, arXiv:0908.0977 (2009).

[147] F. Guinea, M. I. Katsnelson, and M. A. H. Vozmediano, Phys. Rev. B **77**, 075422 (2008).

[148] Y. Zhang, V. W. Brar, F. Wang, C. Girit, Y. Yayon, M. Panlasigui, A. Zettl and M. F. Crommie, Nature Physics **4**, 627 (2008).

[149] T. O. Wehling, I. Grigorenko, A. I. Lichtenstein, and A. Balatsky, Phys. Rev. Lett. **101**, 216803 (2008).

[150] J. Tersoff and D. R. Hamann, Phys. Rev. B **31**, 805 (1985)

[151] J. Heo, Probing electronic properties of carbon nanotubes. Ph.D thesis. California Institute of Technology. (2008).

[152] F. Guinea, M. I. Katsnelson, and M. A. H. Vozmediano, Phys. Rev. B **77**, 075422 (2008).

[153] G. M. Rutter, J. N. Crain, N. P. Guisinger, T. Li, P. N. First, and J. A. Stroscio, Science **317** 219 (2009).

[154] N.-C. Yeh, M. L. Teague, D. A. Boyd, M. W. Bockrath, J. Velasco, and C.-N. Lau, invited paper in ECS Transactions - Vancouver, Canada, Volume **28**, Issure **5**, "Graphene, Ge/III-V, and Emerging Materials for Post-CMOS Applications 2", 115 (2010).

[155] X. Li, W. Cai, J. An, S. Kim, J. Nah, D. Yang, R. Piner, A. Velamakanni, I. Jung, E. Tutuc, S. K. Banerjee, L. Colombo, and R. Ruoff1, Science **324**, 1312 (2009).

[156] E. Stolyarova, K. T. Rim, S. Ryu, J. Maultzsch, P. Kim, L. E. Brus, T. F. Heinz, M. S. Hybertsen, and G. W. Flynn, Proc. Natl. Acad. Sci. **104**, 9209 (2007).

[157]] M. Ishigami, J. H. Chen, W. G. Cullen, M. S. Fuhrer, and E. D. Williams,. Nano Letters **7**, 1643 (2007).

[158] P. Mallet, F. Varchon, C. Naud, L. Magaud, C. Berger, and J.-Y. Veuillen, Phys. Rev. B **76**, 041403 (2007).

[159] N.-C. Yeh, M. L. Teague, R. T.-P. Wu1, H. Chu, D. A. Boyd, M. W. Bockrath, L. He, F.-X. Xiu and K.-L. Wang, Europhysics Journal: Web of Conferences for the Proceedings of the Eurasia Pacific Summer School and Conference on Strongly Correlated Electrons (2011).

[160] I. V. Solovyev, A. I. Liechtenstein, and K. Terakura, Phys. Rev. Lett. **80**, 5758 (2009).

[161] I. F. Herbut, Phys. Rev. B **78**, 205433 (2008).

[162] X.-L. Qi and S.-C. Zhang, Phys. Today **63**, 33 (2010).

[163] M. Z. Hasan and C. L. Kane, Rev. Mod. Phys. **82**, 3045 (2010).

[164] L. Fu and C. L. Kane, Phys. Rev. B **76**, 045302 (2007).

[165] H. Zhang, C.-X. Liu, X.-L. Qi, X. Dai, Z. Fang and S-C. Zhang, Nat. Phys. **5**, 438 (2009).

[166] R. R. Biswas and A. V. Balatsky, Phys. Rev. B **81,** 233405 (2010).

[167] K. Saha, I. Paul, and K. Sengupta, Phys. Rev. B **81**, 165446 (2010).

[168] L. He, F.-X. Xiu, Y. Wang, A. V. Fedorov, G. Huang, X. Kou, M. Lang, W. P. Beyermann, J. Zou, and K. L. Wang, J. Appl. Phys. **109**, 103702 (2011).

[169] M. L. Teague, H. Chu, F.-X. Xiu, L. He, K.-L. Wang and N.-C. Yeh, Solid State Comm. **152**, 747 (2012).

[170] W. Y. Shan, H.-Z. Lu and S.-Q. Shen, New J. Phys. **12**, 043048 (2010).

[171] Y. Zhang, K. He, C.-Z. Chang, C.-L. Song, L.-L. Wang, X. Chen, J.-F. Jia, Z. Fang, X. Dai, W.-Y. Shan, S.-Q. Shen, Q. Niu, X.-L. Qi, S.-C. Zhang, X.- C. Ma and Q.-K. Xue, Nat. Phys. **6**, 584 (2010).

[172] P. Roushan, J. Seo, C. V. Parker, Y. S. Hor, D. Hsieh, D. Qian, A. Richardella, M. Z. Hasan, R. J. Cava and A. Yazdani, Nature **460**, 1106 (2009).

[173]] N.-C. Yeh, M. L. Teague, R. T.-P. Wu, H. Chu, D. A. Boyd, M. W. Bockrath, L. He, F.-X. Xiu and K.-L. Wang, to appear in EPJ Web of Conference (2012).

[174] L. He, F. Xiu, X. Yu, M. L. Teague, W. Jiang, Y. Fan, X., Kou, M. Lang, Y. Wang, G. Huang, N.-C. Yeh, and K. L. Wang, Nano Lett. **12**, 1486 (2012).